

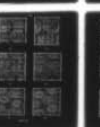
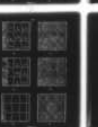
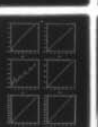
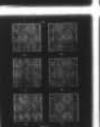
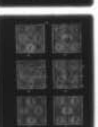
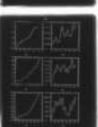
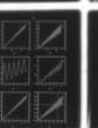
AD-A052 827

HARVARD UNIV CAMBRIDGE MA DIV OF APPLIED SCIENCES
THE ACCURACY, EFFICIENCY AND STABILITY OF THREE NUMERICAL MODEL--ETC(U)
FEB 78 D B HAIDVOGEL, E E SCHULMAN

F/G 8/3
N00014-75-C-0225
NL

UNCLASSIFIED

1 of 2
ADA
052827



AD No.
DDC FILE COPY

AD A 052827

Unclassified

SECURITY CLASSIFICATION OF THIS PAGE (When Data Entered)

REPORT DOCUMENTATION PAGE		READ INSTRUCTIONS BEFORE COMPLETING FORM
1. REPORT NUMBER Reports in Meteorology and Oceanography, No. 11	2. GOVT ACCESSION NO.	3. RECIPIENT'S CATALOG NUMBER 9
4. TITLE (and Subtitle) The Accuracy, Efficiency and Stability of Three Numerical Models with Application to Open Ocean Problems	5. TYPE OF REPORT & PERIOD COVERED Progress Report. no. 11	
6. PERFORMING ORG. REPORT NUMBER		7. AUTHOR(s) D. B. Haidvogel E. E. Schulman A. R. Robinson
8. CONTRACT OR GRANT NUMBER(s) N00014-75-C-0225 NSF-OCE76-00869		9. PERFORMING ORGANIZATION NAME AND ADDRESS Harvard University Cambridge, MA 02138
10. PROGRAM ELEMENT, PROJECT, TASK AREA & WORK UNIT NUMBERS		11. CONTROLLING OFFICE NAME AND ADDRESS Office of Naval Research Arlington, Virginia 22217 CODE 480
12. MONITORING AGENCY NAME & ADDRESS (if different from Controlling Office) 12 104p.		13. REPORT DATE Feb 78
14. SECURITY CLASS. (of this report)		15. NUMBER OF PAGES 103
15a. DECLASSIFICATION/DOWNGRADING SCHEDULE		16. DISTRIBUTION STATEMENT (of this Report) Approved for public release and sale: distribution unlimited.
17. DISTRIBUTION STATEMENT (of the abstract entered in Block 20, if different from Report)		
18. SUPPLEMENTARY NOTES		
19. KEY WORDS (Continue on reverse side if necessary and identify by block number)		
20. ABSTRACT (Continue on reverse side if necessary and identify by block number) The inviscid barotropic vorticity equation is integrated under a variety of assumed initial and boundary conditions corresponding to linear and nonlinear box modes, forced nonlinear box modes, north wall forced modes, and linear and nonlinear Rossby waves (with and without mean advection). The former two classes of problems are defined within a closed domain. The latter two are partially or totally open to a specified external environment and therefore represent prototype limited-area calculations for the ocean. -over		

DD FORM 1473
1 JAN 73

EDITION OF 1 NOV 65 IS OBSOLETE
S/N 0102-014-6601

Unclassified

SECURITY CLASSIFICATION OF THIS PAGE (When Data Entered)

410 457

LB

20. Abstract - cont.

To determine the extent to which the accuracy and efficiency of limited-area calculations depend on the numerical integration scheme, each test problem is solved independently using the finite-difference (FD), finite-element (FE) and pseudospectral (PS) techniques. The three numerical models differ primarily in the formal accuracy of their spatial approximations and their treatment of vorticity at outflow points along the boundary. The FD model employs a centered second-order differencing scheme and requires an extrapolatory (computational) boundary condition to fix the values of vorticity at outflow boundary points. The FE model, which represents ψ and ζ as a summation of piecewise linear elements, is of fourth order for the linearized one-dimensional advective equation. Further, a technique is developed by which the determination of the interior values of ζ is decoupled from that of the boundary values; hence, the vorticity boundary conditions can be implemented without iterative techniques. Lastly, the "infinite-order" PS model avoids the assumption of lateral periodicity by expanding ψ and ζ in a double series of Chebyshev polynomials. The resulting vorticity equation is solved in the spectral domain using a modified alternating direction implicit method. All three models are of second order in time and have conservative formulations of the nonlinear terms.

Integrations of moderate length (5-10 periods of the known analytic solution) are performed to determine the accuracy, stability and efficiency of each model as a function of problem class and the associated physical and computational nondimensional parameters. The most important of these parameters are ϵ , the Rossby number, ν , the number of spatial degrees of freedom (grid points, expansion functions, etc.) per half wavelength of the reference solution, and η , the number of time steps per period of the reference solution. The latter two parameters are nondimensional measures of the spatial and temporal resolution of the numerical approximation.

These tests show that all three models are, in general, capable of delivering stable and efficient solutions to linear and weakly nonlinear problems in open domains ($0 \leq \epsilon \leq 0.4$, $4 \leq \nu \leq 10$, $64 \leq \eta \leq 128$). Despite their added complexity, however, the FE and PS models are on the average, 4 and 15 times more accurate respectively than the FD model even taking into account its increased efficiency. The results also suggest that given a judicious selection of a frictional (filtering) mechanism and/or computational boundary condition (to suppress the accumulation of gridscale features), each of the models can be made similarly accurate for highly nonlinear calculations ($\epsilon \gg 0.4$).

12

REPORTS IN METEOROLOGY AND OCEANOGRAPHY

Number 11

THE ACCURACY, EFFICIENCY AND STABILITY OF THREE
NUMERICAL MODELS WITH APPLICATION TO
OPEN OCEAN PROBLEMS

by

D. B. Haidvogel, E. E. Schulman and A. R. Robinson

Reproduction in whole or in part is permitted for any purpose of the U. S. Government. The research was sponsored by the Office of Naval Research under O. N. R. Contract No. N00014-75-C-0225 and by the National Science Foundation under N. S. F. Contract OCE76-00869. Computing facilities were supplied by the National Center for Atmospheric Research which is supported by the National Science Foundation.

ACCESSION NO.	
DTIC	White Section <input checked="" type="checkbox"/>
ADG	Off Section <input type="checkbox"/>
UNANNOUNCED	<input type="checkbox"/>
JUSTIFICATION	
BY	
DISTRIBUTION/AVAILABILITY CODES	
Dist.	AVAIL. and/or SPECIAL
A	

Division of Applied Sciences

Harvard University

February 1978

DDC
RECEIVED
APR 19 1978
D

ABSTRACT

The inviscid barotropic vorticity equation is integrated under a variety of assumed initial and boundary conditions corresponding to linear and nonlinear box modes, forced nonlinear box modes, north wall forced modes, and linear and nonlinear Rossby waves (with and without mean advection). The former two classes of problems are defined within a closed domain. The latter two are partially or totally open to a specified external environment and therefore represent prototype limited-area calculations for the ocean.

To determine the extent to which the accuracy and efficiency of limited-area calculations depend on the numerical integration scheme, each test problem is solved independently using the finite-difference (FD), finite-element (FE) and pseudospectral (PS) techniques. The three numerical models differ primarily in the formal accuracy of their spatial approximations and their treatment of vorticity at outflow points along the boundary. The FD model employs a centered second-order differencing scheme and requires an extrapolatory (computational) boundary condition to fix the values of vorticity at outflow boundary points. The FE model, which represents ψ and ζ as a summation of piecewise linear elements, is of fourth order for the linearized one-dimensional advective equation. Further, a technique is developed by which the determination of the interior values of ζ is decoupled from that of the boundary values; hence, the vorticity boundary conditions can be implemented without iterative techniques. Lastly, the "infinite-order" PS model avoids the assumption of lateral periodicity by expanding ψ and ζ in a double series of Chebyshev polynomials. The resulting vorticity equation is solved in the spectral domain using a modified alternating direction implicit method. All three models are of second order in time and have conservative formulations of the nonlinear terms.

Integrations of moderate length (5-10 periods of the known analytic solution) are performed to determine the accuracy, stability and efficiency of each model as a function of problem class and the associated physical and computational nondimensional parameters. The most important of these parameters are ϵ , the Rossby number, ν , the number of spatial degrees of freedom (grid points, expansion functions, etc.) per half wavelength of the reference solution, and η , the number of time steps per period of the reference solution. The latter two parameters are nondimensional measures of the spatial and temporal resolution of the numerical approximation.

These tests show that all three models are, in general, capable of delivering stable and efficient solutions to linear and weakly nonlinear problems in open domains ($0 \leq \epsilon \leq 0.4$, $4 \leq \nu \leq 10$, $64 \leq \eta \leq 128$). Despite their added complexity, however, the FE and PS models are on the average, 4 and 15 times more accurate respectively than the FD model even taking into account its increased efficiency. The results also suggest that given a judicious selection of a frictional (filtering) mechanism and/or computational boundary condition (to suppress the accumulation of gridscale features), each of the models can be made similarly accurate for highly nonlinear calculations ($\epsilon \gg 0.4$).

1. INTRODUCTION

Limited-area or regional modelling of the oceans is important for a number of scientific and potentially practical problems. These include real-time forecasting/hindcasting studies of the oceanic interior and regions of intense near-surface currents (such as the Gulf Stream), and idealized local dynamic studies of those subregions of the oceanic gyre thought to contribute to the generation and maintenance of the mean and transient fields of motion. The former studies relate to ongoing and anticipated measurements from a variety of modern techniques including satellite surveys of the ocean [1, 2]. The latter are prompted by recent advances in our modelling and understanding of the mesoscale features of the ocean circulation [3].

Numerical eddy-resolving general circulation models in gyre-scale systems (EGCM's) have shown that transient eddies similar to those observed play an important role in determining the mean flow [4-6]. The very high horizontal resolution needed to resolve adequately the dynamics on the scale of the eddies, however, make EGCM's expensive to run even when, in practice, basins of only a few eddy wavelengths in horizontal extent are used. Furthermore, gyre-scale models are complicated by the fact that they contain many subregions of distinct physics [7, 8].

For statistically homogeneous subregions of the gyre, local dynamical studies can be made with periodic boundary condition models. Such models assume that the physics is locally determined and essentially independent of information such as scales and amplitudes which could be generated elsewhere and continuously transported across the boundaries. Such "process" models have been used to investigate the dynamical properties of the mesoscale eddy field under simulated mid-ocean conditions in regions well removed from boundary layer effects [9, 10]. Many subregions of the gyre obviously violate the above assumptions. For such regions, as well as for many other regional hydrodynamic problems other more complicated boundary conditions are necessary [11]. Such problems include limited-area oceanic forecasting [12], coastal modelling [13], and the study of intense current systems and their associated instabilities.

The determination of valid and convenient forms of boundary conditions, particularly at points of outflow, constitutes a major, essentially unresolved, problem in the modelling of many hydrodynamic systems over regional domains. The choice of boundary conditions involves a number of physical, mathematical, and numerical (or computational) considerations. On large and regional scales, the conditions should correctly represent or parameterize the interaction of the (arbitrary) volume of fluid with its surroundings. Smaller scale physical phenomenon generated internally within the region should not be trapped but allowed to pass out of the domain; i. e., the model boundary should be transparent for such small-scale processes. The mathematical problem consisting of model equations and boundary conditions should be well posed. The numerical scheme chosen for computational purposes should be of desired accuracy and acceptable efficiency.

In its computational algorithms, a given numerical scheme may involve the use of boundary information which is not in principle required in the well-posed analytical problem. Such auxiliary information is known as a computational boundary condition and should be chosen for convenience and efficiency, but should not in principle affect physical results. In practice, specific problems appear to require special conditions and a trial and error approach is usually indicated. Alternate choices of boundary conditions do effect the accuracy and stability of regional computations. For instance, in viscous limited-area calculations it is known that incorrect specification of boundary conditions or data generally leads to the evolution of boundary layers adjacent to outflow [14, 15]. Several types of boundary conditions have been used to avoid the problems associated with outflow, including extrapolatory formulas [16, 17], and radiation conditions [11]. In inviscid systems, Charney, Fjortoft and von Neumann [18] originally argued heuristically that, given the stream-function at all boundary points, only the values of vorticity at inflow points were needed to determine consistently solutions to the barotropic vorticity equation. This conjecture has since been proven more rigorously [19]. In practice, however, unless iterative or implicit numerical techniques or one-sided differencing schemes are used, inviscid calculations require some auxiliary relationship by which to prescribe vorticity at outflow

boundary points. Such a numerical scheme is often sensitive to the specific choice of this computational boundary condition. An example of this has been given by Shapiro and O'Brien [20] in the context of a limited-area meteorological forecast. They showed that the method of characteristics worked well as a computational boundary condition but that the specification of vorticity at outflow boundary points on the basis of known boundary data led to numerical instability.

In this report, we evaluate the feasibility of performing barotropic open ocean calculations by investigating and comparing the accuracy, efficiency and stability of three limited-area numerical models based respectively on the finite-difference, finite-element and spectral approximation methods. The physical boundary conditions used are the Charney-Fjortoft-von Neumann conditions. The calculations are mostly inviscid but in some cases a dissipative filter is included. The codes differ primarily in the details and accuracy of their spatial discretization schemes and in their treatments of the vorticity at outflow. The statement of the nondimensional vorticity equation and a description of the numerical techniques are given in Sections 2 and 3.

The three models have been tested and intercompared for a variety of prototype physical problems in closed and open basins and over a range of the nondimensional physical and computational parameters corresponding to each problem class. First, the unforced (homogeneous) solutions to the linear and nonlinear vorticity equation in a closed-basin are found and compared to the known exact and perturbation solutions for linear and nonlinear box modes respectively (Section 4). With the addition of a body force, various exact nonlinear closed-basin solutions are constructed and tested (Section 5). Next, oscillations driven by time-dependent distribution of boundary values along the northern (open) boundary are examined (North wall forced modes - Section 6). Lastly, in a fully open domain, linear and nonlinear Rossby wave solutions with and without mean advection are obtained and intercompared (Section 7). Model-model inter-comparisons of this type have been carried out for simple advective problems in closed basins (e.g., Orszag and Israeli [21]). To our knowledge, however, this is the first such study that encompasses limited-area hydrodynamic modelling problems as well.

The development of a regional quasigeostrophic modelling capability has two immediate intended applications. Firstly, forecasting/hind-casting studies of the mid-ocean mesoscale eddy field will be undertaken. For this work the MODE and POLYMODE synoptic data sets, can be utilized in a variety of ways both as boundary information and forecast verification data. Secondly, motivated by recent EGCM simulations of eddy generation and eddy mean field interaction in regions of intense mean flow, the finite-amplitude instabilities of idealized jets will be investigated as a function of environmental parameters and inlet conditions. Ultimately, if possible, real Gulf Stream meander region observational data will be used. For these purposes, baroclinic models will be needed. The extension of the following results to a multi-level configuration is, however, straightforward. A two-level version of the code described in Section 3.3 is already operational.

2. MODELLING EQUATIONS, METHODOLOGY AND FORMAT OF RESULTS

We consider the barotropic vorticity equation on a β -plane which can be written in dimensional form as

$$\left\{ \frac{\partial}{\partial t} + J(\psi, \zeta) \right\} (\zeta + f) = F(x, y) \quad \begin{array}{l} 0 \leq x \leq L_x \\ 0 \leq y \leq L_y \end{array} \quad (1)$$

where

$$f = f_0 + \beta y$$

and

$$J(\psi, \zeta) = \frac{\partial \psi}{\partial x} \frac{\partial \zeta}{\partial y} - \frac{\partial \psi}{\partial y} \frac{\partial \zeta}{\partial x}.$$

In addition,

$$\zeta = \nabla^2 \psi \quad (2)$$

is the relationship between streamfunction (ψ) and vorticity (ζ), and $F(x, y)$ represents the effects of a body force, if any. Dissipation has been neglected for three reasons. First, the inviscid system poses a simpler physical and numerical problem, one for which many analytic and perturbation solutions are available. This is the basis of our testing of the limited-area models described in Section 3. Second, quadratic conservation laws are available for non-dissipative physical and numerical systems. This property also contributes to the evaluation of model performance. Lastly, by ignoring explicit higher-order friction, we sidestep for the moment the question of the correct specification of vorticity boundary conditions on outflow, which are not formally needed for integration of the inviscid system. The assumption of inviscid dynamics does, however, require that greater care be taken to construct a numerical scheme which is stable in the absence of explicit dissipative (that is, smoothing) mechanisms. As we shall see, such filtering is in fact necessary to maintain stability in some cases.

If we now nondimensionalize x , y , t , and ψ by d , d , $(\beta d)^{-1}$ and $(V_0 d)$ respectively, then (1) becomes, in nondimensional form,

$$\left\{ \frac{\partial}{\partial t} + \epsilon J(\psi,) \right\} \nabla^2 \psi + \psi_x = F(x, y) \quad \begin{array}{l} 0 \leq x \leq x_B \\ 0 \leq y \leq y_B \end{array} \quad (3)$$

where the Rossby number

$$\epsilon = V_0 / \beta d^2$$

and

$$x_B = L_x / d \quad y_B = L_y / d .$$

The parameters d and V_0 are taken to be the characteristic length and velocity scales of the anticipated field of motion. Note that the length scale d does not correspond to the basin dimensions L_x or L_y ; hence, x_B and y_B are, in general, greater than one.

The modelling strategy developed herein involves the integration of Eq. (3) for several sets of initial and boundary conditions corresponding to successingly more complex physical phenomena in closed and open domains. The problems we will consider include linear and nonlinear box modes, forced nonlinear box modes, linear and nonlinear north wall forced modes (meander-induced forcing), and linear and nonlinear Rossby waves. The sequence of linear problems (box modes, north wall forced modes, and Rossby waves) serve as pivotal calculations for which no boundary values of vorticity are formally required. With the addition of nonlinearity, both accuracy and stability of model calculations can be assessed as a function of ϵ for closed-domain problems in which strict conservation laws apply (nonlinear and forced nonlinear box modes), and partially open and totally open domain problems in which interaction with the surrounding environment is possible and the question of computational boundary conditions arises (nonlinear north wall forced modes and nonlinear Rossby waves). The former experiments are the most easily understood. The latter series of tests - particularly the nonlinear Rossby waves with mean advection - are those most relevant to future open ocean modelling applications.

Each problem thus defined has been solved using three independent (and quite different) numerical techniques. The finite-difference (FD) scheme is second-order accurate in space and time and has the advantage of being easily coded. It should, in addition, be the most efficient of the three models for a fixed number of spatial degrees of freedom. The finite-element (FE) method, though somewhat more complicated than the FD scheme, is known to be of fourth order for certain advective problems [22]. In general, we expect smaller errors with the FE model, but at a slightly higher computational cost. Lastly, pseudospectral (PS) approximation techniques [21] offer greatly reduced spatial truncation errors in comparison to both of the other two methods. The PS model is, therefore, formally the most accurate but thereby it may be subject to instabilities not seen in the FD formulation - see, for instance, Section 7. Of the three models, it is also the most difficult to code (although it can be made comparably efficient if care is taken to optimize the spectral transforms).

Since analytic or perturbation solutions are available for many of the prototype physical problems examined herein, direct measures of numerical error are available for each model. Of particular interest are the RMS errors in streamfunction and vorticity, and the normalized difference in integrated kinetic energy as a function of time; these area integrated error measures are defined as

$$\text{RMS}(\psi') = \left\{ \iint (\psi_c - \psi_a)^2 dA / \iint (\psi_a)^2 dA \right\}^{1/2} \quad (4a)$$

$$\text{RMS}(\zeta') = \left\{ \iint (\zeta_c - \zeta_a)^2 dA / \iint (\zeta_a)^2 dA \right\}^{1/2} \quad (4b)$$

and

$$\text{NDIF}(\text{NRG}) = \left\{ \iint |\nabla \psi_c|^2 dA - \iint |\nabla \psi_a|^2 dA \right\} / \iint |\nabla \psi_a|^2 dA \quad (4c)$$

where subscripts c and a refer to the computed and analytic solutions respectively and a primed quantity represents a difference from the reference solution. Using error measures of this sort, it is possible to ascertain the accuracy of each model.

Table I summarizes the results of all the experiments as a function of problem type and the associated nondimensional parameters. The first

seven columns of Table I refer to the experiment number and the (not necessarily independent) quantities

(i)	ϵ	Rossby number
(ii)	$x_B = y_B$	nondimensional basin size
(iii)	N	number of spatial degrees of freedom in each direction
(iv)	$h = x_B/(N-1)$	nondimensional mesh interval
(v)	Δ	number of half wavelengths or turning points of the reference solution within the domain (nondimensional measure of the structure of the solution)
(vi)	$\nu = (N-1)/\Delta$	nondimensional spatial resolution (number of degrees of freedom per turning point of the reference solution)
(vii)	Δt	nondimensional time increment
and (viii)	η	nondimensional temporal resolution (number of time steps per period of the reference solution).

The last four columns tabulate the duration of the experiment (in periods) and the final values of the three error measures defined above. The duration of simulations which suffered numerical instability are denoted by brackets. No RMS error values are listed for these experiments. Intermediate columns of Table I are reserved for special parameters representative of each problem class. These will be introduced in Sections 4 through 7.

Accompanying Table I are a series of figures which show in more detail the results of one experiment for each problem category. Figures (1-3) are typical. The first two figures give contour plots of ζ and ψ , and ζ' and ψ' respectively at the end of the simulations for each model. Figure 3 shows the corresponding variation with time of $\text{RMS}(\zeta')$ and $\text{RMS}(\psi')$ for each model. Contouring intervals and scaling information are given in the figure captions. Note in particular that the RMS error curves are not necessarily scaled similarly, even within a given figure.

The former (contour) plots give a visual estimate of the wavenumber content of the computed solution (and hence an estimate of its formal spatial accuracy) and reveal any localized features (physical or numerical) that might occur. This is particularly important in those nonlinear experiments for which only approximate or linearized reference solutions are available and for which the RMS errors are therefore difficult to interpret.

3. MODEL FORMULATION

3.1 Finite-difference model

A traditional discrete formulation of Eq. (3) results by approximating all derivatives by second-order centered finite differences. The advantages of finite differences are the simplicity of the required coding and our accumulated experience of using this classical technique. With centered (leapfrog) time differencing, the vorticity and Poisson equations become:

$$\zeta^{k+1} = \zeta^{k-1} - \frac{2\Delta t \epsilon}{h^2} J^*(\psi^k, \zeta^k) - \frac{\Delta t}{h} \delta_x \psi^k \quad (5a)$$

and

$$\delta_{xx} \psi^{k+1} + \delta_{yy} \psi^{k+1} = h^2 \zeta^{k+1} \quad (5b)$$

where finite-difference operators $\delta_x(\psi^k) = \psi_{i+1,j}^k - \psi_{i-1,j}^k$ and $\delta_{xx}(\psi^k) = \psi_{i+1,j}^k - 2\psi_{i,j}^k + \psi_{i-1,j}^k$. The Arakawa [23] Jacobian J^* is given by the finite-difference approximation to the equivalent form $1/3\{[\psi_x \zeta_y - \psi_y \zeta_x] + [(\psi \zeta_y)_x - (\psi \zeta_x)_y] + [-(\psi_y \zeta)_x + (\psi_x \zeta)_y]\}$. This expression conserves vorticity, energy and enstrophy when integrated over a closed domain.

The Poisson equation (5b) with Dirichlet boundary conditions is approximated by the standard five point Laplacian operator and solved with the NCAR cyclic reduction subroutine package. Finite differences are of second-order accuracy, so the total discretization error is $O(h^2 + \Delta t^2)$.

For linear problems ($\epsilon = 0$), vorticity on the boundary Σ does not enter the problem in either the vorticity equation or the Poisson equation. For nonlinear problems ($\epsilon \neq 0$), vorticity is specified at inflow points according to the Charney-Fjortoft-von Neumann boundary condition [18]. Centered finite differences require boundary data everywhere, and in contrast to the analytic problem, some auxiliary relationship (that is, a computational boundary condition) must be assumed at outflow points in order to determine the vorticity there (unless an iterative technique is used to fix ζ on Σ).

Optimally, the computational boundaries of an open ocean model should be transparent to signals impinging on them. Thus, the formation

of boundary layers on or wave reflections from the boundary are undesirable. The most successful computational boundary condition considered in this study is

$$\zeta_B^k + \zeta_{B-2}^k = \zeta_{B-1}^{k+1} + \zeta_{B-1}^{k-1} \quad (6)$$

which was introduced by Sundstrom [16]. Here B, B-1, B-2 represent a boundary point and its 1st and 2nd normal interior neighbors. Davies [17] demonstrated the stability properties of this closure for a variety of nonlinear problems.

There are several possible physical interpretations of statement (6): either (a) it is equivalent to equating the time and spatial averages of ζ at point B-1 (a kind of smoothness condition at outflow); (b) Eq. (6) is equivalent to $\zeta_{tt} = c^2 \zeta_{xx}$ where $c = \Delta x / \Delta t$ (a "local" wave equation); or (c) it is a low-order spatial extrapolation scheme.

In order to implement the Sundstrom/Davies formula, the quantity ζ_{B-1}^{k+1} is eliminated by application of the vorticity equation evaluated at the point B-1, $t = k\Delta t$. This yields an implicit set of equations for the boundary vorticity. Formally, this requires the inversion of a heptadiagonal matrix with cyclic ordering of the points. However, it can be shown that by elimination of those boundary points which are corner neighbors, a simple tridiagonal system results, provided there is at least one inflow point (Appendix I). Note that the boundary vorticity is calculated after the interior vorticity and the streamfunction.

Other computational boundary conditions investigated in this study are the Kreiss extrapolation $\zeta_B^k = 2\zeta_{B-1}^k - \zeta_{B-2}^k$ [11] and the condition $\zeta_\Sigma = \zeta_a$.

3.2 Finite-element model

In the finite-element formulation, we assume a set of basic functions consisting of piecewise polynomials, the simplest being piecewise linear elements arranged in a rectangular lattice. In one dimension, each

element is a chapeau or hill function, and in two dimensions, a pyramidal function, each centered on the lattice point with base width $2h$ [22].

Then the basis functions have the property

$$\phi_q(\underline{z}_p) = \begin{cases} 1 & \text{if } p = q \\ 0 & \text{if } p \neq q \end{cases} \quad (7)$$

where \underline{z}_p is the p -th lattice point. All fields can be expressed in terms of a summation of the basis functions; for instance,

$$\psi(\underline{x}, t) = \sum_q \psi_q(t) \phi_q(\underline{x}) \quad (8)$$

$$\zeta(\underline{x}, t) = \sum_q \zeta_q(t) \phi_q(\underline{x}) \quad (9)$$

where \underline{x} is a general point within the domain.

The weights ψ_q and ζ_q are obtained by the Galerkin procedure. Substitute (8) and (9) into the vorticity equation, multiply by a basis function and integrate over the entire region. Since each element overlaps those adjacent to it, in general each equation will contain terms from its eight neighbors.

For closed-domain problems, we use centered time differences. The resulting finite-element form of the vorticity equation is

$$M(\zeta^{k+1}) = M(\zeta^{k-1}) - 2\Delta t Q^k = P^{k+1} \quad (10a)$$

where

$$Q^k = \frac{\epsilon}{h^2} J^*(\psi^k, \zeta^k) - \frac{1}{2h} W^{(y)} \delta_x(\psi^k) .$$

In partially and completely open domains, however, a second-order Adams-Bashforth time-differencing scheme is used to avoid computational instability. In such cases,

$$M(\zeta^{k+1}) = M(\zeta^k) - \Delta t \left\{ \frac{3}{2} Q^k - \frac{1}{2} Q^{k-1} \right\} . \quad (10b)$$

The mass matrix M has the entries $M_{pq} = \iint \phi_p \phi_q dA$. M is factorable into two parts, $M = W^{(x)} \otimes W^{(y)}$, where \otimes denotes tensor multiplication and the matrices $W^{(x)}$ and $W^{(y)}$ are tridiagonal with the local form $1/6(1 \ 4 \ 1)$. The operator $W^{(x)} \otimes W^{(y)}$ can be interpreted to mean successive multiplications--first rowwise, then columnwise--by the matrix $W = W^{(x)} = W^{(y)}$. Note that the superscripts (x) and (y) refer to the order in which the tridiagonal multiplications are done. At each time step, therefore, Eq. (10) can be written

$$M(\zeta^{k+1}) = W^{(x)} \otimes W^{(y)}(\zeta^{k+1}) = P^{k+1}$$

where ζ^{k+1} is the $N \times N$ matrix of values of ζ at time step $(k+1)$. In this form, it is clear that Eq. (10a) is equivalent to two tridiagonal matrix systems each of size $N \times N$. The mass matrix can therefore be readily inverted. Note that if W is set equal to the identity matrix, Eq. (10a) reduces to the finite-difference form (5a). The Jacobian term is precisely the Arakawa Jacobian employed with finite differences. In fact, the Arakawa form is derivable from the finite-element formulation [24].

Fix [22] has shown that linear elements for the linearized advective equation $\zeta_t + U\zeta_x = 0$ produce fourth-order accurate phase errors. To maintain this accuracy for the vorticity equation, the solution of the Poisson equation for the streamfunction must also be of fourth order. This is accomplished by the method of deferred corrections [25]. Note that

$$K(\psi) = h^2 \nabla^2 \psi + \frac{1}{12} h^4 \left(\nabla^4 - 2 \frac{\partial^4}{\partial x^2 \partial y^2} \right) \psi + O(h^6)$$

where K is the usual five-point Laplacian

$$K = \begin{pmatrix} 0 & 1 & 0 \\ 1 & -4 & 1 \\ 0 & 1 & 0 \end{pmatrix}.$$

Therefore two successive Poisson solutions yield ψ to fourth order in the following manner. First, obtain a second-order solution, ψ_1 , from $K(\psi_1) = h^2 \zeta$. Then, a fourth-order estimate of ψ is the solution to

$$K(\psi) = h^2 \zeta + \frac{h^4}{12} \left(\nabla^2 \zeta - 2 \frac{\partial^4}{\partial x^2 \partial y^2} \psi_1 \right). \quad (11)$$

Finite elements require more computational work per time step than do finite differences. First, two tridiagonal inversions must be performed to determine the vorticity field, contrasted with a simple direct substitution in finite differences. Second, two calls must be made to the Poisson solver instead of one. The significant increase in accuracy plus the virtue of using a technique based on a variational principle justify this increased computational effort in many applications, as indeed they will here (see, for instance, Section 7).

In the finite-element model, vorticity boundary conditions are implemented in the following manner. For ease of presentation, we introduce three types of points and their respective computational molecules m , that is, their local contribution to mass matrix M :

$$(a) \quad \text{interior points} \quad m_I = 1/36 \begin{pmatrix} 1 & 4 & 1 \\ 4 & \underline{16} & 4 \\ 1 & 4 & 1 \end{pmatrix} \quad (12a)$$

$$(b) \quad \text{regular boundary points} \quad m_E = 1/36 \begin{pmatrix} 0 & 1 & 2 \\ 0 & 4 & \underline{8} \\ 0 & 1 & 2 \end{pmatrix} \quad \begin{matrix} \text{(Eastern wall)} \\ (12b) \end{matrix}$$

and

$$(c) \quad \text{corner points} \quad m_{SE} = 1/36 \begin{pmatrix} 0 & 0 & 0 \\ 0 & 1 & 2 \\ 0 & 2 & \underline{4} \end{pmatrix} \quad \begin{matrix} \text{(Southeast} \\ \text{corner)} \\ (12c) \end{matrix}$$

The lattice point associated with the given element is denoted by the underline. Analogous computational molecules exist, for regular boundary points on the northern, southern and western walls and for the southwest, northwest and northeast corner points.

Assume first that vorticity is specified everywhere on the boundary (corresponding to inflow everywhere) and solutions are needed only for

the interior points. It is then easy to show that this is equivalent to the system of equations:

$$M_4(\zeta^{k+1}) = P_4 \quad (13)$$

where

$$P_4 = \begin{cases} P & \text{for interior points} \\ P - \begin{pmatrix} 1 \\ 4 \\ 1 \end{pmatrix} \zeta_B/36 & \text{at (eastern) boundary} \\ P - \begin{pmatrix} 0 & 0 & 1 \\ 0 & 0 & 4 \\ 1 & 4 & 1 \end{pmatrix} \zeta_B/36 & \text{at (southeast) corner} \end{cases} \quad (14)$$

ζ_B is the specified boundary vorticity, and $M_4 = W_4^{(x)} \otimes W_4^{(y)}$, where $W_4 (= W_4^{(x)} = W_4^{(y)})$ is the $(N-2) \times (N-2)$ tridiagonal matrix

$$W_4 = 1/6 \begin{pmatrix} 4 & 1 & & & \\ 1 & 4 & 1 & & \\ & 1 & 4 & 1 & \\ & & 1 & 4 & 1 \\ & & & 1 & 4 \end{pmatrix} \quad (15)$$

The subscript (4) refers to the corner terms in (15).

Next consider the case where vorticity is not specified anywhere on the boundary, as in a basin totally enclosed by solid and/or outflow sides. Here solutions are sought for the entire field (interior, boundary and corner points). It is then easy to show that the combined system including contributions of the form (12a-c) is equivalent to

$$M_2(\zeta^{k+1}) = P_2 \quad (16)$$

where $M_2 = W_2^{(x)} \otimes W_2^{(y)}$, and

$$W_2 = 1/6 \begin{pmatrix} 2 & 1 & & & \\ 1 & 4 & 1 & & \\ & 1 & 4 & 1 & \\ & & 1 & 4 & 1 \\ & & & 1 & 2 \end{pmatrix} \quad (17)$$

is now $N \times N$.

These two cases represent extreme situations--either all inflow, or all outflow (and/or solid boundaries). We seek a method which will allow a general mix of inflow and outflow sections around the boundary. We can do this by defining a new matrix, $M_{7/2}$, which has the following computational structure

$$M_{7/2} = \begin{cases} m_I & \text{for points not at or adjacent to the boundary } (i, j \neq 1, 2, N-1, N) \\ m_I - \frac{1}{2} m_E & \text{for interior points adjacent to the (eastern) boundary but not near a corner } (i = N-1, j \neq 2 \text{ or } N-1) \\ m_I - \frac{1}{2} m_E - \frac{1}{2} m_S + \frac{1}{4} m_{SE} & \text{for interior corner (southeast) points } (i = N-1, j = 2) \end{cases} \quad (18)$$

and so on for points adjacent to other boundaries and corners.

It can be shown that this new formulation decouples the determination of the interior vorticity from that of the boundary vorticity and is equivalent to

$$M_{7/2}(\zeta^{k+1}) = P_{7/2} \quad (19)$$

where $P_{7/2}$ has the same relationship to P as $M_{7/2}$ to M given in (18). In addition, $M_{7/2} = W_{7/2}^{(x)} \otimes W_{7/2}^{(y)}$ where

$$W_{7/2} = \frac{1}{6} \begin{pmatrix} 7/2 & 1 & & & \\ & 4 & 1 & & \\ & & & 1 & \\ & & & & 4 & 1 \\ & & & & & 1 & 7/2 \end{pmatrix}, \quad (20)$$

and all of the unknowns are interior points. In short, we use the known dynamic relations between boundary and interior points to disconnect the solution of the one from the other.

Furthermore, given the interior values from the inversion of $M_{7/2}$, each of the four boundaries decouples from the other boundaries and all of the corners--for instance by defining a new matrix

$$M'_E = M_E - \frac{1}{2} M_{SE} - \frac{1}{2} M_{NE} \quad (21)$$

at the eastern boundary. The solution for the boundary values requires 4 inversions (one for each wall) of a tridiagonal system. The corner point values then follow algebraically. In the finite-element approximation, the order of calculation is therefore the following: interior vorticity, vorticity at regular boundary points, vorticity at corner points, and lastly the streamfunction. The reader should note, however, that this solution procedure does not strictly guarantee that values of vorticity on, or adjacent to, points of inflow be in exact dynamic balance.

3.3 Pseudospectral Model

We seek a (discrete) spectral solution to Eq. (3) subject to some appropriate set of boundary and initial conditions. For definiteness, consider specifying boundary values of streamfunction and vorticity in the manner first suggested by Charney, Fjortoft and von Neumann [18]. That is, we take as given quantities the values of ψ everywhere along Σ , and ζ at those points along Σ characterized by mass influx. Boundary values of vorticity at outflow points are therefore unconstrained; they are computed as part of the calculation. Under these boundary conditions, a completely enclosed domain is a special case, one for which--owing to the absence of any inflow at all--vorticity need never be specified at any time along Σ . In analogy to the analytic problem, we make a computational distinction between problems contained within bounded regions and those characterized by partially or fully open domains.

3.3.1 Closed domain

In a closed system, the advective terms in Eq. (3) are treated explicitly by a leapfrog time-differencing scheme. Under this second-order approximation, the vorticity and Poisson equations become, in the usual notation,

$$\begin{aligned}\zeta^{k+1} &= \zeta^{k-1} - 2\Delta t \left\{ \epsilon J(\psi^k, \zeta^k) + \psi_x^k \right\} \\ &= R^{k+1}(x, y)\end{aligned}\tag{21}$$

and

$$\nabla^2 \psi^{k+1} = \zeta^{k+1} .\tag{22}$$

In space, we adopt a pseudospectral approximation technique for which the dependent variables are expanded in a series of Chebyshev polynomials; that is, let:

$$\psi^k(\hat{x}, \hat{y}) = \sum_{n=0}^N \sum_{m=0}^N a_{nm}^k T_n(\hat{x}) T_m(\hat{y}) \quad -1 \leq \hat{x}, \hat{y} \leq +1 \quad (23a)$$

$$\zeta^k(\hat{x}, \hat{y}) = \sum_{n=0}^N \sum_{m=0}^N b_{nm}^k T_n(\hat{x}) T_m(\hat{y}) \quad (23b)$$

and

$$R^k(\hat{x}, \hat{y}) = \sum_{n=0}^N \sum_{m=0}^N R_{nm}^k T_n(\hat{x}) T_m(\hat{y}) \quad (23c)$$

where

$$\hat{x} = (2x - x_B)/x_B$$

$$\hat{y} = (2y - y_B)/y_B$$

and $T_n(\hat{x}) = \cos(n \cos^{-1} \hat{x})$ is the Chebyshev polynomial (of the first kind) of degree n , a function of the linearly stretched coordinates \hat{x} and \hat{y} . On the collocation grid $(\hat{x}_p, \hat{y}_q) = (\cos(\pi p/N), \cos(\pi q/N))$, $0 \leq p, q \leq N$, this implies for instance that

$$\psi^k(\hat{x}_p, \hat{y}_q) = \sum_{n=0}^N \sum_{m=0}^N a_{nm}^k \cos \left\{ \frac{\pi p n}{N} \right\} \cos \left\{ \frac{\pi q m}{N} \right\},$$

demonstrating the important fact that a Chebyshev transform is equivalent to a cosine transform on the (non-uniform) collocation grid (\hat{x}_p, \hat{y}_q) and as such can be implemented very efficiently using special forms of the fast Fourier transform algorithm [26].

Under these definitions, Eqs. (21) and (22) can be rewritten in terms of the spectral coefficients a_{nm} , b_{nm} , and R_{nm} :

$$b_{nm}^{k+1} = R_{nm}^{k+1} \quad 0 \leq n, m \leq N \quad (24)$$

and

$$[a^{xx} + a^{yy}]_{nm}^{k+1} = b_{nm}^{k+1} \quad 0 \leq n, m \leq N \quad (25)$$

where a_{nm}^{xx} and a_{nm}^{yy} satisfy

$$\begin{aligned} \frac{\partial^2}{\partial x^2} \psi &= \frac{\partial^2}{\partial x^2} \sum_{n=0}^N \sum_{m=0}^N a_{nm} T_n(\hat{x}) T_m(\hat{y}) \\ &= \sum_{n=0}^N \sum_{m=0}^N a_{nm}^{xx} T_n(\hat{x}) T_m(\hat{y}) \end{aligned}$$

and

$$\begin{aligned} \frac{\partial^2}{\partial y^2} \psi &= \frac{\partial^2}{\partial y^2} \sum_{n=0}^N \sum_{m=0}^N a_{nm} T_n(\hat{x}) T_m(\hat{y}) \\ &= \sum_{n=0}^N \sum_{m=0}^N a_{nm}^{yy} T_n(\hat{x}) T_m(\hat{y}) \end{aligned}$$

Unlike periodic models, the resulting spectral scheme can accommodate quite arbitrary boundary conditions on Σ . In the present bounded geometry, $\psi(x, y)$ is given on the boundary by some set of values, let us say ψ_Σ . In terms of the spectral coefficients a_{nm} , this is equivalent to requiring that

$$\sum_{n=0}^N \left[\sum_{m=0}^N a_{nm} T_m(\hat{y}_q) \right] = \psi_\Sigma(+1, y_q) \quad 0 \leq q \leq N \quad (26a)$$

$$\sum_{n=0}^N (-1)^n \left[\sum_{m=0}^N a_{nm} T_m(\hat{y}_q) \right] = \psi_\Sigma(-1, y_q) \quad 0 \leq q \leq N \quad (26b)$$

$$\sum_{m=0}^N \left[\sum_{n=0}^N a_{nm} T_n(\hat{x}_p) \right] = \psi_\Sigma(x_p, +1) \quad 0 \leq p \leq N \quad (26c)$$

and

$$\sum_{m=0}^N (-1)^m \left[\sum_{n=0}^N a_{nm} T_n(\hat{x}_p) \right] = \psi_\Sigma(x_p, -1). \quad 0 \leq p \leq N \quad (26d)$$

These conditions are imposed on the Poisson equation (22) by using the spectral analogue of the tau method [27], that is by neglecting the highest

order dynamic equations--those for $n = N-1, N$ and $m = N-1, N$ --in (25). The remaining equations are then supplemented by boundary conditions (26a-d), written in their equivalent Chebyshev series form, to close the problem. The resulting matrix equations are not sparse; however, they are quite easily diagonalized. The details of the solution have been given by Haidvogel and Zang [28] who show that, for sufficiently smooth fields and given accuracy, solutions to Poisson's equation can be computed at least as efficiently by these spectral techniques as by certain second and fourth-order finite-difference methods.

Once the spectral coefficients a_{nm}^{k+1} have been determined, thus yielding $\psi(x, y)$ at the next time level, the velocity components $u = -\psi_y$ and $v = +\psi_x$ can be computed from well known Chebyshev derivative relations. These in turn are combined to give the nonlinear term $J(\psi, \zeta) = \nabla \cdot (\underline{v}\zeta)$ by the simple pseudospectral procedure

$$\nabla \cdot (\underline{v}\zeta) \big|_{p,q} = \frac{\partial}{\partial x} [u(\hat{x}_p, \hat{y}_q) \zeta(\hat{x}_p, \hat{y}_q)] + \frac{\partial}{\partial y} [v(\hat{x}_p, \hat{y}_q) \zeta(\hat{x}_p, \hat{y}_q)]$$

where the product $\underline{v}\zeta$ is determined locally by physical space multiplications on the collocation grid (\hat{x}_p, \hat{y}_q) but the derivatives $\partial/\partial x$ and $\partial/\partial y$ are performed spectrally. The resulting scheme is of infinite-order accuracy and can be constructed so as to conserve any of the higher order invariants such as energy and enstrophy; however, it retains the effects of high wavenumber aliasing at full strength [29]. The effects of aliasing can be identically removed, but at a large cost in computational efficiency (approximately a factor of 2).

3.3.2 Open domain

In the spectral approximation, boundary conditions can only be correctly applied if the highest-order terms are treated in some way implicitly. For those problems in which the domain of integration is not bounded by an impermeable surface and for which, therefore, values of the vorticity are to be specified at points of inflow, this implies that the advective term must be treated somewhat differently than in a closed region. To do so, we adopt the following alternating direction implicit (ADI) time-differencing scheme.

$$\begin{aligned} \zeta^{k+1/2} + \frac{\epsilon \Delta t}{2} \frac{\partial}{\partial x} (u_0 \zeta)^{k+1/2} &= L_1(\zeta^{k+1/2}) = \zeta^k - \frac{\epsilon \Delta t}{2} \frac{\partial}{\partial y} (v_0 \zeta)^k \\ &- \frac{3\Delta t}{4} \{ \epsilon \nabla \cdot [(\underline{v} - \underline{v}_0) \zeta] + \psi_x \}^k + \frac{\Delta t}{4} \{ \epsilon \nabla \cdot [(\underline{v} - \underline{v}_0) \zeta] + \psi_x \}^{k-1/2} \end{aligned} \quad (27a)$$

$$\begin{aligned} \zeta^{k+1} + \frac{\epsilon \Delta t}{2} \frac{\partial}{\partial x} (v_0 \zeta)^{k+1} &= L_2(\zeta^{k+1}) = \zeta^{k-1/2} - \frac{\epsilon \nabla t}{2} \frac{\partial}{\partial x} (u_0 \zeta)^{k+1/2} \\ &- \frac{3\Delta t}{4} \{ \epsilon \nabla \cdot [(\underline{v} - \underline{v}_0) \zeta] + \psi_x \}^{k+1/2} + \frac{\Delta t}{4} \{ \epsilon \nabla \cdot [(\underline{v} - \underline{v}_0) \zeta] + \psi_x \}^k \end{aligned} \quad (27b)$$

where

$$u_0^{k+1}(\hat{x}, \hat{y}) = \left(\frac{\hat{x}+1}{2} \right) \{ u^{k+1}(1, y) - u^{k+1}(-1, y) \} + u^{k+1}(-1, y)$$

$$v_0^{k+1}(\hat{x}, \hat{y}) = \left(\frac{\hat{x}+1}{2} \right) \{ v^{k+1}(x, 1) - v^{k+1}(x, -1) \} + v^{k+1}(x, -1)$$

and

$$u^{k+1}(-1, y), \quad u^{k+1}(+1, y), \quad v^{k+1}(x, +1) \quad \text{and} \quad v^{k+1}(x, -1)$$

are the known distributions of normal velocity at time step $(k+1)$ along the western, eastern, northern, and southern boundaries, respectively. In effect, this semi-implicit procedure removes and treats implicitly that portion of the advective term which arises from contributions due to non-zero normal velocities at the domain edges. Besides assuring stability of the computational scheme, the splitting of the advective term relaxes the restrictive Courant condition which arises for explicitly differenced inflow/outflow problems due to the crowding of Chebyshev collocation points near the domain boundaries.

The solution of each half step--Eq. (27a) or (27b)--proceeds similarly. Consider (27a). The implicit advective effects introduce a coupling only the x direction. In fact, along any line $\hat{y} = \hat{y}_q = \text{constant}$, $u_0^{k+1}(\hat{x}, \hat{y}_q)$ is at most linear in \hat{x} . Under these circumstances, operator

$L_1(\zeta^{k+1/2})$ can be expressed spectrally as a sequence of tridiagonal matrix equations, one for each \hat{y}_q ($0 \leq q \leq N$). Similar remarks hold for operator $L_2(\zeta^{k+1})$ which is repeatedly solved along lines of constant $\hat{x} = \hat{x}_p$ ($0 \leq p \leq N$). In either case, vorticity boundary conditions are selectively introduced in place of higher order (dynamical) equations in each tridiagonal system. Zero, one or two vorticity conditions are imposed depending on the corresponding number of end points of the line $\hat{x} = \hat{x}_p$ or $\hat{y} = \hat{y}_q$ which are inflow points. The resulting numerical scheme fixes the value of ζ only at inflow points; however, all values of boundary vorticity are in exact dynamic balance with the interior. (This is not true of either the FD or FE models--see the preceding sections.) Note that problems involving inflow only in one coordinate direction--such as the north wall forcing problem to be discussed shortly--can be handled in a single step.

Once Eqs. (27a) or (27b) yield $\zeta^{k+1/2}$ or ζ^{k+1} , the associated Poisson problem for the streamfunction fields $\psi^{k+1/2}$ or ψ^{k+1} are solved as outlined above for a closed basin.

4. LINEAR AND NONLINEAR BOX MODE TESTS

In this and the following sections, we briefly describe the formulation and selected results of the prototype numerical tests mentioned in Section 1. For a more complete summary of the results, the reader is referred to Table I and Figures 1-27. (See also Section 2, pages 5-8.)

4.1 Formulation

The class of exact solutions to the linear vorticity equation ($\epsilon = 0$) satisfying homogeneous streamfunction boundary conditions on Σ are the box modes or normal modes of the basin. These can be written

$$\begin{aligned} \psi(x, y, t) &= \sin(\lambda x) \sin(\mu y) \cos(x+t/2) & 0 \leq x \leq x_B \\ & & 0 \leq y \leq y_B \end{aligned} \quad (28)$$

where x and t have been scaled with respect to d and $(\beta d)^{-1}$, respectively and d is taken to be the scale length of the travelling wave (wavelength/ 2π). The parameters λ and μ , and the domain size $x_B = y_B$ are related to the integer mode numbers, m and n , by the relations

$$\lambda = m/(m^2 + n^2)^{1/2}$$

$$\mu = n/(m^2 + n^2)^{1/2}$$

and

$$x_B = y_B = \pi(m^2 + n^2)^{1/2}.$$

Given this nondimensionalization, the linear box modes have a wavelength, period and phase speed given by 2π , 4π , and $1/2$, respectively. Corresponding to these physical measures are the computational measures

$$\Delta = x_B/\pi \quad \approx \quad \text{relative box size}$$

$$\nu = (N-1)/\Delta = (N-1)\pi/x_B \quad \approx \quad \text{spatial resolution parameter}$$

and

$$\eta = 4\pi/\Delta t = \text{temporal resolution parameter.}$$

As mentioned previously, we use N to refer to the number of spatial degrees of freedom (grid points, spectral functions, etc.) which characterizes the x and y discretization of each model.

For $\epsilon \ll 1$, we can obtain an approximate solution to the non-linear box mode problem using a small amplitude expansion in ϵ . Let

$$\psi(x, y, t) = \psi_0 + \epsilon \psi_1 + \epsilon^2 \psi_2 + \dots$$

where ψ_0 is the linear box mode solution (28). Then, to first order

$$\nabla^2 \psi_{1t} + \psi_{1x} = -J(\psi_0, \nabla^2 \psi_0) \quad (29)$$

which has the solution

$$\begin{aligned} \psi_1(x, y, t) = \sin(2\mu y) \left\{ -\frac{\mu}{2} \sin^2 \lambda x + \frac{\lambda^2 \mu}{4(1+2\mu^2)} \left[\cos(t + 2x) \right. \right. \\ \left. \left. - \left(\frac{\sinh Rx}{\sinh Rx_B} \right) \cos \left(t + \frac{x}{2} + \frac{3x_B}{2} \right) - \frac{\sinh R(x_B - x)}{\sinh Rx_B} \cos(t + x/2) \right] \right\} \end{aligned} \quad (30)$$

with

$$R = (4\mu^2 - 1/4)^{1/2}, \quad \mu > 1/4.$$

Taking the expansion to second order, the right hand side of the equation for ψ_2 has a component proportional to ψ_0 . This secularity destroys the uniform convergence of the approximation for large t . Following Pedlosky [30], it can be shown that by introducing the new time scale $\tau = t(1 + \epsilon^2 \delta)$, all forcing terms proportional to ψ_0 can be suppressed for a suitable choice of δ . The perturbation solution $\psi = \psi_0 + \epsilon \psi_1$ can therefore be corrected by replacing t by τ in (28) and (30). The resulting expression is correct to first order; that is, its leading-order error is $O(\epsilon^2)$. Since the computed solution can be closer

to (or further away from) the correct nonlinear solution than the approximate analytic solution, the RMS error is an unknown mix of errors in both the computed and approximate solutions.

4.2 Finite-difference model results (Table I, cases 1-9; Figures 1-6)

An exact solution, ψ_d , to the discrete finite-difference Eqs. (5a) and (5b) can be found by assuming

$$\psi_d(x, y, t) = \sin(\lambda x) \sin(\mu y) \cos(\alpha x + \sigma t) \quad (31)$$

where α and σ are, in general, functions of the nondimensional space and time increments h and Δt . (We therefore assume that the discrete and analytic results differ only in the wavelength and phase speed of the travelling component of the box mode.) Substituting in the trial solution (31), we find that

$$\sin(\sigma \Delta t) = 1/2 h \Delta t$$

and

$$\cos(\alpha h) = \frac{\cos h(\lambda h)}{2 - \cos(\mu h)}$$

For $h \ll \pi$ and $\Delta t \ll \pi$,

$$\alpha = 1 - \frac{\mu^2}{12} (2 + \mu^2) h^2 + O(h^4)$$

and

$$\sigma = 1/2 + 1/48 \Delta t^2 - 1/24(4 - 2\mu^2 - \mu^4) h^2 + O(\Delta t^4 + h^4)$$

That this is indeed the correct computational result has been verified by direct numerical integration of the finite-difference equations (5a) and (5b). The resulting computational solution differs from (31) only due to machine truncation error--that is, $\text{RMS}(\zeta') = \text{RMS}(\zeta_c - \zeta_d) = O(10^{-11})$.

In comparison to the analytic solution (for which $\alpha = 1$ and $\sigma = 1/2$), the wavelength and period are correct only to second order in space and

time. For sufficiently small phase errors $\phi (= \sigma_a - \sigma_d)$, it is easy to show that

$$\text{RMS}(\psi') = [2(1 - \cos \phi t)]^{1/2}.$$

The initial error growth rate

$$\text{RMS}(\psi') \approx \phi t + O(\phi t)^3, \quad (32)$$

is therefore linear in time with a slope given by

$$\begin{aligned} \phi &= (1/48)\Delta t^2 - 1/24(4 - 2\mu^2 - \mu^4)h^2 \\ &\approx (\pi^2/3)\eta^{-2} - \pi^2/24(4 - 2\mu^2 - \mu^4)\nu^{-2}. \end{aligned} \quad (33)$$

An example of this behavior is given in Figure (3a, b) for $(\nu, \eta, m, n) = (16\sqrt{2}, 128, 1, 1)$.

Note that for the discrete finite-difference solution, the spatial and temporal contributions to the phase error ϕ , being of opposite sign, tend to offset each other. Because of this compensation effect, if an optimal choice of Δt and h is made, the total error of the finite-difference scheme can be made quite small although the contributions to ϕ from spatial and temporal error are individually large. This property explains the computed results as a function of $\nu (\approx \pi/h)$ and $\eta (= 4\pi/\Delta t)$ in which increasing η (holding ν fixed), and vice-versa, can increase, rather than decrease the error of the computed finite-difference solution. Compare, for instance, Table 1, cases 2 and 3.

For $\epsilon > 0$, the values of ζ on the boundary enter the problem through the nonlinear terms. Three ways of fixing ζ_Σ have been examined in the context of the finite-difference model. They are the specification of the analytic value of the vorticity ($\zeta_\Sigma = \zeta_a$), and the Kreiss and Sundstrom/Davies conditions--see Section 3. For the non-linear box mode problems studied, the following behavior was noted.

4.2.1 $\epsilon = 0.2$

For low to moderate Rossby number the FD model is always well behaved out to at least $t = 5$ periods independent of computational

boundary condition. When $\zeta_{\Sigma} = \zeta_a$ is the required condition, however, there is a buildup of small-scale perturbation vorticity on the western wall--Figure 6a. (Since similar effects are noted in all the models, this buildup is presumably a manifestation of the physical response of the system to the presence of small-scale numerical truncation error.) This accumulation of ζ' is less rapid when the Kreiss boundary condition is applied everywhere (Figure 6b) and is nearly eliminated when the Sundstrom/Davies condition is invoked (Figure 6c). The RMS error measures are, however, comparably large--several tens of percent after five periods--for all three boundary conditions (Table 1, case 6).

4.2.2 $\epsilon = 0.4$

For higher Rossby number, the error accumulation to the west is much more rapid and becomes noticeable in even the Sundstrom/Davies experiments. In contrast to the finite-element and spectral models, however, the finite-difference scheme does not suffer catastrophic numerical instability when grid-scale vorticity begins to accumulate. This lower sensitivity to the presence of small-scale vorticity is perhaps due to a small amount of (numerical) dissipation implicit in the finite-difference formalism.

In general, the RMS error quantities have a linearly increasing trend similar to, but somewhat greater than, that noted for $\epsilon = 0$. Some our approximate reference solution.

4.3 Finite-element model results (Table I, cases 1-9; Figures 1-5)

The following functional dependence on the parameters ν and η has been noted in the error analysis of the finite-element model results.

4.3.1 $\eta \ll 4\sqrt{2} \nu$

For relatively coarse temporal resolution, the RMS error quantities are well described, as in the finite-difference and spectral models, by the relation $\phi \approx (\pi^2/3)\eta^{-2}$ and consequently by an initial linear increase with time proportional to η^{-2} . This reflects the fact that for sufficiently large ν the error is attributable to temporal truncation effects (identical in all three models).

4.3.2 $\eta \approx 4\sqrt{2} \nu$

As η increases, $\text{RMS}(\zeta')$ for the finite-element is characterized by a large initial value followed by a very slow linear increase thereafter (Figure 3c). ($\text{RMS}(\psi')$ --whose values are perhaps dictated by a different mechanism than those of $\text{RMS}(\zeta')$ --maintains a linear trend.) Apparently, the spatial contribution to the phase error ϕ is of a form quite different than that implied by (33). For one thing, we know the phase error to be proportional to h^4 for the linearized advective equation [22]. In parameter ranges where this diminished error growth rate prevails, the finite-element model may offer some advantages for long-term calculations; however, we have not verified this possibility.

For $\epsilon = 0$, the maximum pointwise errors in vorticity tend to be near the western boundary, but there is very little preferential accumulation of small-scale vorticity there. With nonlinearity ($\epsilon > 0$), the situation is qualitatively different in the following way(s).

4.3.3 $\epsilon = 0.2$

With $\epsilon = 0.2$, an initial eastern boundary layer is generally observed in the field of ζ' . This boundary layer eventually disappears, to be replaced by an accumulation of perturbation vorticity on the western wall, as in the FD and PS simulations (Figure 5c). In other

respects, the solutions bear some resemblance to those for $\epsilon = 0$. $\text{RMS}(\zeta')$ again shows evidence--for certain values of ν and η --of levelling off with time after an initially large increase, and ψ' sometimes resembles a box mode (out of phase with the reference solution).

4.3.4 $\epsilon = 0.4$

With stronger nonlinearity, perturbation vorticity on the grid-point scale collects first on the western wall and then in the center of the domain (perhaps as a numerical response to insufficient resolution of the narrow wall layers of ζ'). Once this stage is reached, the solution becomes numerically unstable, typically after about 5 periods (Table I, case 7).

This catastrophic effect of small-scale vorticity accumulation is reached in less than a period for $\epsilon = 0.8$.

4.4 Pseudospectral model results (Table I, case 1-9; Figures 1-5, 7)

For linear box modes, for which we have the analytic solution, the spectral model shows three distinct types of behavior corresponding to different regimes in the space of the nondimensional computational parameters.

4.4.1 $\nu \geq 4\sqrt{2}$, $\eta \leq 128$ ($\eta < 16\sqrt{2}\nu$)

Quite a large range of ν exists for which spatial truncation errors are totally insignificant in comparison to those arising from time-differencing. For this range of parameters, the RMS quantities grow linearly in time (Figures 3e, f) and can be quantitatively explained by the simple phase error analysis of Section 4.2 if, in addition, the assumption is made that $h \approx 0$. There is no apparent buildup of perturbation vorticity at scales other than those of the box modes themselves. Since the computational errors are due to time-differencing alone, they are proportional to η^{-2} --see Table I, cases 1 and 2.

$$4.4.2 \quad \frac{8\sqrt{2}}{3} \leq \nu \leq 4\sqrt{2}, \quad \eta \leq 128 \quad (\eta \approx 16\sqrt{2}\nu)$$

For $\nu \approx 4$ and standard values of η (= 64 or 128), spatial error becomes noticeable. The growth of the RMS quantities is no longer strictly linear. In fact, the temporal variation of $\text{RMS}(\zeta')$ begins to assume characteristics noted (over a larger range of ν and η) in the finite-element model: a large initial error growth, followed by a relatively slow increase with time. Indeed, it is interesting to note that the spectral model can show the effects of compensating space and time-differencing errors which is a general property of finite-difference model. Something of this kind is clearly happening in the spectral model when, for instance, $\text{RMS}(\psi')$ decreases when the box mode numbers $m = n$ are increased from two to three at constant ν and η (Table I, cases 4 and 5). For these values of ν , perturbation vorticity does appear to collect on the western wall, perhaps in scales much smaller than those of the original box modes.

$$4.4.3 \quad \nu \leq 2\sqrt{2}, \quad \eta \leq 128 \quad (\eta \gg 16\sqrt{2}\nu)$$

As expected, for extremely small values of the resolution parameter ν , substantial spatial error results. The RMS error quantities once again grow in a quasilinear fashion. The perturbation vorticity field is now dominated by a narrow layer on the western wall. The amplitude of this feature is sufficiently large (after 10 periods) as to contribute recognizably to the total vorticity field.

For the nonlinear box modes, behavior of the computational system depends sensitively on ϵ in the following manner.

$$4.4.4 \quad \epsilon = 0.2$$

For $\epsilon \leq 0.2$, the spectral model is well behaved out to $t \approx 5$ periods. By this time, however, integrated $|\nabla\zeta|^2$ has begun to increase rapidly. Significantly longer integrations could therefore be expected to suffer eventual computational instability. Even at this level of nonlinearity, increasing ν and/or η (over the range tested: $\nu \leq 8\sqrt{2}$, $\eta \leq 128$) does nothing to improve the error measures (Table I, cases 6,

8,9). The manifestation of error growth is a very definite preferential accumulation of perturbation vorticity in narrow layers adjacent to the western wall of the domain (Figure 5e). This accumulation of perturbation vorticity may ultimately result from local numerical truncation errors which are propagated to the west where, in the absence of dissipation, they collect in a narrow boundary layer.

4.4.5 $\epsilon = 0.4$

The results for $\epsilon = 0.4$ are much more catastrophic, with perturbation vorticity collecting so quickly on the western wall that locally intense gradients of vorticity grow to destroy the calculation after only 2.5 periods (Table I, case 7). This behavior is once again independent of ν and η . When the calculations go bad, they do so very quickly; presumably the computed fields are still quite accurate up to the instant of catastrophic failure. (This essentially instantaneous instability is a feature of the FE model also.) In a related calculation, it has been shown that the useful integration of the spectral model can be prolonged to $t = 5$ periods (and beyond) by periodically filtering the vorticity field by setting

$$b_{nm}^k(\text{filtered}) = f_n f_m b_{nm}^k$$

(see Section 3.3) where the spectral filter

$$f_n = 1.0 - \exp\{-\mathcal{H}(N^2 - n^2)\}$$

and \mathcal{H} is adjusted so that ζ^k is smoothed only at the highest wavenumbers. By comparing the filtered and unfiltered results, it is known that such filtering does not affect the large-scale features of the circulation and that the two streamfunction fields (up to the moment of instability in the unfiltered calculation) are virtually identical (Figure 7).

Lastly, it is important to note that the RMS error quantities for the nonlinear box mode problems are nearly independent of ν and η . If there is nothing idiosyncratic about these problems, then we must conclude that the largest contribution to the RMS error fields comes from the uncertainty in the exact analytic solution to the nonlinear box mode problem.

4.5 Intercomparison

Results from the linear box mode tests (see Table I) demonstrate that the finite-element (with $N = 33$) and pseudospectral (with $N = 17$) models are comparably accurate over the range of ν and η studied. (The spectral model is, however, somewhat more efficient--Table II.) And, even though the finite-difference is by far the least accurate model, a phase error analysis of the FD model results shows that errors can be minimized for optimal choices of ν and η . Since these optimal parameters are functions of the time and space scales of the problem, however, this property will be of questionable value in more general problems characterized by multiple time and space scales. Even if a degree of compensation could be guaranteed in a specific problem, errors get smaller only if ν and η are increased in the same ratio. A fourfold decrease in the RMS errors would therefore require η and ν to be simultaneously increased by a factor of two, with a resulting increase in computational work of a factor of eight. In contrast, the spectral model (and to a lesser extent the FE model) generally require only η to be increased--say by two, for a four-fold reduction in error--because of their much greater spatial accuracy.

In the case of the nonlinear box modes, interpretation of the results is complicated by the fact that we have only a perturbation solution with which to compare the computational results. Consequently, our error measures--such as $\text{RMS}(\psi')$, etc.--reflect three sources of error: spatial and temporal truncation errors, and the error associated with not knowing the exact analytic solution. The RMS quantities listed in Table I for the nonlinear box mode tests cannot be used as direct measures of model performance.

The essential qualitative distinction that can be made between the results of the three models for $\epsilon > 0$ is that the finite-difference model, though presumably less accurate, appears not to be susceptible to catastrophic numerical instability when small-scale error fields are present. Under these conditions, the FD spatial truncation error is, however, formally quite large. A nonlinear FD solution will therefore become invalid after only a short period of time even though a stable calculation can be maintained for a much longer time.

5. FORCED NONLINEAR BOX MODE TESTS

5.1 Formulation

One means of avoiding the complications associated with having only a perturbation solution to the nonlinear box mode problem is to consider the analogous forced problem, that is to seek solutions to the inhomogeneous equation

$$\frac{\partial}{\partial t} \nabla^2 \psi + J(\psi, \nabla^2 \psi) + \psi_x = F(x, y, t) \quad (34)$$

where F is some suitably chosen forcing function. As before, ψ is required to vanish on Σ . In particular, we wish to examine solutions with spatial and temporal characteristics similar to those of the linear box modes. Accordingly, set

$$\psi(x, y, t) = \sin x \sin y \cos(ax + by + ct) \quad 0 \leq x, y \leq \pi \quad (35)$$

where a , b , and c are arbitrary constants which determine the wavelength, period and phase speed of the forced mode ($2\pi/(a^2 + b^2)^{1/2}$, $2\pi/c$, and $c/(a^2 + b^2)^{1/2}$, respectively). This will be a solution to (34) so long as

$$F(x, y, t) = \left\{ \frac{\partial}{\partial t} \nabla^2 + J(\psi, \epsilon \nabla^2) + \frac{\partial}{\partial x} \right\} \psi(x, y, t) \quad (36)$$

which will in general be nonvanishing, as will $J(\psi, \epsilon \nabla^2 \psi)$. Given specific values of parameters a , b , c and ϵ , the functional form of F can therefore be directly calculated. For the following tests, the Rossby number has been fixed at $\epsilon = 0.2$. An examination of higher ϵ behavior is reserved for the open boundary calculations of Section 7.

5.2 Finite-difference model results (Table I, cases 10-12; Figures 8-10)

Table I shows the RMS error measures for the finite-difference model after two periods for a variety of values of ν and η . The results indicate that the FD error norms are in general somewhat smaller than those for the linear box mode problems with comparable nondimensional

parameters. Compare Figures (3a, b) and (10a, b), for instance. In addition, a partial compensation between spatial and temporal errors once again exists so that the RMS errors (as in the linear box mode cases) need not decrease with increasing η and ν (Table I, cases 11 and 12). As in the nonlinear box mode problems, perturbation vorticity tends to collect on the western boundary (Figure 9a). This appears to be a quite general property of all the simulations when $\epsilon > 0$, no matter what the orientation of the forced mode.

5.3 Finite-element model results (Table I, cases 10-12; Figures 8-10)

The FE model behaves similarly, yielding very accurate and stable solutions for a range of parameters (Table I, cases 10-12). For instance, with $(\nu, \eta, a, b) = (32, 128, 1/\sqrt{2}, 1/\sqrt{2})$ the RMS errors are 0 (1-2%) after two periods. As in the FD, and as we shall see, the spectral computations, the RMS errors given by the FE solution to the nonlinear forced box mode problem are typically no less, and very often several times smaller, than the errors noted for the linear unforced box mode tests with comparable resolution. Figures (3c, d) and (10c, d) give an example of this behavior. (Note, also that the character of the RMS error curves seems to be modified by the forcing such that $\text{RMS}(\zeta')$ is a quasilinear function of time over the range of parameters examined here.) The perturbation fields associated with the forced problems, although small in amplitude, are still characterized by small-scale, westward-trapped ζ' and large-scale ψ' patterns (Figure 9).

5.4 Pseudospectral model results (Table I, cases 10-12; Figures 8-10)

These calculations were all performed with very high spatial resolution ($\nu \geq 16$); consequently, insignificant spatial truncation error is expected. With a diagonally propagating mode ($a = b = 1/\sqrt{2}$) and $\eta = 128$, the RMS errors are in fact very small, being no more than 0.5 percent after 5 periods of integration. Reference to Table I and Figures 10e, f demonstrates, however, that not only are the RMS errors

no longer strictly proportional to η^{-2} --as they were in the unforced case with sufficient spatial resolution--but the error trends are not linear in time. Although $\text{RMS}(\zeta')$ increases monotonically, $\text{RMS}(\psi')$ seems to vary quasiperiodically with little superimposed trend (Figures 10e, f).

As in the FD and FE simulations, the PS results for the forced nonlinear box mode problems show a similar tendency for small-scale ζ' to accumulate at the western edge of the domain (Figure 9e). The rate of this error accumulation might plausibly be thought to increase dramatically with ϵ , as in the nonlinear box mode problems; however, this hypothesis was not tested.

None of these conclusions depend sensitively on the direction of propagation of the forced mode.

5.5 Intercomparison

All three models are capable of delivering an accurate and stable solution to the forced nonlinear box mode problem for the computational parameters considered here. In all cases, the observed RMS errors are less than or equal to those noted in the linear box mode cases (for comparable ν and η). It is quite likely that this reduction in numerical error, despite going to a problem with nontrivial nonlinearities, is in some sense associated with a "locking in" of the numerical solution to the applied forcing. The quasioscillatory nature of the resultant $\text{RMS}(\psi')$ error curves--see especially Figure 10f--argues for such a process. We will return to this possibility in our discussion of future work.

6. NORTH WALL FORCED MODE TESTS

6.1 Formulation

Consider solving Eq. (3) with $\epsilon = 0$ in a domain characterized by three closed boundaries (on the east, south and west), but which is open on its northern edge. If, in particular, we let the boundary conditions on Σ be

$$\psi = \begin{cases} 0 & x = 0, x_B; \quad y = 0 \\ \sin \gamma \sin\left(\frac{m\pi x}{x_B}\right) \cos(x + t/2) & y = y_B \end{cases} \quad (37)$$

then the solution is

$$\psi(x, y, t) = \sin\left(\frac{m\pi x}{x_B}\right) \sin\left(\frac{\gamma y}{y_B}\right) \cos(x + t/2) \quad (38)$$

provided that $x_B = y_B = (m^2 \pi^2 + \gamma^2)^{1/2}$. A special case of these north wall forced modes are the linear box modes, Eq. (28), which result when $\gamma = n\pi$, n an integer, so that the streamfunction vanishes on all four walls.

Under appropriate forcing conditions, trapped solutions also exist to the north wall forced problem. One simple solution is

$$\psi(x, y, t) = \sin\left(\frac{m\pi x}{x_B}\right) \sinh\left(\frac{\gamma y}{y_B}\right) \cos(x + t/2) \quad (39)$$

where

$$x_B = y_B = (m^2 \pi^2 - \gamma^2)^{1/2}.$$

The appropriate boundary conditions for this problem are clearly the value of ψ evaluated along the boundary Σ . Since these solutions decay away from the north wall, (39) is referred to as a trapped case, and (38) as a propagating case. Note that for propagation (trapping) $x_B > m\pi$ ($x_B < m\pi$). A more general description of the north wall forcing problem and its relation to meander-induced forcing has been given by Harrison [31].

Two particular north wall forcing problems have been considered, one each of the propagating and trapped varieties. The former, which we will refer to as case 1, corresponds to Eq. (38) with $m = 1$ and $\gamma = 9.36$. The latter experiment, or case 2, is the trapped solution (39) with $m = 2$ and $\gamma = 4.0$.

In addition to these linear solutions, the corresponding nonlinear case 1 solution--that is, the solution to Eqs. (3) and (37) with $m = 1$, $\gamma = 9.36$ and $\epsilon > 0$ --has been sought. With $\epsilon = 0$, problems 1 and 2 are similar in practice to the linear box mode problems, except that ψ assumes some time-dependent distribution of values along the northern boundary. With nonlinearity present, however, a set of vorticity boundary conditions must also be specified along $y = y_B$. In the FE and PS models, vorticity is given its analytic value on boundary points characterized by inflow. In addition to this, the FD model constrains the values of vorticity on outflow by the Sundstrom/Davies condition--see Section 3.1. For the purposes of this study, solid boundaries will be treated as points of outflow. Since an exact solution to the resulting nonlinear problem is not available, we use (38) as our reference solution even when $\epsilon > 0$. This leads to a problem in interpreting the RMS error quantities similar to that encountered in the nonlinear box mode tests where only a perturbation solution was available.

6.2 Finite-difference model results (Table I, cases 13-21; Figures 11-19)

Not only are the methods of solution nearly identical, as noted above, but the results of the cases 1 and 2 linear north wall forced mode problems are themselves quite similar to those of the linear box mode tests (Section 4). The following ν and η dependencies were noted in the propagating and trapped cases, respectively.

6.2.1 Case 1 (propagating)

The case 1 north wall forced mode closely resembles the linear box mode with $m = n = 3$. The results for these two FD test problems are comparable with few exceptions. The error fields are once again

attributable to a simple phase difference between the discrete and analytic solutions (Figure 11a, b). $\text{RMS}(\psi')$ and $\text{RMS}(\zeta')$ grow linearly in time over the five period integrations (Figure 13a, b). Because of the highly structured nature of these solutions and the second-order spatial accuracy of the model, the RMS FD errors tend to be quite large in both although their variations with ν and η (Table I) suggest that it is possible to reduce the RMS error measures for suitable choices of the computational parameters. One striking dissimilarity between the box mode and north wall forced mode results is that, of the three error measures tabulated, only the normalized error in integrated energy is greatest for the north wall problem. This presumably reflects the modified nature of the north wall forced problem in which energy is exchanged between the interior solution and exterior environment at a rate determined by the imposed values of ψ_Σ and ζ_Σ . The change in energy level over the course of the 5 period simulation is, however, always fractionally quite small, being no more than 0 (10%) even for the poorest resolved experiment.

6.2.2 Case 2 (trapped)

Although the trapping scale γ^{-1} in equation (39) can be quite small, it has been chosen in case 2 to give only moderate structure to the solution. Consequently, the case 2 solution is actually somewhat less structured than the propagating case and, as such, the trapped FD results are more accurate by roughly a factor of four (Table I, cases 14 and 17, for instance). The curves of $\text{RMS}(\zeta')$ tend to rise to an initial moderate value, but grow much more slowly thereafter (Figure 16a)--a pattern noted over varying ranges of the parameters in the PS and FE linear box mode experiments. ($\text{RMS}(\psi')$ tends to remain quasilinear in time though it also has large excursions about the linear trend.) For the case 2 simulations, the perturbation streamfunction and vorticity fields can no longer be explained by a simple phase difference between computed and analytic fields. Instead, perturbation vorticity tends to accumulate in the northeast and northwest corners of the domain (Figure 15a).

For $\epsilon = 0.2$, the character of the FD solution is changed dramatically. Early in the simulation, the fields of perturbation streamfunction

and vorticity are characterized by a 6×2 celled structure. In fact, this feature appears in the FE and PS simulations as well (Figure 18). Since in this problem our reference solution is the linear forced mode (38), this structured perturbation vorticity field must partially reflect the nonlinear correction to (38) for $\epsilon = 0.2$. At later stages in the simulation, the perturbation vorticity generated during the calculation winds up on the western boundary where it forms six narrow cells of vorticity adjacent to the walls (Figure 19). For the FD model, these layers of vorticity dominate the field of total vorticity by the end of two periods of integration. Although this graininess in the FD results does not typically lead to numerical instability, such ζ fields are not accurately resolvable on the FD grid. For $\epsilon = 0.4$, this state of an unresolvable vorticity field is reached after one period.

As in the nonlinear box mode problem, the RMS errors are not calculated with respect to the exact analytic solution.

6.3 Finite-element model results (Table I, cases 13-21; Figures 11-19)

As noted for the FD model, the qualitative characteristics of the case 1 and case 2 FE computational results are very different, particularly in the form of the ψ' and ζ' fields (Figures 12c, d and 15c, d) and the associated RMS error curves (Figures 13c, d and 16c, d).

6.3.1 Case 1 (propagating)

As expected from their structural similarity, the 3×3 linear box mode and case 1 north wall forced mode problems both give RMS errors of 0 (5%) after five periods for $(\nu, \eta) = (0(10), 64)$ --see Table I, cases 5 and 14. (This is to be compared with errors of 30% and greater for the comparable FD problems.) The perturbation fields are themselves box mode-like, indicating a simple phase error relationship between computed and analytic solutions. Depending on ν and η , the $\text{RMS}(\zeta')$ error curves may have either of the two forms noted in the linear box mode calculations. For the pivotal resolution $(\nu, \eta) = 32/3, 64$, both $\text{RMS}(\psi')$ and $\text{RMS}(\zeta')$ increase quasilinearly (Figure 13c, d).

While $\text{RMS}(\zeta')$ decreases with increasing ν and η , $\text{RMS}(\psi')$ does not, perhaps indicating some degree of compensation between the contributions to ψ of spatial and temporal errors.

6.3.2 Case 2 (trapped)

For case 2, the fields of perturbation streamfunction and vorticity are not simply related to the analytic form of the trapped modes. While ψ' is dominated by lateral scales larger than those making up the trapped modes, ζ' appears at highest wave numbers and is eventually trapped in layers on both the eastern and western walls (Figure 15c, d). The RMS errors increase only slowly with time (Figure 16c, d) and decrease uniformly with increasing ν and η around the point of pivotal resolution (Table I). Typical error after five periods are 0 (2-3%) for $\text{RMS}(\psi')$ and $\text{RMS}(\zeta')$ at $(\nu, \eta) = (64/3, 64)$.

Stable, but noisy, solutions can be obtained out to five periods for the case 1 problem with $\epsilon = 0.2$. The final fields for the pivotal case-- $(\nu, \eta) = (32/3, 64)$ --are given in Figures 17c, d and 19c, d. Note the preferential accumulation of grid-point scale vorticity in the western-most basin whose contribution to the total field ζ is evident as early as $t = 2$ periods. Although gridpoint variations in the west undoubtedly contribute to sizeable numerical discretization errors in this region, it must be added that the resulting total streamfunction field ψ appears to be only locally affected, retaining over most of the basin the expected mode-like form. At $\epsilon = 0.4$, the small-scale vorticity accumulates much more catastrophically, leading to numerical instabilities for $t \leq 5$ periods (Table I, case 21).

6.4 Pseudospectral model results (Table I, cases 13-21; Figures 11-20)

The results of the Chebyshev spectral model are both qualitatively and quantitatively similar to those of the finite-element code. This is perhaps due to their higher order spatial accuracy.

6.4.1 Case 1 (propagating)

For the values of ν used in the case 1 tests, the spectral model has negligible spatial differencing error. The perturbation fields are therefore attributable to a phase error proportional to η^{-2} and not at all to ν (Figures 11e,f and 12e,f; Table I). For $(\nu, \eta) = (32/3, 64)$, the resulting errors are 0 (5%)--comparable to (much less than) the FE (FD) error norms. $\text{RMS}(\psi')$ and $\text{RMS}(\zeta')$ increase linearly in time (Figure 13e,f).

6.4.2 Case 2 (trapped)

Although ψ' and ζ' are no longer characterized by a simple phase relationship to ψ_a and ζ_a , but by basin-scale and grid-scale features, respectively (Figures 15e,f), their RMS values at $t = 5$ periods are again approximately proportional to η^{-2} (Table I, cases 17 and 18). For a pivotal resolution of $(\nu, \eta) = (64/3, 64)$, $\text{RMS}(\psi') \approx \text{RMS}(\zeta') = 0$ (1%). After an initial period of rapid error growth, the RMS norms are oscillatory in time with a much slower linear trend.

When we set $\epsilon = 0.2$ and seek nonlinear solutions to the case 1 north wall forced mode problem, the spectral model goes unstable as early as $t = 2$ periods. This behavior coincides with that of the FE model, but at slightly higher ϵ . The origin of this instability is the ultrathin western boundary layer of vorticity which develops in all the models by this time as a result of accumulated computational error (Figure 19e). The Chebyshev spectral model is especially sensitive to such a feature of the solution because of its nonuniform distribution of resolution which favors the domain edges over the interior. For reasonably narrow layers, the Chebyshev model will give a much more accurate representation than either the FD or FE models. However, the accuracy of the spectral model works to its own disadvantage for layers which are much thinner than the collocation grid spacing. This relationship between the accuracy and stability of FD and PS approximation has also been noted in integrations of one-dimensional viscous transport problems [15].

The most straightforward way to avoid eventual computational instability is to suppress the generation of perturbation vorticity and its

accumulation on the western boundary. This could be done by greatly increasing the spatial and temporal resolution of the spectral model. This, however, is inefficient. Quite good results have been attained by periodic filtering of the vorticity field to preferentially remove numerically generated vorticity errors which, it is assumed, are of much smaller scale than the solution we seek. Such an exponentially tapered spectral filter--see Section 4.4--has been applied to the pivotal non-linear north wall forced experiment-- $(\nu, \eta, \epsilon) = (32/3, 64, 0.2)$ --with the results shown in Figure 20. After 1.5 periods, the streamfunction field (which reflects the large-scale component of the flow) of both the unfiltered and filtered simulations are virtually identical. On the small scales, localized layers of ζ' exist; however, they are of much smaller amplitude and not as thin in the filtered calculation. Subsequently, the unfiltered run goes unstable at $t \approx 2$ periods. With the filter, the calculation proceeds to $t = 5$ periods with a resulting field which is at least as smooth as the FD and FE simulations (Figure 17). One potentially undesirable side-effect of the vorticity filter is that a much greater fraction of the initial energy has been lost over the course of the integration (Table I, case 19). A more scale-selective filter might avoid this problem.

6.5 Intercomparison

The intercomparative statements that can be made on the basis of the linear north wall forcing problems do not differ substantially from those made in connection with the linear box modes--Section 4.5. In general, both the FE and PS models, by virtue of their superior spatial accuracy, are notably more accurate than the FD model. The latter, however, can have small overall discretization error when values of ν and η are chosen to insure partial compensation between spatial and temporal errors. Errors in the PS simulations are strictly proportional to Δt^2 . This is also approximately true for the FE code in which, however, there is also a somewhat complicated parametric dependence on the form of the RMS error growth curves. For case 1 (box mode-like solution), ψ' and ζ' themselves resemble the analytic result for all

three models. In case 2, ψ' and ζ' collect at low and high wavenumbers respectively, independent of numerical technique.

When $\epsilon > 0$, the stability of the various models seems to be inversely related to the formal accuracy of the numerical technique involved. While the FD formalism is stable for all the tests we have conducted, the FE model develops instabilities for some values of the parameter set (ν, η, ϵ) . The spectral result becomes unbounded much earlier than the FE calculation, but can be stabilized for integrations of moderate length by spectrally filtering the vorticity field to delay the accumulation of vorticity at unresolvable scales.

7. LINEAR AND NONLINEAR ROSSBY WAVE TESTS

7.1 Formulation

The advected Rossby wave

$$\psi(x, y, t) = -\gamma y + \sin(kx + \ell y + \omega t) \quad (40)$$

where

$$\omega = k(1 - \epsilon\gamma) \quad (41)$$

and

$$k^2 + \ell^2 = 1$$

is a solution to both the linear and nonlinear vorticity equation (3). As for the box modes, we have scaled with respect to $d = (2\pi)^{-1}$ times the wavelength of the travelling wave; u_0 , a characteristic particle velocity; and the time scale $(\beta d)^{-1}$. In the resulting nondimensional system, the wavelength is 2π , and the basin size $x_B = \pi\Delta$ where Δ is the number of half wavelengths per box width (a measure of the structure of the solution). Theoretically it is known that Rossby waves are individually unstable to small perturbations [32] with an e-folding time proportional to $(\epsilon)^{-1}$. This growth time scale is comparable in all cases to the entire duration of the experiment. Due to the absence of large-amplitude perturbations (or "noise") that can efficiently extract energy from the primary wave, it is unlikely that purely physical instabilities--as opposed to computational ones--play a role in the following results. The reader should note that the nonlinearity of these model problems is trivial (that is, self-cancelling) when $\gamma = 0$.

7.2 Finite-difference model results (Table I, cases 22-37; Figures 21-23, 25-27)

The results for one linear Rossby wave experiment in which $(\nu, \eta, \epsilon) = (32/3.5, 128, 0)$ are listed in Table I, case 22. Variations in the RMS error measures as a function of ν and η did not differ from the comparable dependencies noted for the linear box mode and linear north wall forced modes--see Sections 4.5 and 6.5--and hence will not be

reiterated here. The one substantive difference between these and the other linear problems is that $\text{RMS}(\psi')$ and $\text{RMS}(\zeta')$ are not strictly linear in time but appear to be levelling off at $t = 5$ periods.

With no mean flow and moderate nonlinearity $(\epsilon, k, \ell, \gamma) = (0.4, 3/\sqrt{13}, 2/\sqrt{13}, 0)$, the RMS errors of the FD simulations are characterized by very small temporal, relative to spatial, errors. At the pivotal resolution $(\nu, \eta) = (32/3.5, 64)$, $\text{RMS}(\psi') \approx \text{RMS}(\zeta') \approx \text{NDIF}(\text{NRG}) = 0$ (14%) after five periods. The manifestation of error in these simulations are perturbation fields closely resembling box modes which begin to destroy the plane wave nature of the solution after a few periods (Figures 21a, b and 22a, b). This form for the error fields appears to be independent of ν and η . Their amplitude, as stated previously, depends sensitively on ν but not on η for those values considered here. (In addition, other simulations--cases 28, 29 and 31--show that $\text{RMS}(\psi')$ and $\text{RMS}(\zeta')$ also depend on the orientation of the reference wave so that cancellation of time and space errors can sometimes occur.) The RMS error measures typically grow quasilinearly, though in some cases there is a tendency for the rate of error growth to slow towards the end of the simulation. Lastly, the change in the integrated kinetic energy of the system is 0 (-10%), somewhat larger than that observed in either the nonlinear box mode or nonlinear north wall forced mode problems for comparable ν and η .

For $\epsilon = 0.8$, but still with $(\nu, \eta, k, \ell, \gamma) = (32/3.5, 64, 3/\sqrt{13}, 2/\sqrt{13}, 0)$, the same qualitative remarks apply. The field of ζ' does, however, begin to show some noticeable grid-scale variability in comparison to its rather smooth mode-like appearance for $\epsilon = 0.4$. The associated values of $\text{RMS}(\psi')$ and $\text{RMS}(\zeta')$ are comparable to those for $\epsilon = 0.4$.

With the addition of a mean flow ($\gamma \neq 0$), the FD model actually becomes more accurate perhaps reflecting the increased smoothness of the ψ field (Figure 25b). With $\gamma = 0.5$, the FD model delivers a stable solution with an accuracy of 0 (20%) after 5 periods (Table I, case 26). For a mean flow of the opposite sense ($\gamma = -0.5$), the errors are comparable or slightly larger. As with $\gamma = 0$, the integrated errors grow linearly in time, and the fields of ψ' and ζ' are dominated by large-scale box mode-like features. Similar remarks hold for Rossby waves of different orientation.

7.3 Finite-element model results (Table I, cases 22-37; Figures 21-23, 25-27)

The results of the FE linear Rossby wave calculations are as expected from Sections 4.3 and 6.3. With $(\nu, \eta, k, \ell, \gamma) = (32/3.5, 128, 3/\sqrt{13}, 2/\sqrt{13}, 0)$, $\text{RMS}(\psi') < \text{RMS}(\zeta') \leq 0(1\%)$ at the end of five periods of integration (Table I, case 22). In fact, $\text{RMS}(\zeta')$ has nearly stopped increasing altogether, though $\text{RMS}(\psi')$ continues to rise quasilinearly. Associated with these error levels are fields of ψ' and ζ' composed of basin-scale and grid-scale features, respectively.

With $\epsilon > 0$, the FE model accumulates box mode-like features in the streamfunction field. Errors in the vorticity are resident at somewhat smaller scales. Consider, for instance, Figures 21c, d and 22c, d which show the total and perturbation fields respectively at the end of a five-period integration with $(\nu, \eta, \epsilon, k, \ell, \gamma) = (32/3.5, 64, 0.4, 3/\sqrt{13}, 2/\sqrt{13}, 0)$. For this case, the FE model has errors of 0(9%), a significant improvement over the second-order FD results which, as remarked, have a large component of spatial truncation error. On the contrary, the FE errors are most sensitive to changes in η , at least in the parametric neighborhood of our pivotal calculation (Table I, cases 23-25).

Quantitatively similar statements can be made for simulations at higher Rossby number--case 28, $\epsilon = 0.8$ --and in the presence of mean advection--cases 26 and 27, $\gamma = \pm 0.5$. (Note that the latter differ from the nonadvected Rossby waves in that they have nontrivial nonlinearities.) As with the FD model, neither the increase in ϵ nor the inclusion of mean advection seriously increases the RMS errors of the FE model. As a result, for constant ν and η (spatial and temporal resolution), $\text{RMS}(\psi') = 0(1-4\%)$ and $\text{RMS}(\zeta') = 0(3-10\%)$ after 5 periods (Table I, cases 25-28). The error growth is quite consistently nearly linear (Figures 27c, d) with the perturbation streamfunction appearing at the largest (basin) scales although in a somewhat less organized pattern than the box mode-like features noted with $(\epsilon, \gamma) = (0.4, 0)$ --Figures 22d and 26d.

7.4 Pseudospectral model results (Table I, cases 22-37; Figures 21-27)

For $0.4 \leq \epsilon \leq 0.8$, the spectral model suffers eventual numerical instability at some $t \leq 5$ periods. Figure 24a shows a typical example where $(\nu, \eta, \epsilon, \gamma) = (16/3.5, 128, 0.4, 0)$. By $t = 1.5$ periods, the total vorticity is dominated by small-scale noise; catastrophic failure of the numerical experiment occurs shortly thereafter. The most intense grid-scale vorticity features occur at one or more points on the boundary, but the noise is also substantial in the interior along a line normal to that point. This is undoubtedly due to the nature of the spectral expansion which ties points together in just such a manner. The ultimate origin of the PS instability is not known. The site of the instability, for instance, is random and not simply related to the imposed patterns of inflow/outflow along the domain margins.

It has been discovered empirically, however, that periodic spectral filtering effectively controls the generation and accumulation of grid-scale vorticity, and prevents numerical instability in these nonlinear Rossby wave experiments. Figure 24 shows the effect on one such pivotal calculation. By $t = 1.5$ periods, ζ is entirely dominated by two regions of high wavenumber noise in the unfiltered calculation. When the simulation is redone, however, with filtering, the Rossby wave is easily advanced in time to $t = 5$ periods. The final field is quite free of grid-scale noise.

Filtering of this kind stabilizes a wide range of nonlinear Rossby wave calculations (Table I, cases 23-37). The resulting RMS errors are also notably small, being no more than a few percent for the experiments recorded in Table I. The errors associated with the filtered PS model are typically many times smaller than those of the comparable FD test and somewhat smaller than those given by the FE model. $\text{RMS}(\psi')$ and $\text{RMS}(\zeta')$ grow linearly in time (perhaps with some initially large value of the errors due to the filtering (Figures 23 and 27) with very little accumulation of unresolvable features in the vorticity field (Figures 21e, f and 25e, f). The removal of these small-scale features by filtering does not, however, seem to have a strong effect on the energy of the system.

7.5 Intercomparison

The parametric results of the linear Rossby wave calculations confirm the conclusions of Sections 4.5 and 6.5 in which it was noted that the FE and PS models were in general more accurate than the FD code, except for certain optimal choices of the computational parameters ν and η . In addition, the orientation of the Rossby wave has a strong influence on the RMS errors of the FD model. All three models are stable for $\epsilon = 0$.

When nonlinearity is admitted, however, the finite-difference and finite-element models are alone capable of delivering stable and accurate calculations of moderate duration ($t \leq 5$ periods) over a broad range of parameters. The spectral model is typically unstable in these instances unless it is supplemented by periodic spectral filtering of the vorticity field.

As a preliminary test of the response of the finite-difference and finite-element models to the addition of a scale selective vorticity filtering mechanism, we have redone the FD and FE experiments 25, 26 and 28 and the FE experiments 7 and 21 with the application at each time step of a 16th-order Shapiro filter [33]. The results of these comparisons indicate that the RMS errors of the FE calculations are generally lowered somewhat by the addition of filtering (particularly $\text{RMS}(\zeta')$ whose smaller scale components are being eliminated by the filtering) and its instabilities delayed (but not removed). The opposite, namely an increase of error with the application of filtering, is often true of the FD simulations. It is not obvious why this should be the case unless the computational boundary condition used in the FD formulation interacts in some systematic way with the applied filtering. This possibility will be explored in our next series of pseudoforecasting tests (see Section 8).

It is of interest to note, however, that all three models (perhaps with some distribution of wavenumber selective filtering) can be made to yield accurate solutions to these open domain problems. In fact, the models have error accumulation characteristics not greatly different than those noted in closed-basin problems. Specifically, the FE and PS models are many times more accurate for given ν and η than the FD model,

with the PS being overall the best. Even taking into account the increased efficiency of the finite-difference scheme (Table II), the difference between the second-order and higher-order methods is significant. It is estimated that the FE ($N = 33$) and PS ($N = 17$) models are, on the average, 15 and 3.5 times more accurate respectively than a FD model with $N \approx 43$ for which the running times of all three models would be approximately equal.

8. CONCLUSION

We have integrated the inviscid barotropic vorticity equation under a variety of assumed initial and boundary conditions corresponding to linear and nonlinear box modes, forced nonlinear box modes, north wall forced modes (meander induced forcing), and linear and nonlinear Rossby waves. The former two classes of problems are defined with closed domains; the latter two are partially or totally open with respect to a presupposed external environment and therefore represent prototype limited-area calculations for the ocean. Each problem has been solved using second-order finite-difference, fourth-order finite-element and infinite-order spectral approximation techniques. For each of the three models a series of calculations was performed to determine its accuracy, stability and efficiency as a function of problem type and the associated physical and computational nondimensional parameters. The most important of these parameters are ϵ , the Rossby number, and ν and η , nondimensional measures of the spatial and temporal resolution of the numerical approximation. The accuracy of model results was determined, wherever possible by comparing to known analytic or reference solutions. RMS measures of the errors in the computed values of vorticity, $\text{RMS}(\zeta')$, and streamfunction, $\text{RMS}(\psi')$, and a measure of the gain or loss of globally integrated kinetic energy, NDIF (NRG), were tabulated. Integrations of moderate length (5-10 periods of the reference solution) were performed as an empirical measure of the functional dependence of model stability on the parameters. As a result of these calculations, we are able to make model-model intercomparative statements for a sequence of linear and nonlinear problems in open, as well as closed, domains. To our knowledge, such intercomparisons have not previously been made. A more lengthy summary of the parameters and error norms can be found in Section 2. A complete discussion of results has been given in Sections 4-7 and Table I.

These tests have shown that all three models are capable of delivering efficient long-term solutions of acceptable accuracy to linear and weakly nonlinear problems in both closed and open domains. The results also suggest that given a judicious selection of frictional (filtering) mechanism

and/or computational boundary condition, each of the models can be made comparably accurate for highly nonlinear calculations. (This hypothesis is being tested in a related series of experiments). We conclude, therefore, that any of the physical/numerical models investigated here--modified perhaps by additional dissipative or boundary condition assumptions--could be used for the intended scientific applications mentioned in Section 1.

Under the assumption of inviscid dynamics, the operational performance of the three models is most sensitively related to the Rossby number, ϵ . For $0 \leq \epsilon \leq 0.2$, all the models are stable in the long-term. Furthermore, unless an optional choice of ν and η , the non-dimensional space and time steps, is made, the spectral and finite-element models are the most accurate, and the finite-difference the least. That this ranking reflects the formal spatial accuracies of the models has been demonstrated by a simple phase error analysis for the linear box mode problems--Section 4.2. The net result of this increased accuracy is that, for a given admissible error, both the FE and PS models are many times more efficient than the FD model (Section 7.5). These conclusions are valid independent of problem class.

Although the PS (and to a lesser degree the FE) models are susceptible to eventual numerical instability characterized by the catastrophic accumulation of grid-scale vorticity features, it has been found that stability can often be maintained, and errors reduced, by a periodic filtering (smoothing) procedure. Consider for instance the nonlinear Rossby wave experiments in the presence of mean advection. The PS model develops numerical instabilities which appear as very high wavenumber noise in the vorticity field. (This generation of noise may be partially due to our choice of boundary conditions--see the following remarks.) But, by selectively filtering out this grid-scale vorticity at each time step, the spectral model can be made stable in the long-term sense while maintaining a very high accuracy (Table I, cases 23-37). The RMS error norms of the FE (but not the FD) model are also reduced with the application of a scale selective vorticity filter.

If we had sufficient spatial resolution (that is, scale separation between the energy-containing band and our cutoff wavenumber, K_0) and could devise the optimal filter, removing vorticity in this manner would correspond to destroying enstrophy as it reached K_0 , but to leaving energy unaffected. Such inertial range filters have been constructed on the basis of various turbulence theory closure schemes [34] and are typically nonlinear and highly dependent on the energy spectrum of the field being filtered. Standard frictional mechanisms such as linear and second-order vorticity dissipation, and the exponentially tapered vorticity filter adopted here for the spectral calculations are almost certainly crude approximations to these optimal filters. As we have seen, however, even relatively ad hoc removal of small-scale vorticity prolongs the useful length of integration and increases the accuracy of highly nonlinear simulations.

Were we to incorporate a higher order frictional mechanism into our models in order to prevent the contamination of our results by small-scale noise, however, the problem of specifying the outflow boundary condition would take on added importance. We already know on the basis of finite-difference calculations detailed in Section 4.2 that alternate specifications of ζ_Σ can lead to much smoother vorticity fields. Similar findings for the nonlinear Rossby waves (not presented here) also indicate that certain outflow boundary conditions are better able to control the accumulation of small-scale vorticity near the boundaries, presumably by allowing the grid-scale error field to propagate more freely through the boundaries. Although the optimal form of the outflow boundary condition is a matter of some debate, there are several strong candidates which have proven useful in various applications. These include the Sundstrom/Davies condition considered here [16, 17], the Orlanski radiation condition [11], and various extrapolatory techniques and multi-dimensional generalizations of the method of characteristics. Lastly, it is possible to locally modify the physics of the problem so that small-scale errors are trapped near the boundaries and selectively dissipated before they can contaminate the interior solution [35, 36].

A second series of tests is now being readied to investigate further the effects of dissipation (including filtering) and alternate specifications of the outflow boundary condition on the accuracy and stability of related

limited-area calculations. Following the methodology of this report, we plan a systematic parametric examination of these effects. Since it is expected that this testing phase serve as a lead-in to the intended scientific applications outlined in Section 1, the reference solution selected for these next tests will have a multiplicity of space and time scales. Two approaches are possible. First, a desired analytic solution can be constructed (perhaps assuming some known distribution of body forces). Second, the open ocean problem can be embedded into a previously existing closed-basin numerical calculation of known accuracy (which serves as the source of boundary information). Of these two approaches, the former is the easier to implement but, in general, would require the assumption of some complicated time-dependent forcing function. As has been speculated in Section 5, this may significantly reduce the computational error because the computed solution tends to be "locked in" to the forcing. Using a forced analytic reference solution as a test problem is, therefore, neither physically nor numerically analogous to the unforced forecasting/hindcasting studies proposed in Section 1. An embedding experiment, on the other hand, can be made physically as well as numerically identical to a forecasting study although it requires that boundary and verification data be generated numerically and stored for later access. For this reason, we will pursue the embedding strategy as a basis for our next series of tests.

The large-scale unforced numerical simulation into which the open ocean calculations will be embedded can be conducted in either a closed or periodic domain. Solutions will be sought whose local character resembles that of the proposed scientific applications; that is, either the evolution of a mesoscale eddy field such as might be observed in the mid-ocean or the local dynamics of intense current regions might be examined as natural precursors to the MODE/POLYMODE forecasting and EGCM jet instability studies, respectively. Since it is necessary to consider various frictional and filtering mechanisms (including the inviscid limit), reference numerical solutions are needed for each of these mechanisms although the environmental parameters could otherwise be held fixed. (Besides providing initial and boundary condition data for the open ocean models, this could provide an interesting study of the effects of

subgrid-scale parameterization on geophysical turbulence.) In addition, in order to avoid biasing the results towards a particular numerical technique, the large-scale reference solution must be generated either 1) with a numerical model different than those being compared, or 2) independently for each numerical model being tested.

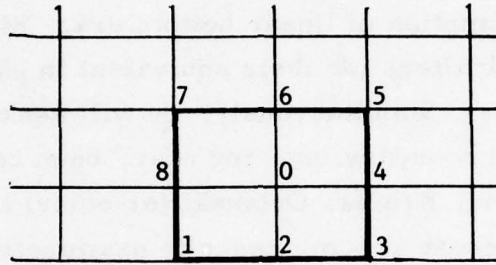
The pivotal calculation for each of these tests will be inviscid and use the Charney-Fjortoft-von Neumann closure. Subsequent calculations will involve the assumption of linear bottom drag, high-order lateral friction and spectral filters (or their equivalent in physical space) in various combinations. Simultaneously, we will seek to minimize wave reflection from, and boundary layering near, open boundaries by invoking the Sundstrom/Davies, Kreiss, Orlanski (or other) condition on outflow. It will also be of interest in some cases to examine the effects on the accuracy and stability of the models of adding errors of certain amplitude and scale to the imposed boundary data. This will be important in judging the suitability of the models for forecasting studies driven by observational data in which measurement and objective analysis errors may be large. On this basis, it will be possible to confidently select that physical problem/numerical technique/boundary condition set which is most reliable for limited-area calculations with $\epsilon \gg 0$.

At some point during this sequence of tests, it will become necessary to choose one of the open ocean models as that best suited for the intended scientific problems. This selection will be done expeditiously and will be based on such factors as the efficiency of the models for a given accuracy and the generalizability of the models (to account for baroclinic processes or alternate boundary conditions, for instance). Once the choice of numerical technique has been made, a baroclinic (two-level) version of barotropic model will be constructed and readied for use. Some limited testing, along the lines of this report, will be necessary to demonstrate that our conclusions based on these barotropic calculations do indeed carry over to the baroclinic problem.

APPENDIX I

Implementation of the Sundstrom/Davies Boundary Condition

Consider a region near the boundary with the following local ordering.



The vorticity equation applied at the point 0 will involve vorticity values on the other eight numbered points.

$$\zeta_0^{k+1} - \zeta_0^{k-1} = -\frac{\Delta t}{\Delta x} (\psi_4^k - \psi_8^k) - Q \sum_{r=1}^8 J_r \zeta_r^k \quad (A1)$$

Where $Q = \epsilon \Delta t / h^2$ and J_r is the Arakawa Jacobian term for the r -th point evaluated at point 0.

The Sundstrom/Davies closure for the boundary point 2 is

$$\zeta_0^{k+1} + \zeta_0^{k-1} = \zeta_2^k + \zeta_6^k \quad (A2)$$

ζ_0^{k+1} can be eliminated from (A1) and (A2) and the result can be written:

$$QJ_1 \zeta_1^k + (1 + QJ_2) \zeta_2^k + QJ_3 \zeta_3^k = R_2 \quad (A3)$$

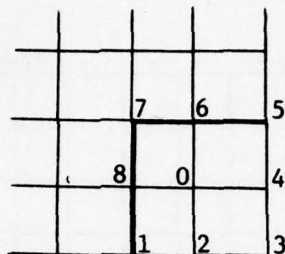
where

$$R_2 = 2\zeta_0^{k-1} - \zeta_6^k - \frac{\Delta t}{h} (\psi_4^k - \psi_8^k) - Q \sum_{r=4}^8 J_r \zeta_r^k \quad (A4)$$

In this numerical procedure, the interior vorticity and streamfunction are computed before the boundary vorticity. Equation (A3) is arranged so

that R_2 contains only known quantities. For each point along a boundary (but not at corners), (A3) applies.

Were it not for corner points, the system of equation (A3) would be of tridiagonal form and easily invertable. Consider a region near the (southeast) corner.



For the boundary condition at the corner, we take the spatial average along the diagonal.

$$\zeta_0^{k+1} + \zeta_0^{k-1} = \zeta_3^k + \zeta_7^k \quad (A5)$$

It would seem that near corners a pentadiagonal system is required since the Jacobian evaluated at 0 involves the five unknown boundary values at points one through five. However, the Sundstrom/Davies conditions at points two and four are

$$\zeta_0^{k+1} + \zeta_0^{k-1} = \zeta_2^k + \zeta_6^k \quad (A6)$$

and

$$\zeta_0^{k+1} + \zeta_0^{k-1} = \zeta_3^k + \zeta_7^k \quad (A7)$$

Thus,

$$\zeta_2^k = \zeta_3^k + \zeta_7^k - \zeta_6^k \quad (A8)$$

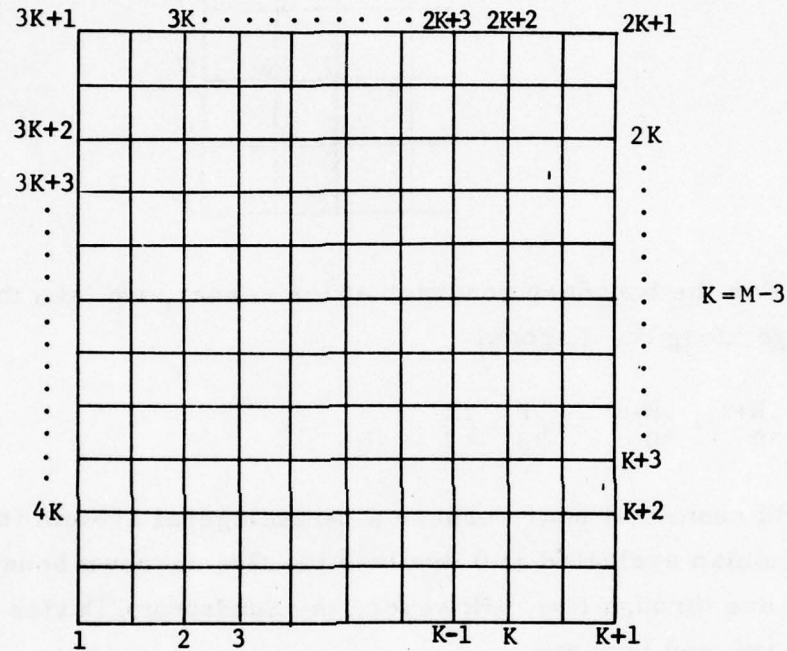
and

$$\zeta_4^k = \zeta_3^k + \zeta_7^k - \zeta_8^k \quad (A9)$$

This means that boundary points which are corner neighbors can be expressed in terms of the corner vorticity and known values. (A8) and

(A9) are applied in conjunction with the equations requiring vorticity values of the corner neighbor, i.e., the corner and the two boundary points $2h$ from the corner.

The unknowns in the tridiagonal system are given a cyclic ordering excluding the corner neighbor points.



In the diagram the ordering is started in the southwest corner, and (A3) is a tridiagonal system with cyclic boundary conditions since point 1 and $4K$ are connected. By a reordering of the points, the tridiagonal cyclic system can be transformed into a pentadiagonal system which requires twice the computation time of a tridiagonal system.

At inflow points, the vorticity is known and (A3) is replaced by

$$\zeta_2^k = \zeta_B^k \quad (A10)$$

where ζ_B^k is the specified value. If the origin of the ordering (the southwest corner in the diagram) were inflow, the off-tridiagonal terms expressing the cyclic nature vanish and we are left with a simple

tridiagonal system. If the southwest corner is not inflow, renumber the boundary point

$$i' = (i + L - 1) \bmod(4K) + 1$$

where L is an inflow point. Finally, the values at the eight corner neighbor points are obtained from (A8) and (A9), or specified if inflow.

REFERENCES

- [1] MODE Group (1977). The mid-ocean dynamics experiment. Submitted for publication.
- [2] Legeckis, R. (1975). Application of synchronous meteorological satellite data to the study of time dependent sea surface temperature changes along the boundary of the Gulf Stream. Geo. Res. Letters, 2, 435-438.
- [3] Robinson, A. R. (1977). Mesoscale eddies. Proceedings of the JOC/SCOR Joint Study Conference on General Circulation Models of the Ocean and their Relation to Climate (Helsinki, May, 1977). To appear.
- [4] Holland, W. R. (1978). The role of mesoscale eddies in the general circulation of the ocean: numerical experiments using a quasigeostrophic model. In press.
- [5] Robinson, A. R., D. E. Harrison, Y. Mintz and A. J. Semtner (1977). Eddies and the general circulation of an idealized oceanic gyre: A wind and thermally driven primitive equation numerical experiment. Journ. Phys. Ocean., 7, 182-207.
- [6] Semtner, A. J. and Y. Mintz (1977). Numerical simulation of the Gulf Stream and mid-ocean eddies. Journ. Phys. Ocean., 7, 208-230.
- [7] Haidvogel, D. B. and W. R. Holland (1978). The stability of ocean currents in eddy-resolving general circulation models. In press.
- [8] Harrison, D. E. and A. R. Robinson (1978). Energy analysis of open regions of turbulent flows; mean eddy energetics of a numerical ocean circulation experiment. In press.
- [9] Owens, W. B. and F. P. Bretherton (1978). A numerical study of mid-ocean mesoscale eddies. In press.
- [10] Rhines, P. B. (1977). The dynamics of unsteady currents. The Sea, Volume 6: Marine Modeling, ed. by E. D. Goldberg, I. N. McCane, J. J. O'Brien, and J. H. Steele, John Wiley and Sons, New York.
- [11] Orlanski, I. (1976). A simple boundary condition for unbounded hyperbolic flows. Journ. Comp. Phys., 21, 251-269.
- [12] Kollmeyer, R. C. (1975). Labrador Current Predictive Model. Ph. D. Thesis, University of Connecticut.
- [13] Hurlburt, H. E. and J. D. Thompson (1973). Coastal upwelling on a betaplane. Journ. Phys. Ocean., 3, 16-32.

- [14] Fix, G.J. and M.D. Gunzberger (1976). Downstream boundary conditions for viscous flow problems. ICASE Report No. 76-10. Institute for Computer Applications in Science and Engineering, NASA Langley Research Center, Hampton, Virginia.
- [15] Haidvogel, D. B. (1978). Resolution of downstream boundary layers in the Chebyshev approximation to viscous flow problems. Submitted for publication.
- [16] Sundstrom, A. (1969). Stability theorems for the barotropic vorticity equation. Mon. Wea. Rev., 97, 340-345.
- [17] Davies, H. C. (1973). On the initial-boundary value problem of some geophysical fluid flows. Journ. Comp. Phys., 13, 398-422.
- [18] Charney, J. G., R. Fjortoft and J. von Neumann (1950). Numerical integration of the barotropic vorticity equation. Tellus, 2, 237-254.
- [19] Bennett, A. F. and P. E. Kloeden (1978). Boundary conditions for limited-area forecasts. Submitted for publication.
- [20] Shapiro, M. A. and J. J. O'Brien (1970). Boundary conditions for fine-mesh limited-area forecasts. Journ. App. Met., 9, 345-349.
- [21] Orszag, S. A. and M. Israeli (1974). Numerical simulation of viscous incompressible flows. Ann. Rev. Fluid Mech., 6, 281-318.
- [22] Fix, G. J. (1975). Finite element models for ocean circulation problems. SIAM Journ. App. Math., 29, 371-387.
- [23] Arakawa, A. (1966). Computational design for long-term numerical integration of the equations of motion: two-dimensional incompressible flow. Part I. Journ. Comp. Phys., 1, 119-143.
- [24] Jespersen, D. C. (1974). Arakawa's method is a finite-element method. Journ. Comp. Phys., 16, 383-390.
- [25] Pereyra, V. (1967). Accelerating the convergence of discretization algorithms. SIAM Journ. Num. Anal., 4, 508-533.
- [26] Haidvogel, D. B. (1977). Quasigeostrophic regional and general circulation modelling: an efficient pseudospectral approximation technique. Proceedings of the ASME Symposium on Computing Methods in Geophysical Mechanics. AMD-volume 25, The American Society of Mechanical Engineers.
- [27] Lanczos, C. (1956). Applied Analysis. Prentice Hall, Englewood Cliffs, N. J.
- [28] Haidvogel, D. B. and T. Zang (1978). The accurate solution of Poisson's equation by expansion in Chebyshev polynomials. Submitted for publication.

- [29] Orszag, S. A. (1972). Comparison of pseudospectral and spectral approximation. Stud. App. Math., 51, 253-259.
- [30] Pedlosky, J. (1967). Fluctuating winds and the ocean circulation. Tellus, 19, 250-256.
- [31] Harrison, D. E. (1977). On Mesoscale Mean-Field Interaction in the Ocean. Ph. D. Thesis, Harvard University, Cambridge, MA.
- [32] Gill, A. E. (1974). The stability of planetary waves on an infinite betaplane. Geophys. Fluid Dyn., 6, 29-47.
- [33] Shapiro, R. (1971). The use of linear filtering as a parameterization of atmospheric diffusion. Journ. Atm. Sci., 28, 523-531.
- [34] Kraichnan, R. H. (1976). Eddy viscosity in two and three dimensions. Journ. Atm. Sci., 33, 1521-1536.
- [35] Orszag, S. A. (1976). Turbulence and transition: a progress report. Proceedings of the Fifth International Conference on Numerical Methods in Fluid Dynamics, Springer-Verlag.
- [36] Perkey, D. J. and C. W. Kreitzberg (1976). A time-dependent lateral boundary scheme for limited-area primitive equation models. Mon. Wea. Rev., 104, 744-755.

TABLE CAPTIONS

Table I: Maximum RMS error measures-- $\text{RMS}(\psi')$, $\text{RMS}(\zeta')$, and NDIF (NRG)--for the finite-difference (FD), finite-element (FE) and pseudospectral (PS) models as a function of problem class, duration of experiment, and the associated nondimensional parameters. The first seven columns refer to the experiment number and the quantities ϵ , Δ , x_B , N , ν and η which are, respectively, the Rossby number, the number of half wavelengths of the reference solution within the domain, the nondimensional basin size, the number of spatial degrees of freedom in each direction and nondimensional measures of the spatial and temporal resolution. Intermediate columns are reserved for problem-dependent parameters which have been introduced in Sections 4-7.

Table II: Approximate model running times as a function of N (CPU time in seconds on the NCAR CDC 7600 per 100 time steps). The ratios of the running times (also listed) indicate that the computational time increases as approximately N^2 for the FD and FE models and as $N \ln N$ for the PS model. Running times for the other linear and nonlinear model problems are comparable to those quoted here for the Rossby wave calculations.

TABLE I

Linear and Nonlinear Box Modes

Exp't	ϵ	Δ	X_B	N	ν	η	m	n	Duration	RMS (ψ')	RMS (ζ')	NDIF (NRG)	Comments
1	0	$\sqrt{2}$	$\sqrt{2}\pi$	33	$16\sqrt{2}$	64	1	1	FD	10.8×10^{-2}	9.4×10^{-2}	8.1×10^{-4}	
									FE	6.0×10^{-2}	5.2×10^{-2}	2.1×10^{-4}	
				17	$8\sqrt{2}$				PS	6.2×10^{-2}	5.4×10^{-2}	1.9×10^{-4}	
2	0	$\sqrt{2}$	$\sqrt{2}\pi$	33	$16\sqrt{2}$	32	1	1	FD	7.8×10^{-2}	6.8×10^{-2}	6.6×10^{-4}	
									FE	$25. \times 10^{-2}$	$21. \times 10^{-2}$	$16. \times 10^{-4}$	
				17	$8\sqrt{2}$				PS	$25. \times 10^{-2}$	$22. \times 10^{-2}$	$16. \times 10^{-4}$	
3	0	$\sqrt{2}$	$\sqrt{2}\pi$	33	$16\sqrt{2}$	128	1	1	FD	$15. \times 10^{-2}$	$27. \times 10^{-2}$	$72. \times 10^{-5}$	
									FE	1.3×10^{-2}	2.3×10^{-2}	4.2×10^{-5}	
				17	$8\sqrt{2}$				PS	1.5×10^{-2}	1.4×10^{-2}	2.4×10^{-5}	
4	0	$2\sqrt{2}$	$2\sqrt{2}\pi$	33	$8\sqrt{2}$	64	2	2	FD	$51. \times 10^{-2}$	$46. \times 10^{-2}$	$24. \times 10^{-4}$	
									FE	4.2×10^{-2}	5.5×10^{-2}	7.7×10^{-4}	
				17	$4\sqrt{2}$				PS	5.3×10^{-2}	5.1×10^{-2}	4.0×10^{-4}	
5	0	$3\sqrt{2}$	$3\sqrt{2}\pi$	33	$16\sqrt{2}/3$	64	3	3	FD	$96. \times 10^{-2}$	$93. \times 10^{-2}$	5.2×10^{-3}	
									FE	2.5×10^{-2}	7.6×10^{-2}	3.0×10^{-3}	
				17	$8\sqrt{2}/3$				PS	3.3×10^{-2}	5.8×10^{-2}	3.7×10^{-3}	
6	0.2	$\sqrt{2}$	$\sqrt{2}\pi$	33	$16\sqrt{2}$	64	1	1	FD	$18. \times 10^{-2}$	$16. \times 10^{-2}$	$11. \times 10^{-3}$	Sundstrom
									FD	$18. \times 10^{-2}$	$16. \times 10^{-2}$	9.3×10^{-3}	Specify ζ_a
									FD	$18. \times 10^{-2}$	$16. \times 10^{-2}$	$11. \times 10^{-3}$	Kreiss
				17	$8\sqrt{2}$				FE	8.4×10^{-2}	$10. \times 10^{-2}$	3.0×10^{-3}	
				17	$8\sqrt{2}$				PS	$35. \times 10^{-2}$	$34. \times 10^{-2}$	2.4×10^{-3}	

Exp't	ε	Δ	X_B	N	ν	η	m	n	Duration	RMS(ψ')	RMS(ζ')	NDIF (NRG)	Comments
7	0.4	$\sqrt{2}$	$\sqrt{2}\pi$	33	$16\sqrt{2}$	64	1	1	FD	8.6×10^{-1}	8.3×10^{-1}	1.6×10^{-2}	
									FE	$12. \times 10^{-1}$	$18. \times 10^{-1}$	2.6×10^{-2}	unstable @ t=5.
									FE	$12. \times 10^{-1}$	$11. \times 10^{-1}$	2.6×10^{-3}	filter
									PS [2.5]				
									PS	$12. \times 10^{-1}$	$11. \times 10^{-1}$	1.2×10^{-2}	filter
8	0.2	$2\sqrt{2}$	$2\sqrt{2}\pi$	33	$8\sqrt{2}$	64	2	2	FD	$29. \times 10^{-2}$	$28. \times 10^{-2}$	$35. \times 10^{-2}$	
									FE	6.5×10^{-2}	$12. \times 10^{-2}$	2.3×10^{-3}	
									PS	$30. \times 10^{-2}$	$35. \times 10^{-2}$	-1.0×10^{-3}	
9	0.2	$\sqrt{2}$	$\sqrt{2}\pi$	33	$16\sqrt{2}$	128	1	1	FD	1.4×10^{-1}	1.2×10^{-1}	$10. \times 10^{-3}$	
									FE	2.8×10^{-1}	2.5×10^{-1}	4.5×10^{-3}	
									PS	3.1×10^{-1}	3.0×10^{-1}	2.4×10^{-3}	
				17	$8\sqrt{2}$								
Forced Nonlinear Box Modes													
	ε	Δ	X_B	N	ν	η	a	b	c				
10	0.2	1.0	π	17	16	64	$1/\sqrt{2}$	$1/\sqrt{2}$	$1/2$	FD	1.9×10^{-2}	5.2×10^{-2}	2.8×10^{-2}
										FE	1.1×10^{-2}	6.5×10^{-2}	1.2×10^{-2}
										PS	1.0×10^{-2}	1.6×10^{-2}	1.4×10^{-2}
11	0.2	1.0	π	33	32	64	$1/\sqrt{2}$	$1/\sqrt{2}$	$1/2$	FD	4.4×10^{-3}	1.4×10^{-2}	6.3×10^{-3}
										FE	9.0×10^{-3}	2.0×10^{-2}	$14. \times 10^{-3}$
										PS	$10. \times 10^{-3}$	1.5×10^{-2}	$14. \times 10^{-3}$
12	0.2	1.0	π	33	32	128	$1/\sqrt{2}$	$1/\sqrt{2}$	$1/2$	FD	9.6×10^{-3}	2.0×10^{-2}	-9.5×10^{-3}
										FE	2.6×10^{-3}	1.9×10^{-2}	2.9×10^{-3}
										PS	2.3×10^{-3}	0.4×10^{-2}	3.5×10^{-3}

Exp't ε Δ X_B N ν η case Duration RMS (ψ') RMS (ζ') NDIF (NRG) Comments

North Wall Forced Modes

13	0.0	3	9.87	17	16/3	64	1	FD	5	120. $\times 10^{-2}$	110. $\times 10^{-2}$	-140. $\times 10^{-3}$	
								FE	5	1.6 $\times 10^{-2}$	7.5 $\times 10^{-2}$	5.1 $\times 10^{-3}$	
								PS	5	5.0 $\times 10^{-2}$	5.1 $\times 10^{-2}$	10. $\times 10^{-3}$	
14	0.0	3	9.87	33	32/3	64	1	FD	5	30. $\times 10^{-2}$	30. $\times 10^{-2}$	-40. $\times 10^{-3}$	
								FE	5	4.7 $\times 10^{-2}$	5.1 $\times 10^{-2}$	9.4 $\times 10^{-3}$	
								PS	5	5.0 $\times 10^{-2}$	5.1 $\times 10^{-2}$	10. $\times 10^{-3}$	
15	0.0	3	9.87	33	32/3	128	1	FD	5	340. $\times 10^{-3}$	33. $\times 10^{-2}$	-46. $\times 10^{-3}$	
								FE	5	9.6 $\times 10^{-3}$	2.4 $\times 10^{-2}$	2.0 $\times 10^{-3}$	
				17	16/3			PS	5	13. $\times 10^{-3}$	1.3 $\times 10^{-2}$	2.5 $\times 10^{-3}$	
16	0.0	3/2	4.85	17	32/3	64	2	FD	5	33. $\times 10^{-2}$	23. $\times 10^{-2}$	-92. $\times 10^{-3}$	
								FE	5	1.9 $\times 10^{-2}$	9.8 $\times 10^{-2}$	- 2.9 $\times 10^{-3}$	
								PS	5	1.3 $\times 10^{-2}$.94 $\times 10^{-2}$	3.7 $\times 10^{-3}$	
17	0.0	3/2	4.85	33	64/3	64	2	FD	5	5.6 $\times 10^{-2}$	5.4 $\times 10^{-2}$	-20. $\times 10^{-3}$	
								FE	5	1.4 $\times 10^{-2}$	3.4 $\times 10^{-2}$	3.4 $\times 10^{-3}$	
								PS	5	9.3 $\times 10^{-3}$	1.3 $\times 10^{-2}$	3.8 $\times 10^{-3}$	
18	0.0	3/2	4.85	33	64/3	128	2	FD	5	68. $\times 10^{-3}$	60. $\times 10^{-3}$	-240. $\times 10^{-4}$	
								FE	5	3.8 $\times 10^{-3}$	33. $\times 10^{-3}$	7.0 $\times 10^{-4}$	
				17	32/3			PS	5	3.3 $\times 10^{-3}$	2.4 $\times 10^{-3}$	9.2 $\times 10^{-4}$	
19	0.2	3	9.87	33	32/3	64	1	FD	5	7.4 $\times 10^{-1}$	1.00	-11. $\times 10^{-2}$	
								FE	5	4.3 $\times 10^{-1}$	1.35	- 4.4 $\times 10^{-2}$	
								PS	[2.0]				
								PS	5	4.0 $\times 10^{-1}$	0.86	-57. $\times 10^{-2}$	filter

Exp't	ϵ	Δ	X_B	N	ν	η	case		Duration	RMS (ψ')	RMS (ζ')	NDIF (NRG)	Comment	
20	0.2	3	9.87	33	32/3	128	1		5	7.6×10^{-1}	1.00	$-11. \times 10^{-2}$		
									5	5.0×10^{-1}	1.30	-7.5×10^{-2}		
				17	16/3				[2.5]					
21	0.4	3	9.87	33	32/3	64	1		5	1.5	2.3	-1.8×10^{-1}		
									[2.5]					
									5	1.4	1.6	-2.6×10^{-1}	filter	
									[1.0]					
Linear and Nonlinear Rossby Waves														
	ϵ	Δ	X_B	N	ν	η	k	ℓ	γ					
22	0.0	3.5	3.5 π	33	32/3.5	128	$3/\sqrt{13}$	$2/\sqrt{13}$	0	5	$160. \times 10^{-3}$	$145. \times 10^{-3}$	$-150. \times 10^{-3}$	
										5	6.3×10^{-3}	$12. \times 10^{-3}$	6.0×10^{-3}	
				17	16/3.5					5	8.3×10^{-3}	8.2×10^{-3}	8.0×10^{-3}	
23	0.4	3.5	3.5 π	17	16/3.5	64	$3/\sqrt{13}$	$2/\sqrt{13}$	0	5	$58. \times 10^{-2}$	$52. \times 10^{-2}$	$-45. \times 10^{-2}$	
										5	6.2×10^{-2}	6.8×10^{-2}	6.2×10^{-2}	
									[4.5]					
									5	1.9×10^{-2}	1.9×10^{-2}	2.1×10^{-2}	filter	
24	0.4	3.5	3.5 π	33	32/35	64	$3/\sqrt{13}$	$2/\sqrt{13}$	0	5	$14. \times 10^{-2}$	$13. \times 10^{-2}$	$-14. \times 10^{-2}$	
										5	8.3×10^{-2}	9.2×10^{-2}	9.0×10^{-2}	
									[3.0]					
									5	2.0×10^{-2}	2.1×10^{-2}	2.1×10^{-2}	filter	
25	0.4	3.5	3.5 π	33	32/3.5	128	$3/\sqrt{13}$	$2/\sqrt{13}$	0	5	$16. \times 10^{-2}$	$15. \times 10^{-2}$	$-16. \times 10^{-2}$	
										5	$15. \times 10^{-2}$	$15. \times 10^{-2}$	$-15. \times 10^{-2}$	filter
										5	2.6×10^{-2}	4.2×10^{-2}	1.8×10^{-2}	
										5	1.7×10^{-2}	2.0×10^{-2}	1.9×10^{-2}	filter
				17	16/3.5					[4.5]				
				17	16/3.5					5	0.5×10^{-2}	0.5×10^{-2}	0.5×10^{-2}	filter

Exp't	ϵ	Δ	X_B	N	ν	η	k	ℓ	γ	Duration	RMS(ψ')	RMS(ζ')	NDIF (NRG)	Comments	
26	0.4	3.5	3.5 π	33	32/3.5	128	3/ $\sqrt{13}$	2/ $\sqrt{13}$	0.5	FD	5	27. $\times 10^{-3}$	20. $\times 10^{-2}$	-38. $\times 10^{-3}$	
										FD	5	33. $\times 10^{-3}$	44. $\times 10^{-2}$	12. $\times 10^{-3}$	filter
										FE	5	7.0 $\times 10^{-3}$	9.4 $\times 10^{-2}$	5.2 $\times 10^{-3}$	
										FE	5	5.6 $\times 10^{-3}$	6.0 $\times 10^{-2}$	6.2 $\times 10^{-3}$	filter
				17 16/3.5						PS	[4.0]	4.1 $\times 10^{-3}$	2.9 $\times 10^{-2}$	9.6 $\times 10^{-3}$	filter
				17 16/3.5						PS	5	410. $\times 10^{-4}$	190. $\times 10^{-3}$	-100. $\times 10^{-3}$	
27	0.4	3.5	3.5 π	33	32/3.5	128	3/ $\sqrt{13}$	2/ $\sqrt{13}$	-0.5	FD	5	46. $\times 10^{-4}$	34. $\times 10^{-3}$	13. $\times 10^{-3}$	
				17 16/3.5						FE	5	9.0 $\times 10^{-4}$	6.0 $\times 10^{-3}$	-1.0 $\times 10^{-3}$	filter
				17 16/3.5						PS	[4.0]				
										PS	5				
28	0.8	3.5	3.5 π	33	32/3.5	128	3/ $\sqrt{13}$	2/ $\sqrt{13}$	0	FD	5	160. $\times 10^{-3}$	17. $\times 10^{-2}$	-160. $\times 10^{-3}$	
										FD	5	150. $\times 10^{-3}$	16. $\times 10^{-2}$	-140. $\times 10^{-3}$	filter
										FE	5	42. $\times 10^{-3}$	5.4 $\times 10^{-2}$	27. $\times 10^{-3}$	
										FE	5	33. $\times 10^{-3}$	3.5 $\times 10^{-2}$	25. $\times 10^{-3}$	filter
				17 16/3.5						PS	[2.0]				
				17 16/3.5						PS	5	6.7 $\times 10^{-3}$	1.1 $\times 10^{-2}$	7.4 $\times 10^{-3}$	filter
29	0.4	3.5	3.5 π	33	32/3.5	128	1/ $\sqrt{2}$	1/ $\sqrt{2}$	0	FD	5	59. $\times 10^{-3}$	79. $\times 10^{-3}$	45. $\times 10^{-3}$	
										FE	5	23. $\times 10^{-3}$	39. $\times 10^{-3}$	-4.0 $\times 10^{-3}$	
										PS	5	3.8 $\times 10^{-3}$	6.8 $\times 10^{-3}$	-3.0 $\times 10^{-3}$	filter
30	0.4	3.5	3.5 π	33	33/3.5	128	1/ $\sqrt{2}$	1/ $\sqrt{2}$	0.5	FD	5	5.2 $\times 10^{-3}$	9.4 $\times 10^{-2}$	12. $\times 10^{-3}$	
										FE	5	5.5 $\times 10^{-3}$	9.4 $\times 10^{-2}$	-7.2 $\times 10^{-3}$	
										PS	5	3.0 $\times 10^{-3}$	1.8 $\times 10^{-2}$	-4.7 $\times 10^{-3}$	filter
31	0.4	3.5	3.5 π	33	32/3.5	128	-3/ $\sqrt{13}$ +2/ $\sqrt{13}$		0	FD	5	160. $\times 10^{-3}$	160. $\times 10^{-3}$	-160. $\times 10^{-3}$	
										FE	5	26. $\times 10^{-3}$	43. $\times 10^{-3}$	18. $\times 10^{-3}$	
				17 16/3.5						PS	5	4.7 $\times 10^{-3}$	5.3 $\times 10^{-3}$	4.8 $\times 10^{-3}$	filter

Exp't	ϵ	Δ	X_B	N	ν	η	k	ℓ	γ	Duration	RMS(ψ')	RMS(ζ')	NDIF (NRG)	Comments	
32	0.4	3.5	3.5 π	33	32/3.5	128	-3/ $\sqrt{13}$	2/ $\sqrt{13}$	0.5	FD	5	27. $\times 10^{-3}$	19. $\times 10^{-3}$	-39. $\times 10^{-3}$	
										FE	5	7.2 $\times 10^{-3}$	9.7 $\times 10^{-2}$	5. $\times 10^{-3}$	
				17	16/3.5					PS	5	3.8 $\times 10^{-3}$	2.8 $\times 10^{-2}$	9.3 $\times 10^{-3}$	filter
33	0.4	3.5	3.5 π	33	32/3.5	128	3/ $\sqrt{13}$	2/ $\sqrt{13}$	-1.5	FD	5	110. $\times 10^{-4}$	240. $\times 10^{-3}$	-110. $\times 10^{-4}$	
										FE	5	24. $\times 10^{-4}$	40. $\times 10^{-3}$	38. $\times 10^{-4}$	
				17	16/3.5					PS	5	6.3 $\times 10^{-4}$	9.6 $\times 10^{-3}$	-6.2 $\times 10^{-4}$	filter
34	0.4	7.0	7.0 π	33	32/3.5	128	3/ $\sqrt{13}$	2/ $\sqrt{13}$	0	FD	5	740. $\times 10^{-3}$	580. $\times 10^{-3}$	-100. $\times 10^{-3}$	
										FE	5	18. $\times 10^{-3}$	30. $\times 10^{-3}$	-2.2 $\times 10^{-3}$	
										PS	5	5.8 $\times 10^{-3}$	7.4 $\times 10^{-3}$	3.1 $\times 10^{-3}$	filter
35	0.4	7.0	7.0 π	33	32/3.5	128	3/ $\sqrt{13}$	2/ $\sqrt{13}$	0.5	FD	5	62. $\times 10^{-3}$	47. $\times 10^{-2}$	-170. $\times 10^{-3}$	
										FE	5	7.0 $\times 10^{-3}$	25. $\times 10^{-2}$	18. $\times 10^{-3}$	
										PS	5	1.9 $\times 10^{-3}$	2.6 $\times 10^{-2}$	6.3 $\times 10^{-3}$	filter
36	0.4	3.5	3.5 π	17	16/3.5	128	3/ $\sqrt{13}$	2/ $\sqrt{13}$	0	FD	5	600. $\times 10^{-3}$	540. $\times 10^{-3}$	-460. $\times 10^{-3}$	
										FE	5	18. $\times 10^{-3}$	37. $\times 10^{-3}$	-6.6 $\times 10^{-3}$	
										PS	5	4.8 $\times 10^{-3}$	5.3 $\times 10^{-3}$	5.0 $\times 10^{-3}$	filter
37	0.4	3.5	3.5 π	17	16/3.5	128	3/ $\sqrt{13}$	2/ $\sqrt{13}$	0.5	FD	5	120. $\times 10^{-3}$	53. $\times 10^{-2}$	-120. $\times 10^{-3}$	
										FE	5	30. $\times 10^{-3}$	45. $\times 10^{-2}$	-36. $\times 10^{-3}$	
										PS	5	4.1 $\times 10^{-3}$	2.9 $\times 10^{-2}$	9.8 $\times 10^{-3}$	filter

TABLE II

N	Linear Rossby Waves			Nonlinear Rossby Waves		
	FD	FE	PS	FD	FE	PS
17	1.5	3.1	3.7	2.0	3.4	12.1
33	6.3	13.1	10.6	8.3	14.0	31.1
33/17	4.2	4.2	2.9	4.2	4.1	2.6

FIGURE CAPTIONS

Note that contour plots and RMS error curves are not necessarily scaled similarly, even within a single figure.

Figure 1: Linear box mode solution at $t=10$ periods with $(\eta, m, n) = (128, 1, 1)$.

- (a,b) (ζ, ψ) : FD model, $\nu = 16\sqrt{2}$, CI = (0.3, 0.1)
- (c,d) (ζ, ψ) : FE model, $\nu = 16\sqrt{2}$, CI = (0.3, 0.1)
- (e,f) (ζ, ψ) : PS model, $\nu = 8\sqrt{2}$, CI = (0.3, 0.1)

Figure 2: as Figure 1

- (a,b) (ζ', ψ') : FD model, $\nu = 16\sqrt{2}$, CI = (0.08, 0.02)
- (c,d) (ζ', ψ') : FE model, $\nu = 16\sqrt{2}$, CI = $(4.0, 1.0) \times 10^{-3}$
- (e,f) (ζ', ψ') : PS model, $\nu = 8\sqrt{2}$, CI = $(8.0, 3.0) \times 10^{-3}$

Figure 3: as Figure 1

- (a,b) RMS(ζ', ψ'): FD model, $\nu = 16\sqrt{2}$, $0 \leq t \leq 10$ periods
- (c,d) RMS(ζ', ψ'): FE model, $\nu = 16\sqrt{2}$, $0 \leq t \leq 5$ periods
- (e,f) RMS(ζ', ψ'): PS model, $\nu = 8\sqrt{2}$, $0 \leq t \leq 10$ periods

Figure 4: Nonlinear box mode solution at $t=5$ periods with $(\nu, \eta, m, n, \epsilon) = (16\sqrt{2}, 64, 1, 1, 0.2)$.

- (a,b) (ζ, ψ) : FD model, CI = (0.3, 0.1)
- (c,d) (ζ, ψ) : FE model, CI = (0.3, 0.1)
- (e,f) (ζ, ψ) : PS model, CI = (0.4, 0.1)

Figure 5: as Figure 4

- (a,b) (ζ', ψ') : FD model, CI = (0.1, 0.03)
- (c,d) (ζ', ψ') : FE model, CI = $(0.1, 8.0 \times 10^{-3})$
- (e,f) (ζ', ψ') : PS model, CI = (0.4, 0.03)

Figure 6: as Figure 4, CI = 0.1

- (a) ζ' : FD model, $\zeta_{\Sigma} = \zeta_a$
- (b) ζ' : FD model, ζ_{Σ} specified by Kreiss condition
- (c) ζ' : FD model, ζ_{Σ} specified by Sundstrom/Davies condition

Figure 7: as Figure 4

(a,b) (ζ, ψ) : PS model, $t=2$ periods, $CI = (0.4, 0.1)$
(c,d) (ζ, ψ) : PS model, $t=2$ periods, filtered, $CI = (0.4, 0.1)$
(e,f) (ζ, ψ) : PS model, $t=5$ periods, filtered, $CI = (1.0, 0.1)$

Figure 8: Forced nonlinear box modes with $(v, \eta, a, b, \varepsilon) = (32, 128, 1/\sqrt{2}, 1/\sqrt{2}, 0.2)$

(a,b) (ζ, ψ) : FD model, $t=2$ periods, $CI = (0.4, 0.1)$
(c,d) (ζ, ψ) : FE model, $t=5$ periods, $CI = (0.7, 0.1)$
(e,f) (ζ, ψ) : PS model, $t=5$ periods, $CI = (0.4, 0.1)$

Figure 9: as Figure 8

(a,b) (ζ', ψ') : FD model, $t=2$ periods, $CI = (0.04, 1.0 \times 10^{-3})$
(c,d) (ζ', ψ') : FE model, $t=5$ periods, $CI = (0.1, 4.0 \times 10^{-4})$
(e,f) (ζ', ψ') : PS model, $t=5$ periods, $CI = (0.06, 2.0 \times 10^{-4})$

Figure 10: as Figure 8

(a,b) $RMS(\zeta', \psi')$: FD model, $0 \leq t \leq 2$ periods
(c,d) $RMS(\zeta', \psi')$: FE model, $0 \leq t \leq 5$ periods
(e,f) $RMS(\zeta', \psi')$: PS model, $0 \leq t \leq 5$ periods

Figure 11: Case 1 linear north wall forced modes at $t=5$ periods with
 $(v, \eta) = (32/3, 64)$

(a,b) (ζ, ψ) : FD model, $CI = (0.3, 0.1)$
(c,d) (ζ, ψ) : FE model, $CI = (0.3, 0.1)$
(e,f) (ζ, ψ) : PS model, $CI = (0.3, 0.1)$

Figure 12: as Figure 11.

(a,b) (ζ', ψ') : FD model, $CI = (0.1, 0.05)$
(c,d) (ζ', ψ') : FE model, $CI = (0.01, 8.0 \times 10^{-3})$
(e,f) (ζ', ψ') : PS model, $CI = (0.01, 8.0 \times 10^{-3})$

Figure 13: as Figure 11, $0 \leq t \leq 5$ periods

(a,b) $RMS(\zeta', \psi')$: FD model
(c,d) $RMS(\zeta', \psi')$: FE model
(e,f) $RMS(\zeta', \psi')$: PS model

Figure 14: Case 2 linear north wall forced modes at $t=5$ periods, with
 $(\nu, \eta) = (64/3, 64)$

(a,b) (ζ, ψ) : FD model, CI = (10.0, 3.0)
(c,d) (ζ, ψ) : FE model, CI = (10.0, 3.0)
(e,f) (ζ, ψ) : PS model, CI = (10.0, 2.0)

Figure 15: as Figure 14

(a,b) (ζ', ψ') : FD model, CI = (2.0, 0.06)
(c,d) (ζ', ψ') : FE model, CI = (0.5, 0.01)
(e,f) (ζ', ψ') : PS model, CI = (0.1, 0.01)

Figure 16: as Figure 14, $0 \leq t \leq 5$ periods

(a,b) $\text{RMS}(\zeta', \psi')$: FD model
(c,d) $\text{RMS}(\zeta', \psi')$: FE model
(e,f) $\text{RMS}(\zeta', \psi')$: PS model

Figure 17: Case 1 nonlinear north wall forced modes at $t=5$ periods with
 $(\nu, \eta, \epsilon) = (32/3, 64, 0.2)$

(a,b) (ζ, ψ) : FD model, CI = (2.0, 0.1)
(c,d) (ζ, ψ) : FE model, CI = (2.0, 0.1)
(e,f) (ζ, ψ) : PS model, CI = (2.0, 0.1)

Figure 18: as Figure 17, $t=0.5$ periods

(a,b) (ζ', ψ') : FD model, CI = (0.06, 0.01)
(c,d) (ζ', ψ') : FE model, CI = (0.04, 0.01)
(e,f) (ζ', ψ') : PS model, CI = (0.04, 0.01)

Figure 19: as Figure 17, $t=5.0$ periods

(a,b) (ζ', ψ') : FD model, CI = (2.0, 0.1)
(c,d) (ζ', ψ') : FE model, CI = (2.0, 0.1)
(e,f) (ζ', ψ') : PS model, CI = (2.0, 0.07)

Figure 20: as Figure 17

(a,b) (ζ, ψ) : PS model, $t=1.5$ periods, CI = (3.0, 0.1)
(c,d) (ζ, ψ) : PS model, $t=1.5$ periods, filtered, CI = (0.9, 0.1)
(e,f) (ζ, ψ) : PS model, $t=5.0$ periods, filtered, CI = (2.0, 0.1)

Figure 21: Nonlinear Rossby waves at $t=5$ periods with $(\nu, \eta, k, \ell, \varepsilon, \gamma) = (32/3.5, 64, 3/\sqrt{13}, 2/\sqrt{13}, 0.4, 0.0)$

(a,b) (ζ, ψ) : FD model, CI = (0.2, 0.2)
 (c,d) (ζ, ψ) : FE model, CI = (0.2, 0.2)
 (e,f) (ζ, ψ) : PS model, CI = (0.2, 0.2), filtered

Figure 22: as Figure 21

(a,b) (ζ', ψ') : FD model, CI = (0.04, 0.04)
 (c,d) (ζ', ψ') : FE model, CI = (0.05, 0.02)
 (e,f) (ζ', ψ') : PS model, CI = $(8.0 \times 10^{-3}, 6.0 \times 10^{-3})$, filtered.

Figure 23: as Figure 21, $0 \leq t \leq 5$ periods

(a,b) $\text{RMS}(\zeta', \psi')$: FD model
 (c,d) $\text{RMS}(\zeta', \psi')$: FE model
 (e,f) $\text{RMS}(\zeta', \psi')$: PS model, filtered

Figure 24: as Figure 21

(a,b) (ζ, ψ) : PS model, $t=2.5$ periods, CI = (0.6, 0.2)
 (c,d) (ζ, ψ) : PS model, $t=2.5$ periods, filtered, CI = (0.2, 0.2)
 (e,f) (ζ, ψ) : PS model, $t=5.0$ periods, filtered, CI = (0.2, 0.2)

Figure 25: Nonlinear Rossby waves with $(\nu, \eta, k, \ell, \varepsilon, \gamma) = (32/3.5, 64, 3/\sqrt{13}, 2/\sqrt{13}, 0.4, 0.5)$

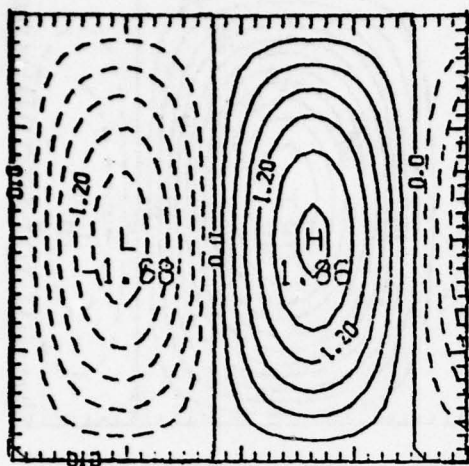
(a,b) (ζ, ψ) : FD model, $t=5$ periods, CI = (0.2, 0.7)
 (c,d) (ζ, ψ) : FE model, $t=5$ periods, CI = (0.2, 0.7)
 (e,f) (ζ, ψ) : PS model, $t=5$ periods, CI = (0.2, 0.7), filtered

Figure 26: as Figure 25

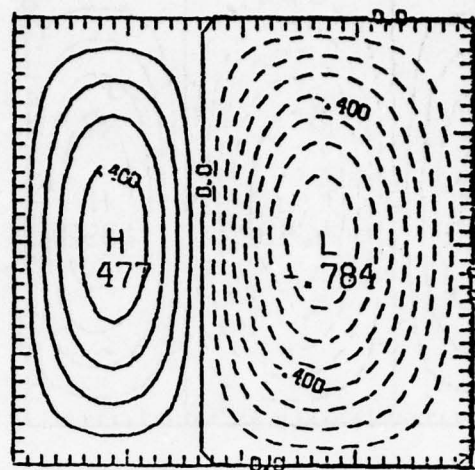
(a,b) (ζ', ψ') : FD model, $t=5$ periods, CI = (0.07, 0.03)
 (c,d) (ζ', ψ') : FE model, $t=5$ periods, CI = (0.04, 0.01)
 (e,f) (ζ', ψ') : PS model, $t=5$ periods, CI = $(0.01, 5.0 \times 10^{-3})$,
 filtered

Figure 27: as Figure 25, $0 \leq t \leq 5$ periods

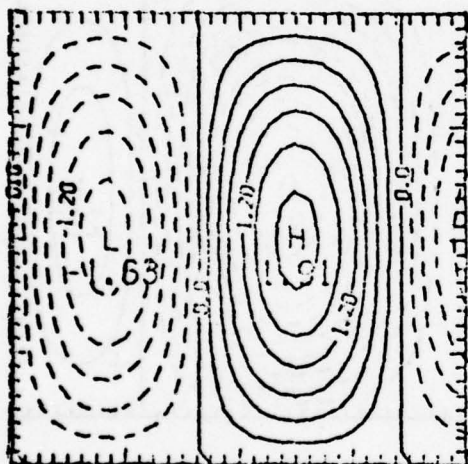
(a,b) $\text{RMS}(\zeta', \psi')$: FD model
 (c,d) $\text{RMS}(\zeta', \psi')$: FE model
 (e,f) $\text{RMS}(\zeta', \psi')$: PS model, filtered



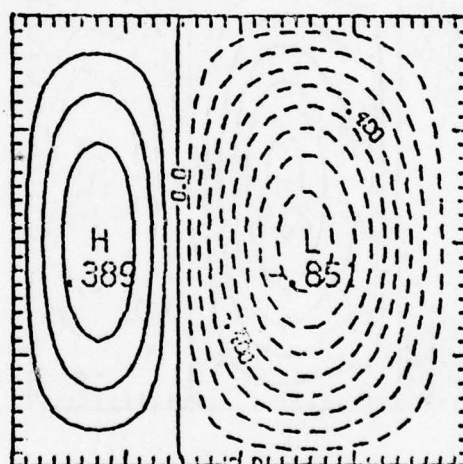
(a)



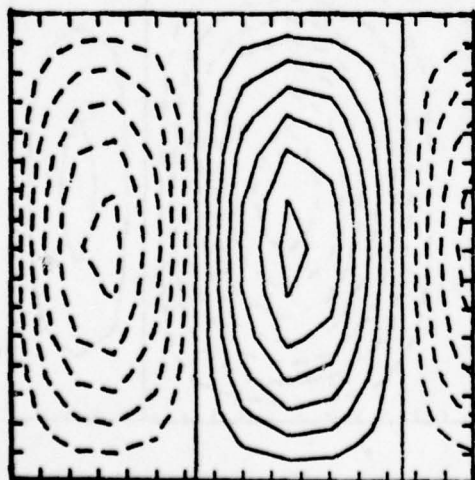
(b)



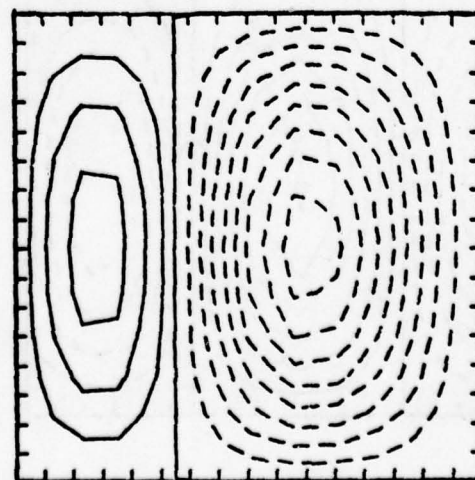
(c)



(d)

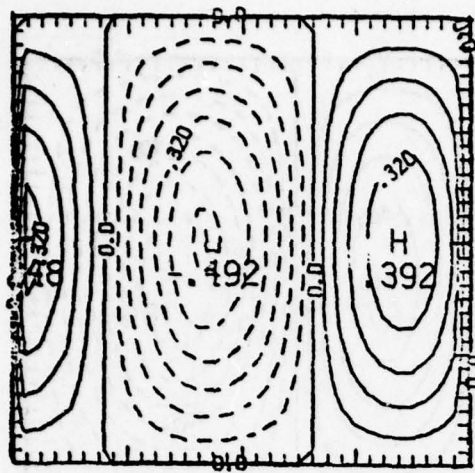


(e)

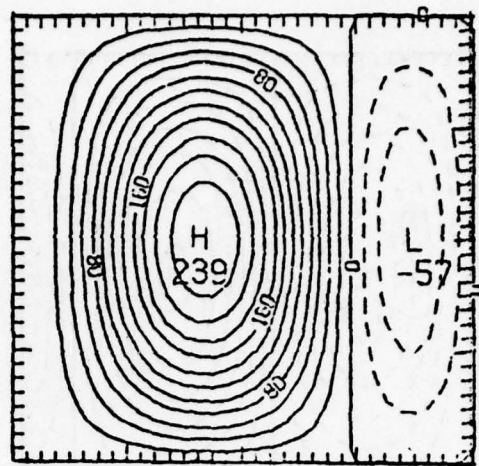


(f)

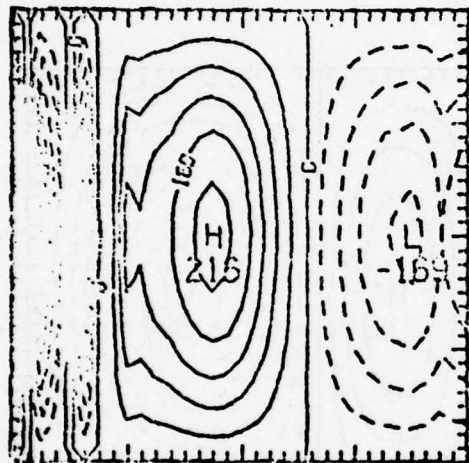
Figure 1



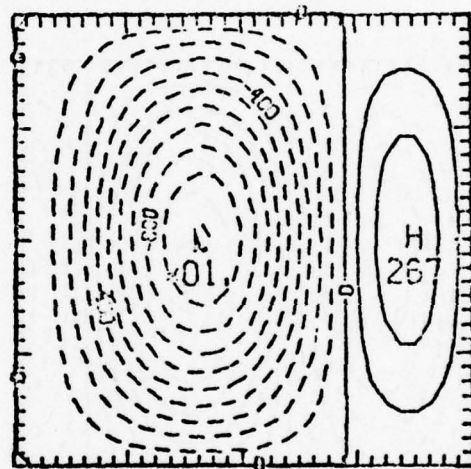
(a)



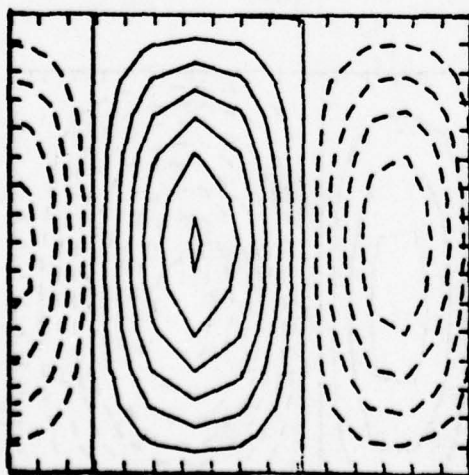
(b)



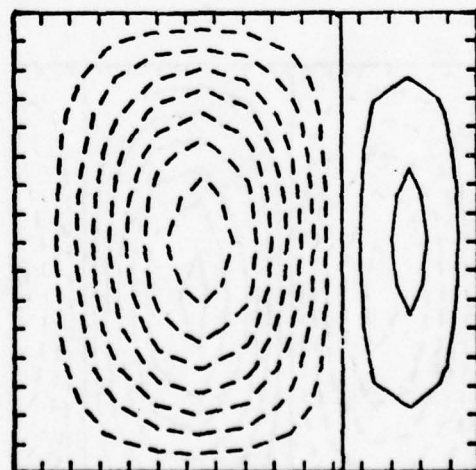
(c)



(d)

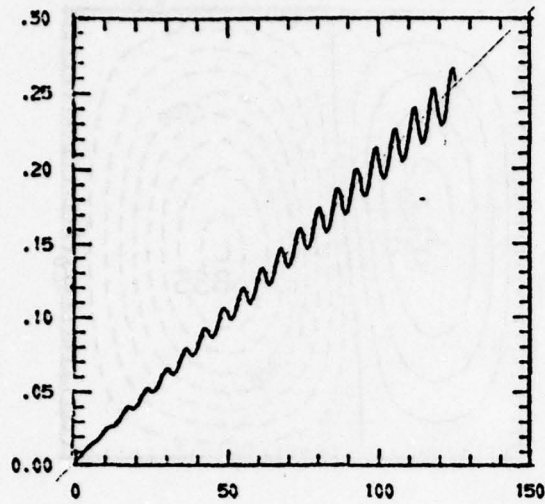


(e)

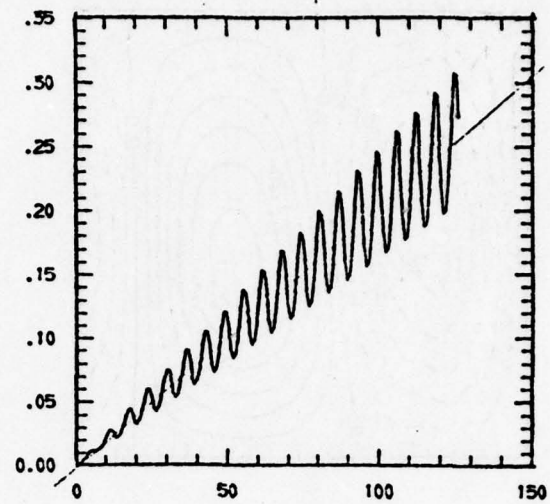


(f)

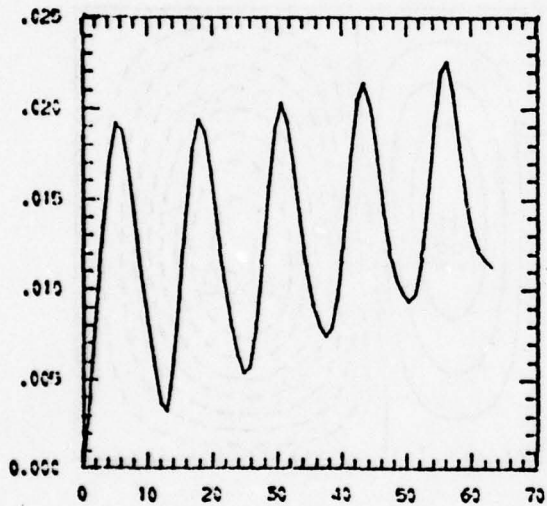
Figure 2



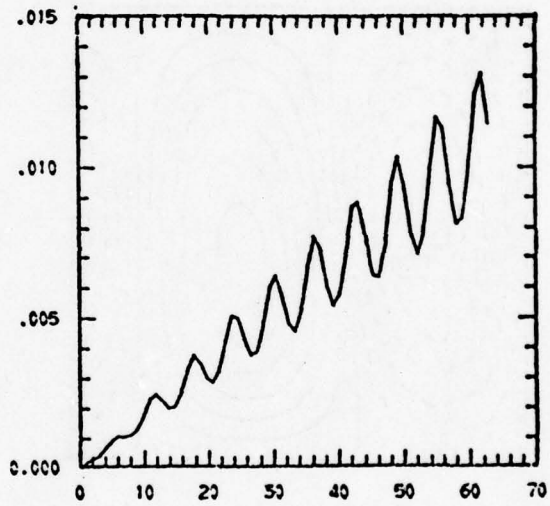
(a)



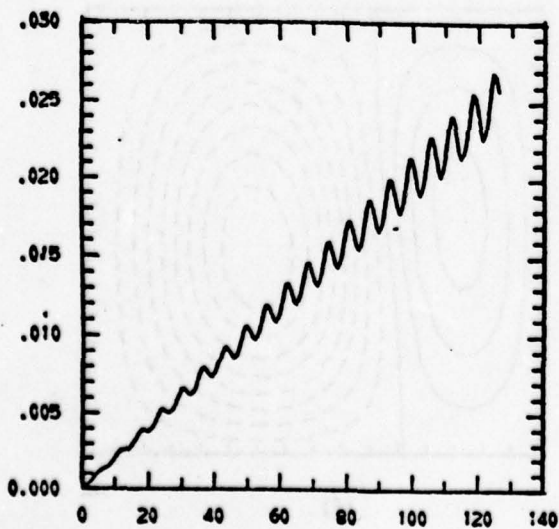
(b)



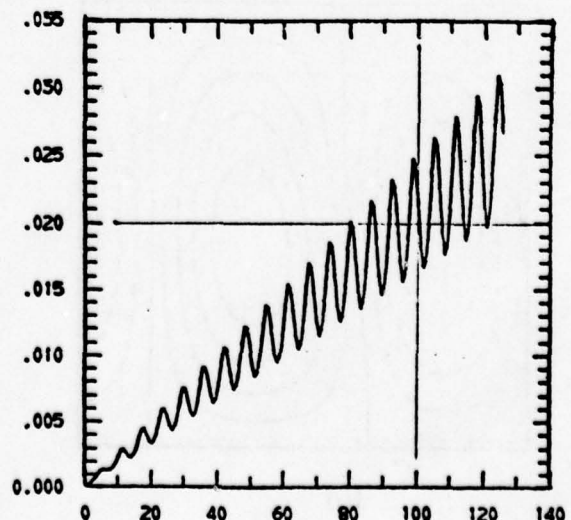
(c)



(d)

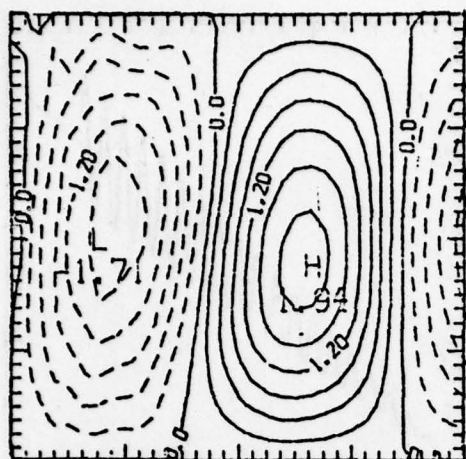


(e)

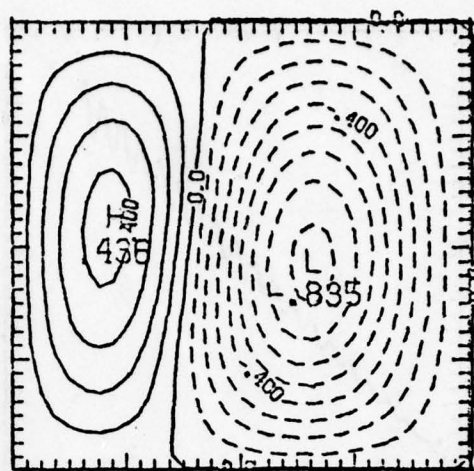


(f)

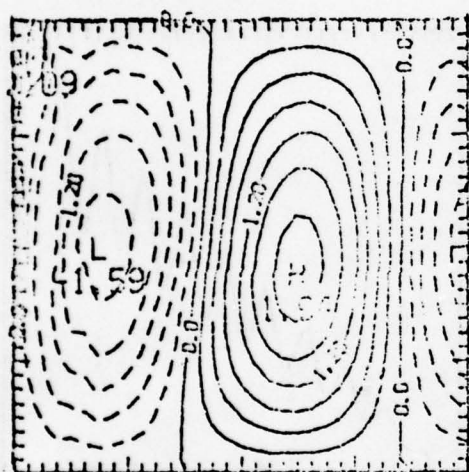
Figure 3



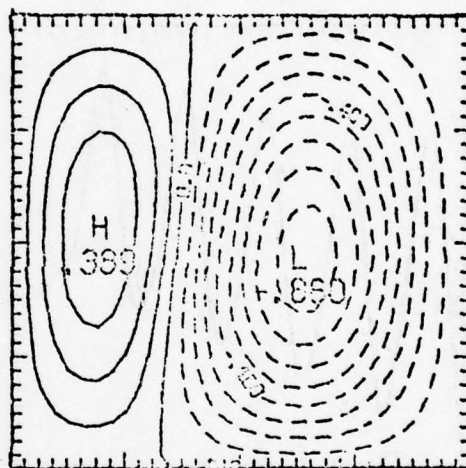
(a)



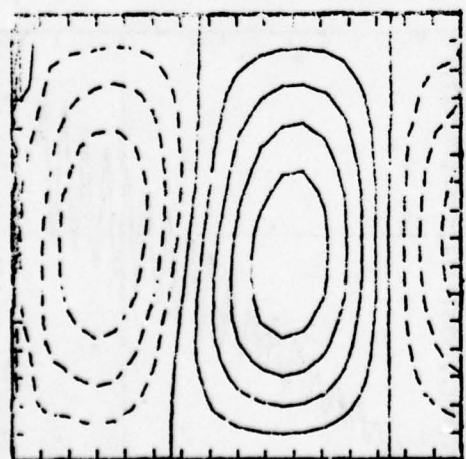
(b)



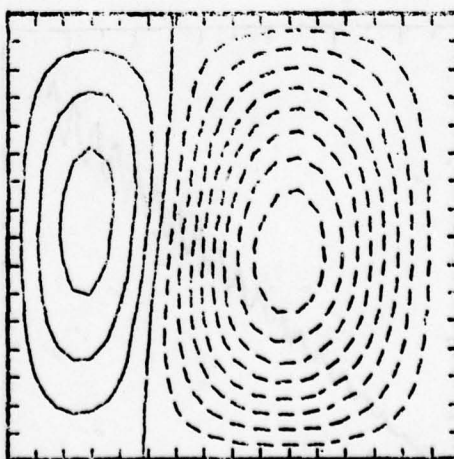
(c)



(d)

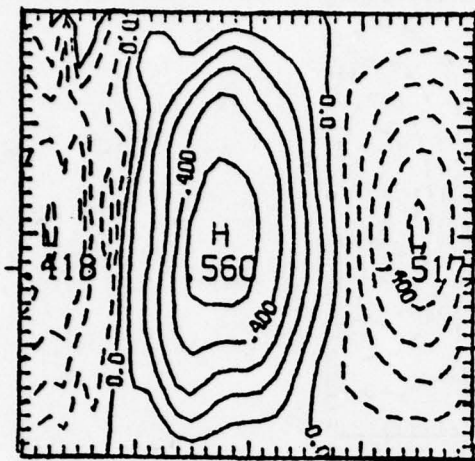


(e)

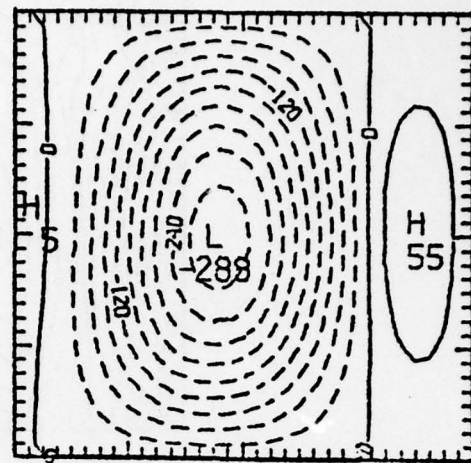


(f)

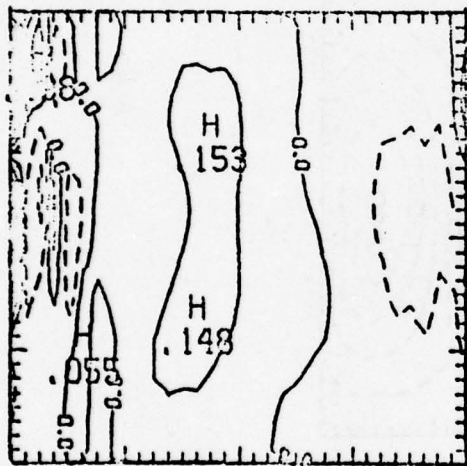
Figure 4



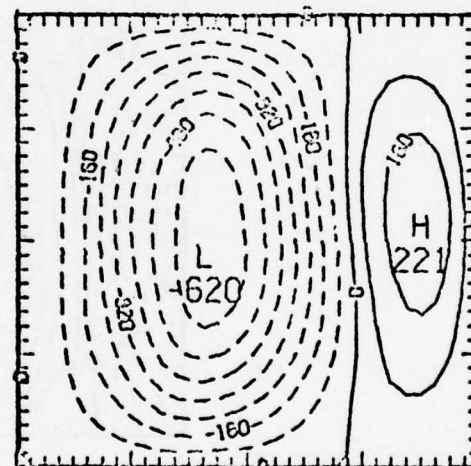
(a)



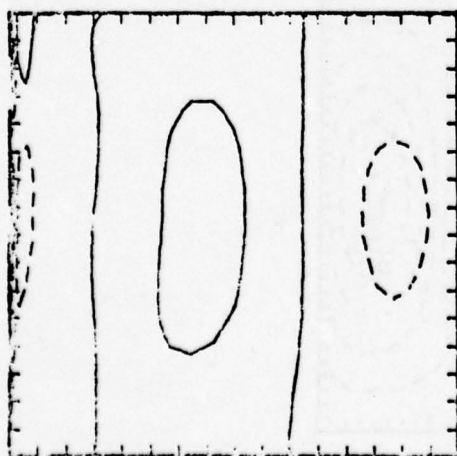
(b)



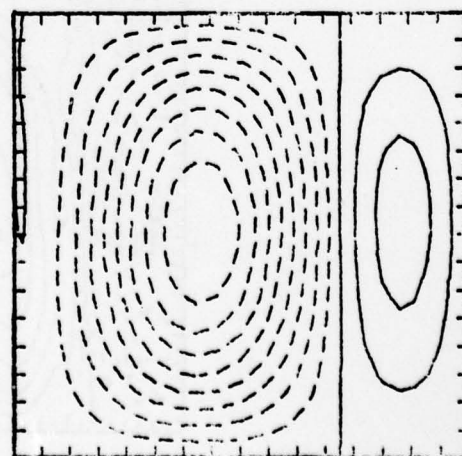
(c)



(d)

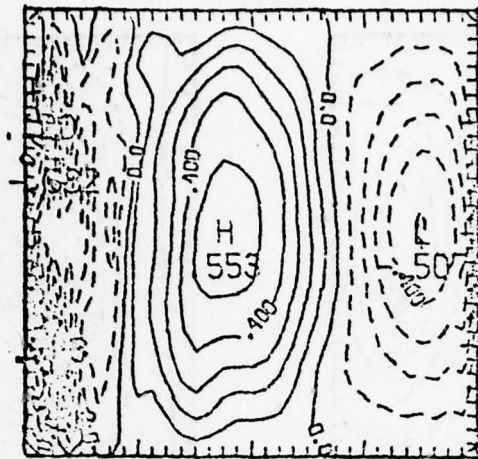


(e)

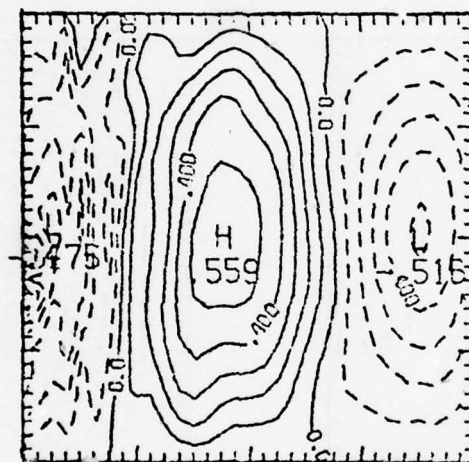


(f)

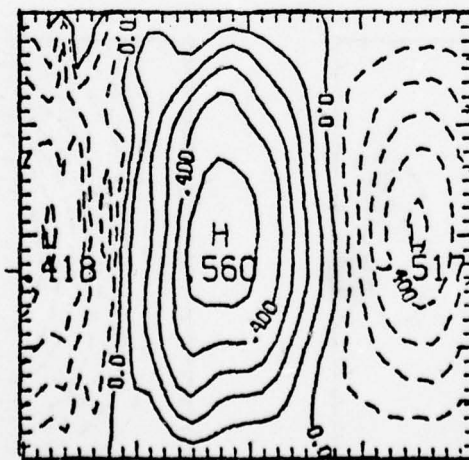
Figure 5



(a)

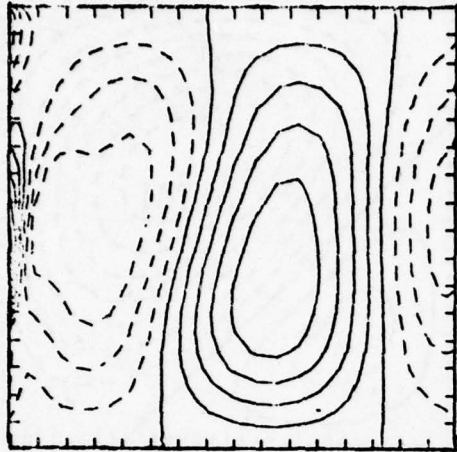


(b)

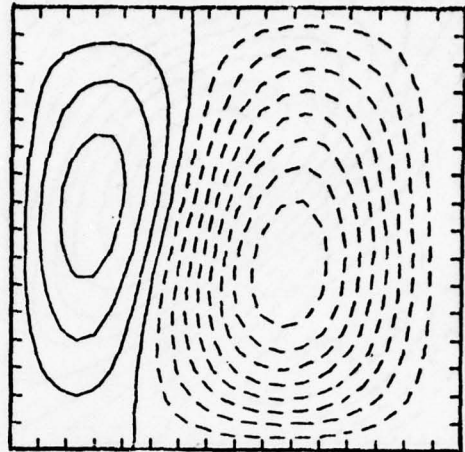


(c)

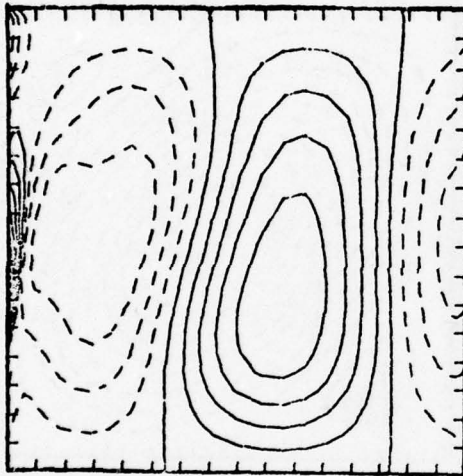
Figure 6



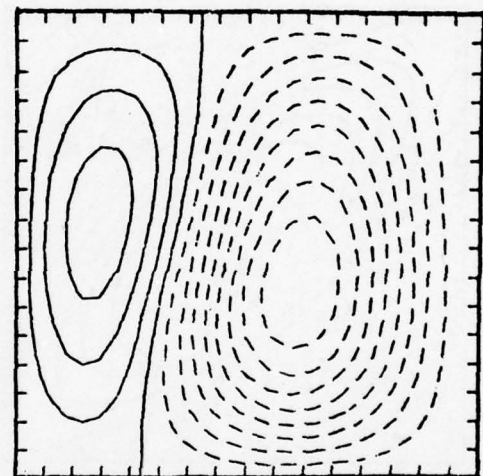
(a)



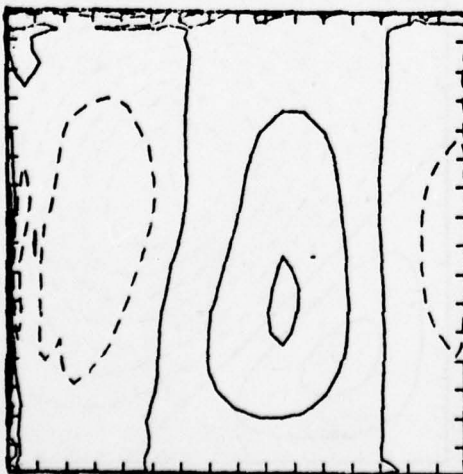
(b)



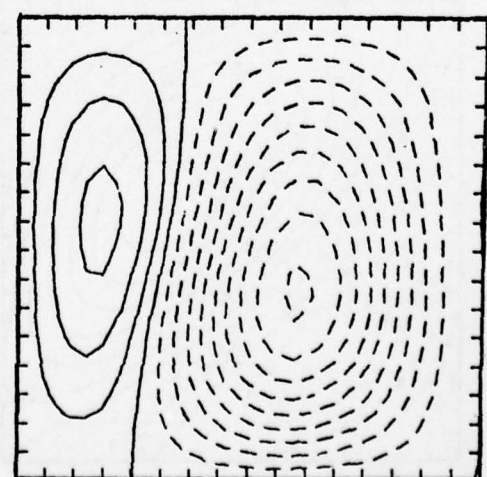
(c)



(d)

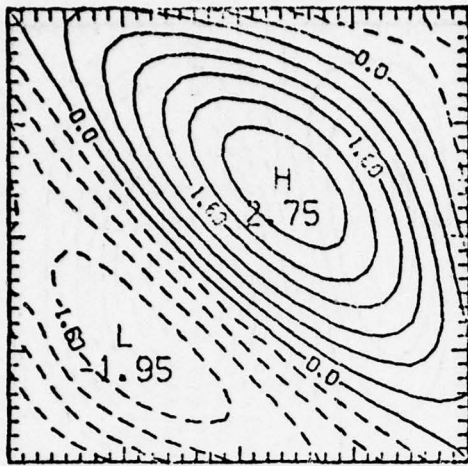


(e)

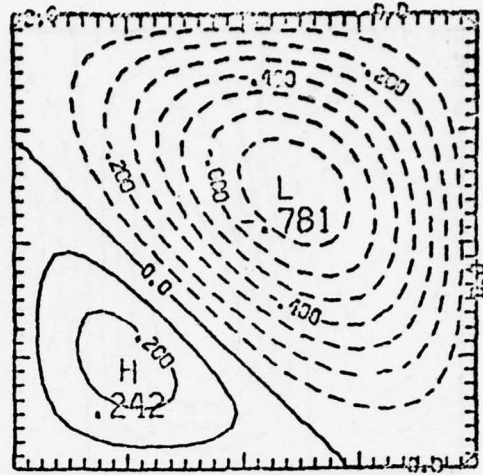


(f)

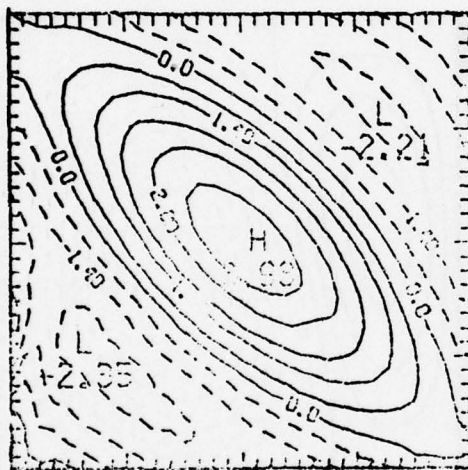
Figure 7



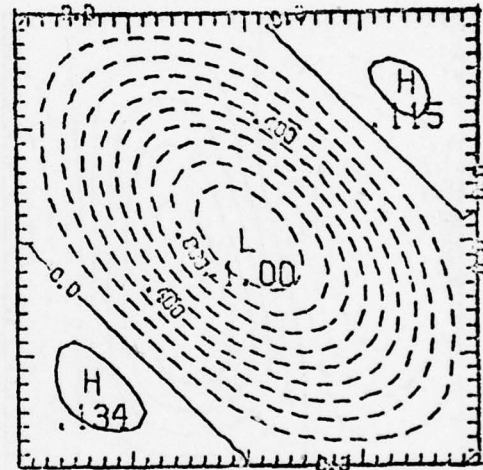
(a)



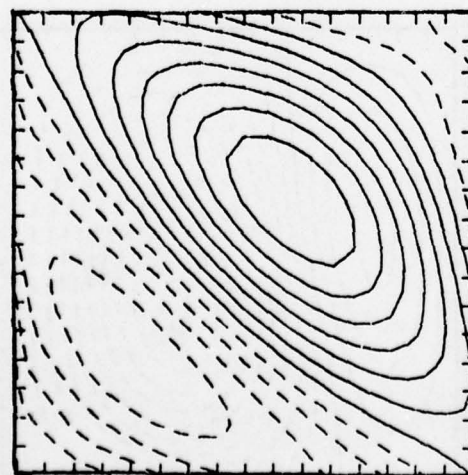
(b)



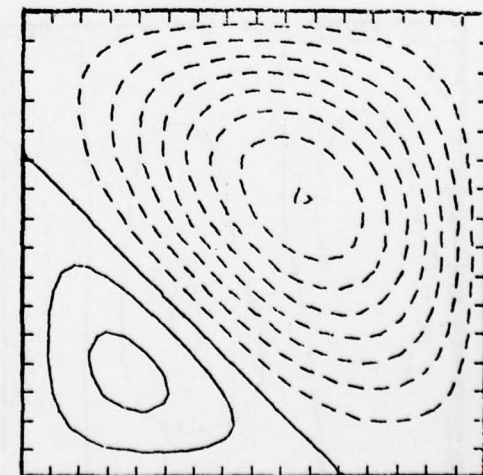
(c)



(d)

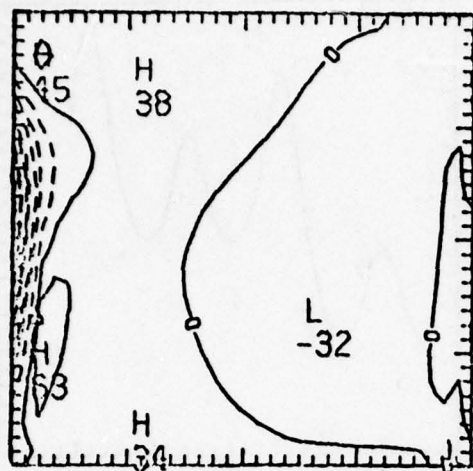


(e)

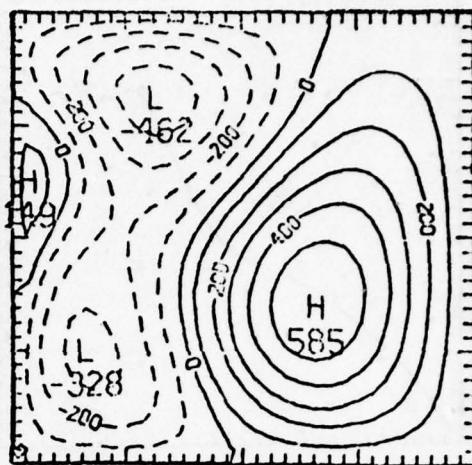


(f)

Figure 8



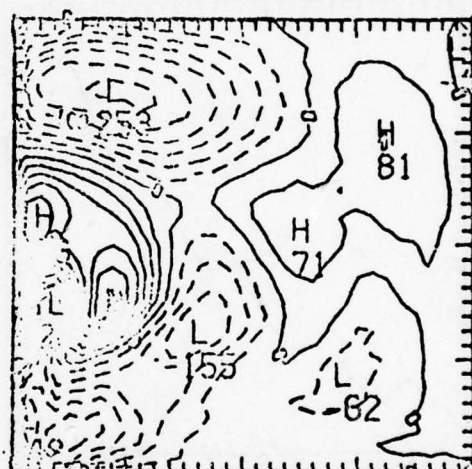
(a)



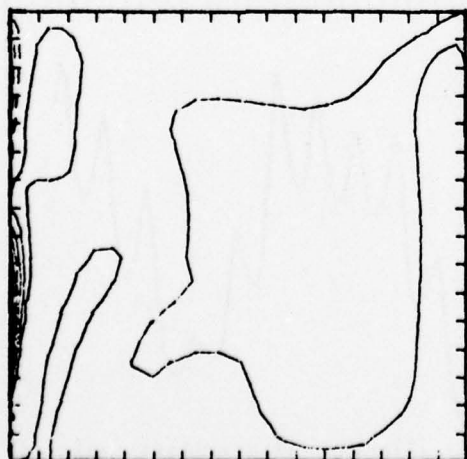
(b)



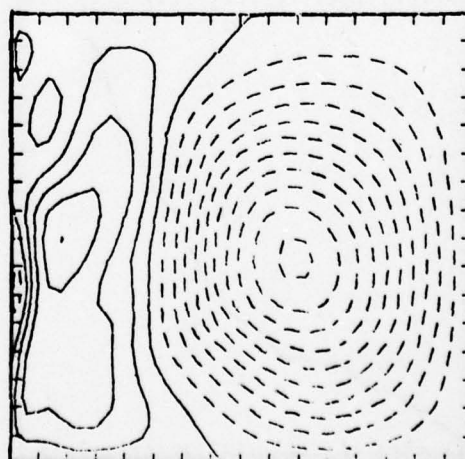
(c)



(d)

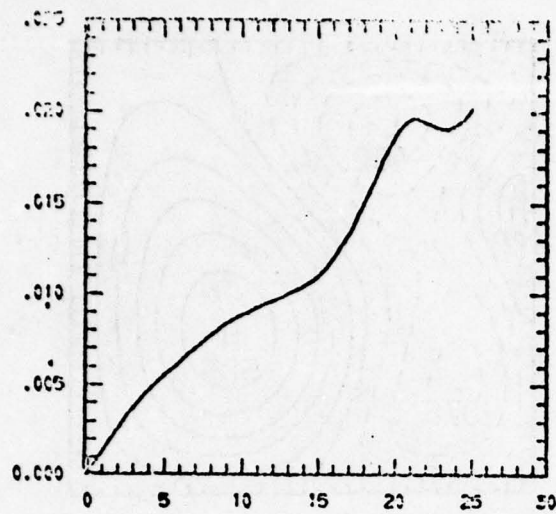


(e)

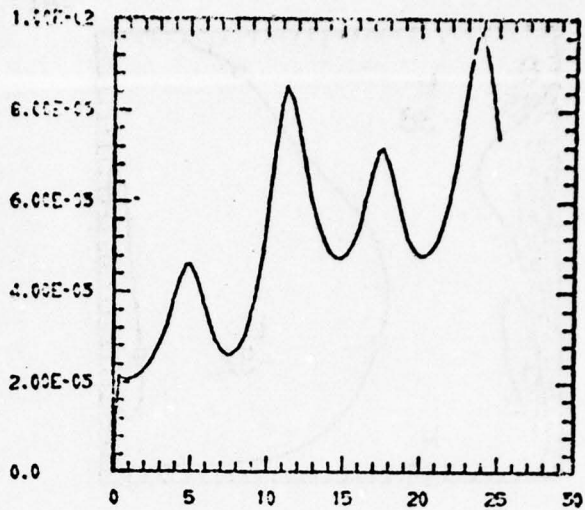


(f)

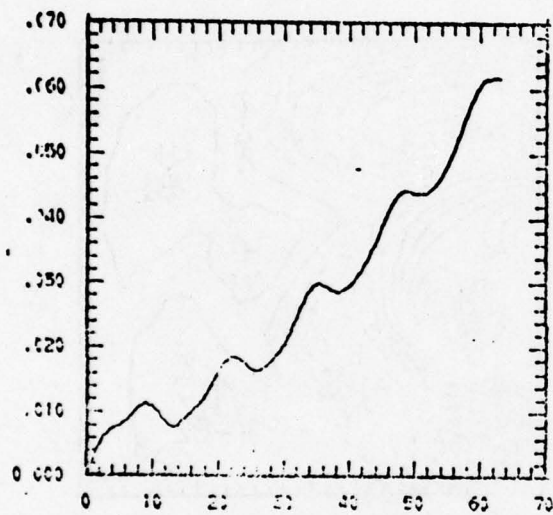
Figure 9



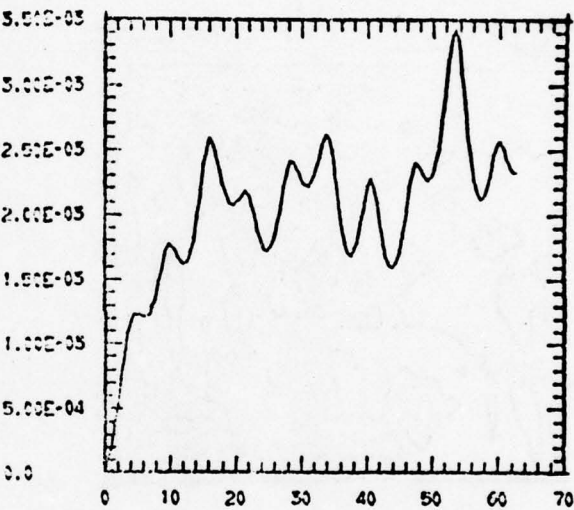
(a)



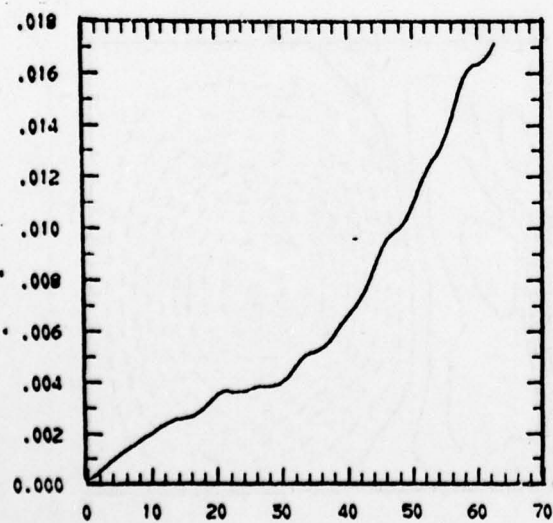
(b)



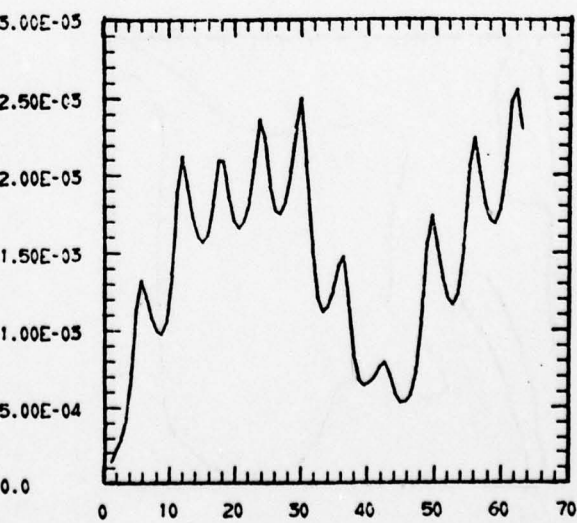
(c)



(d)

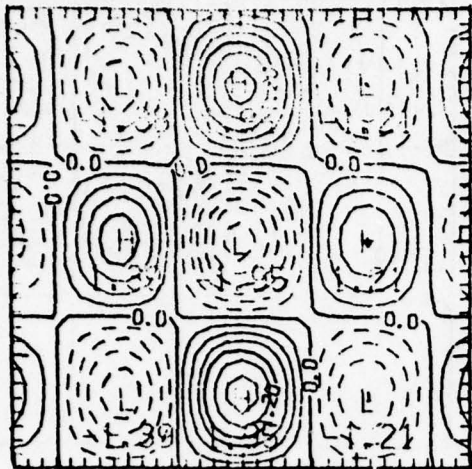


(e)

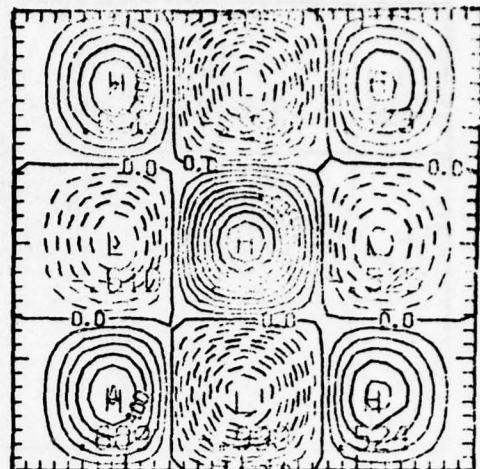


(f)

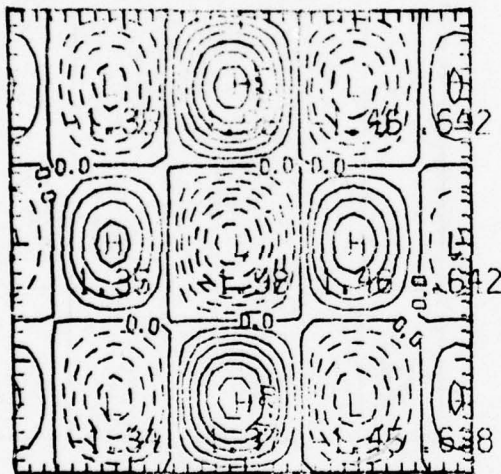
Figure 10



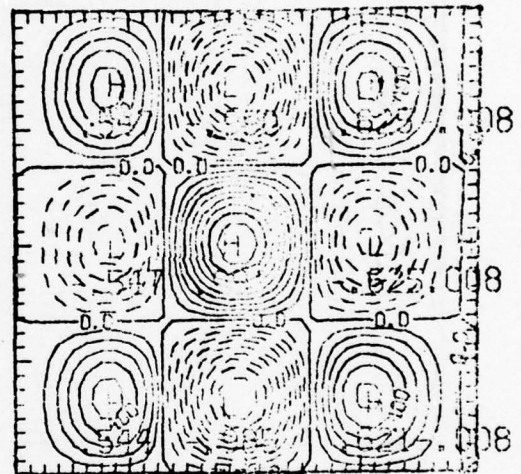
(a)



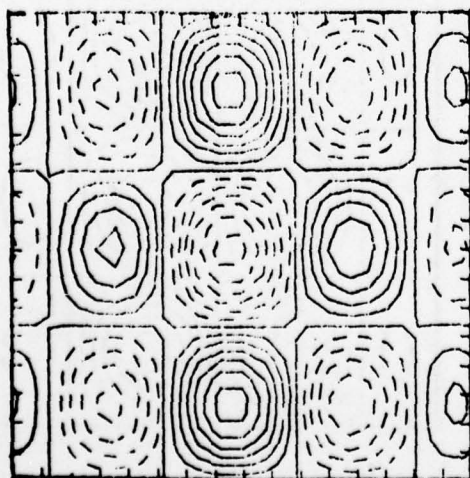
(b)



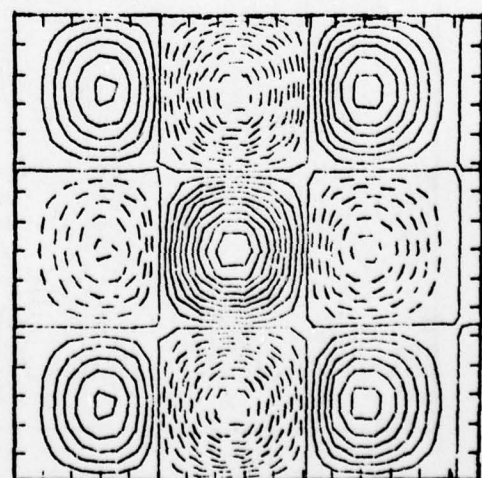
(c)



(d)

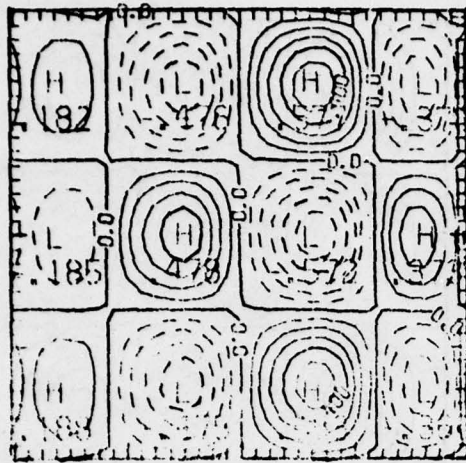


(e)

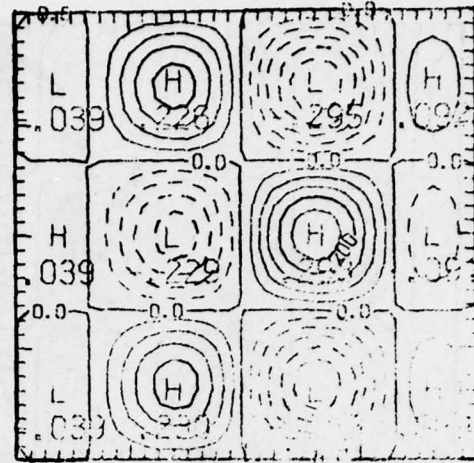


(f)

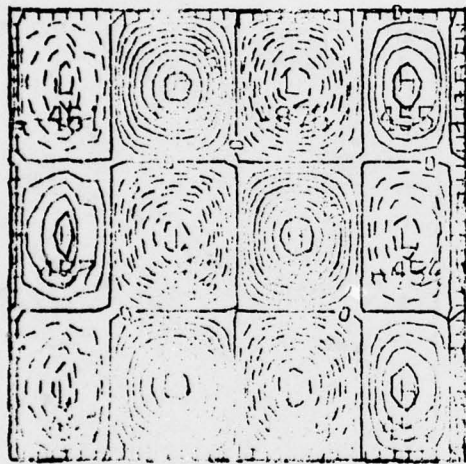
Figure 11



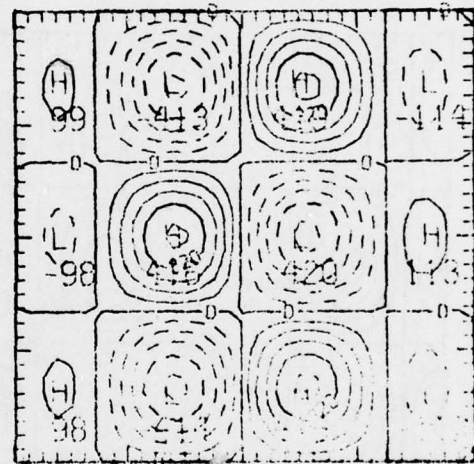
(a)



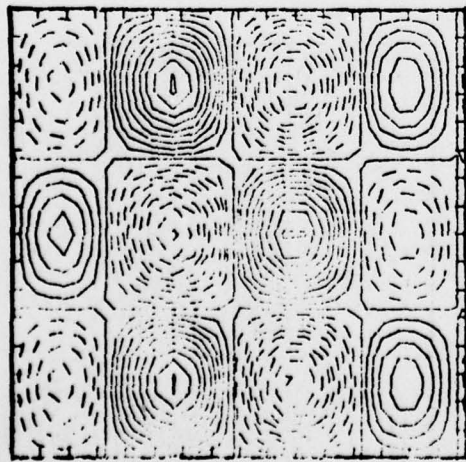
(b)



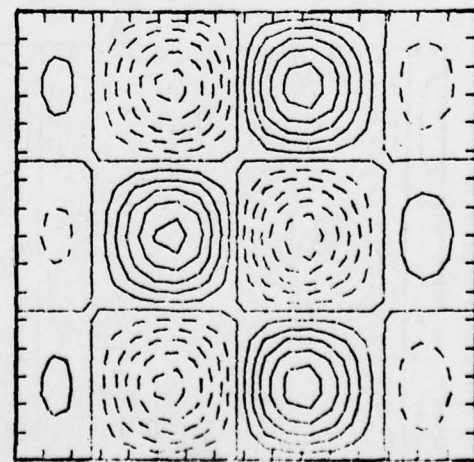
(c)



(d)

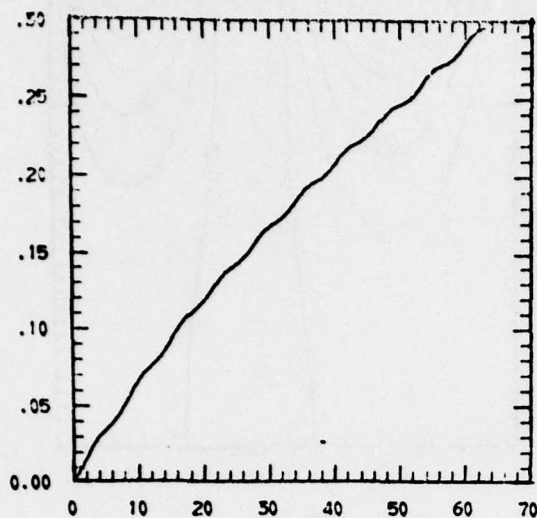


(e)

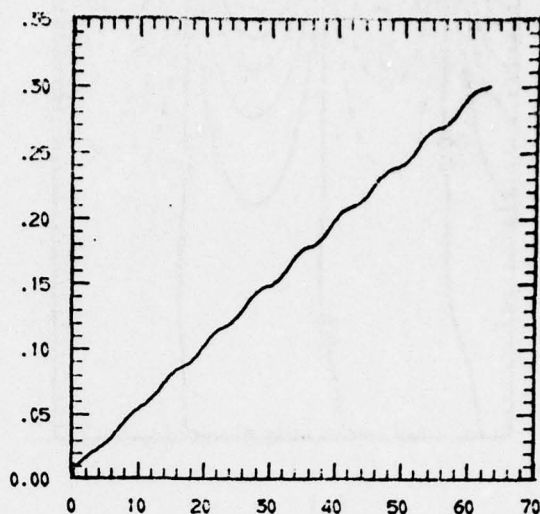


(f)

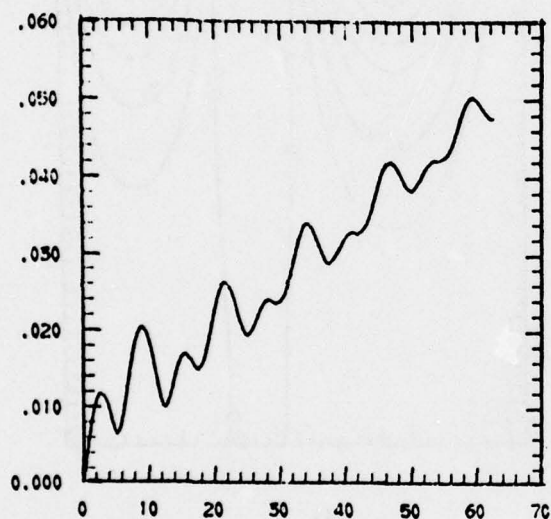
Figure 12



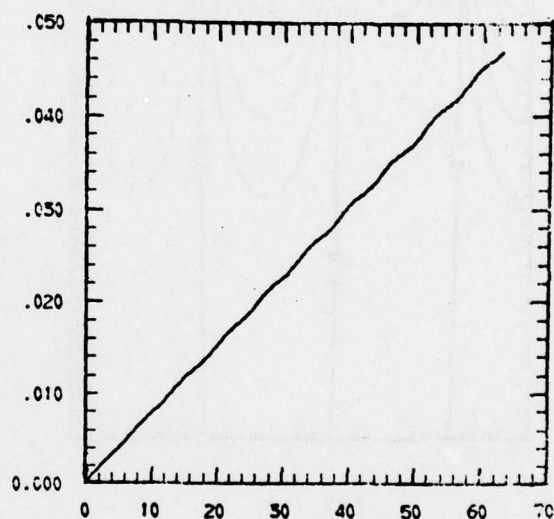
(a)



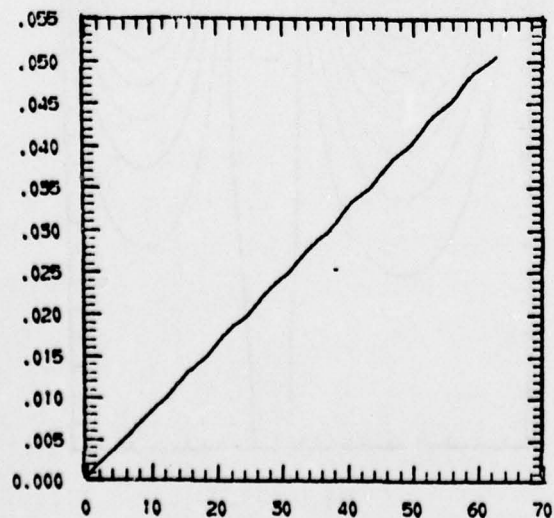
(b)



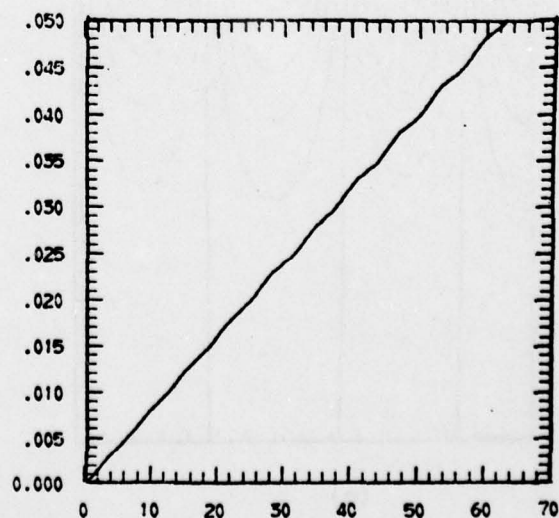
(c)



(d)

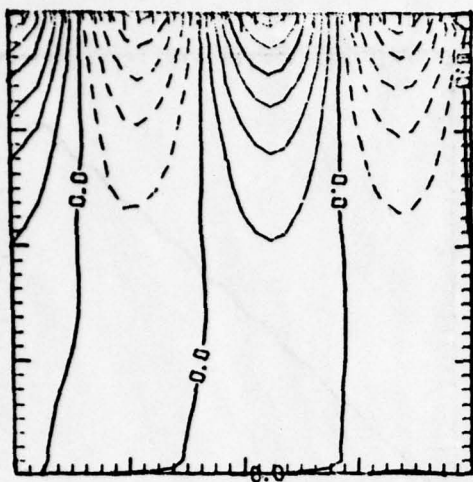


(e)

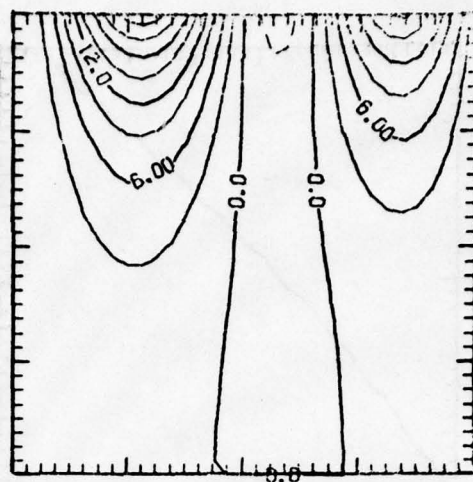


(f)

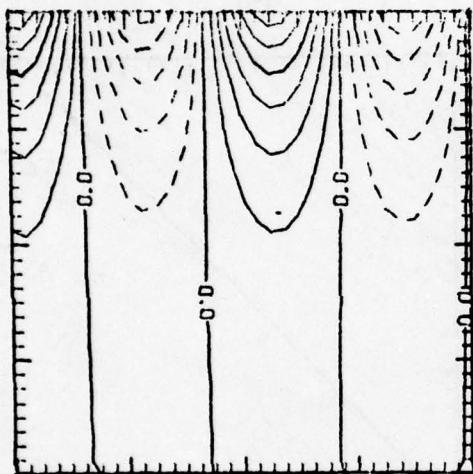
Figure 13



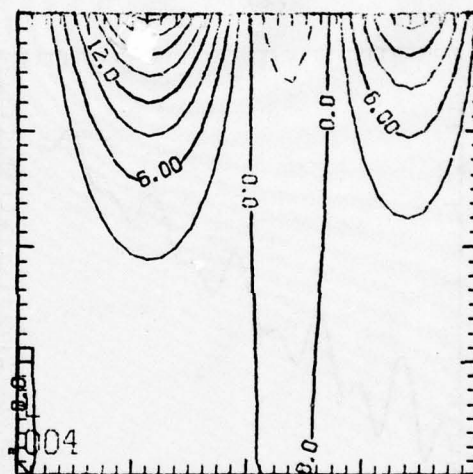
(a)



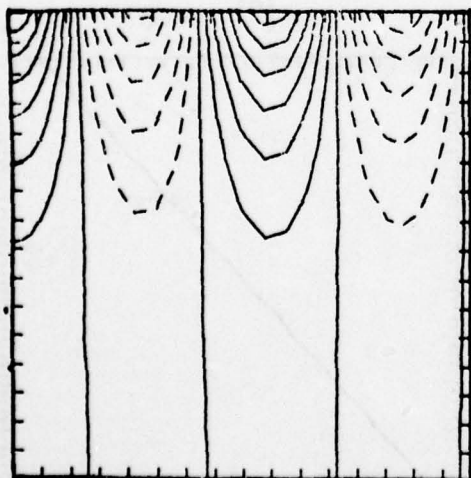
(b)



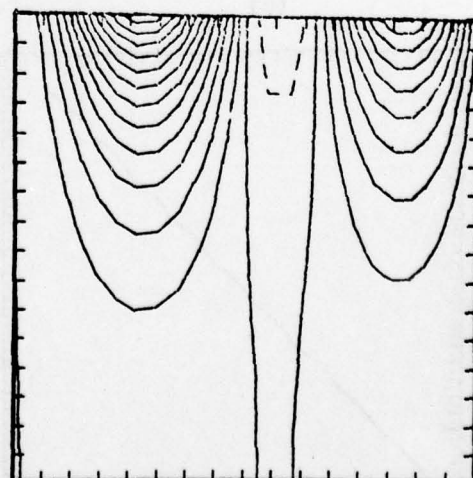
(c)



(d)

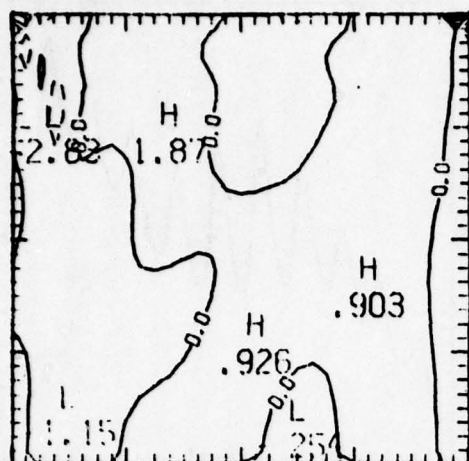


(e)

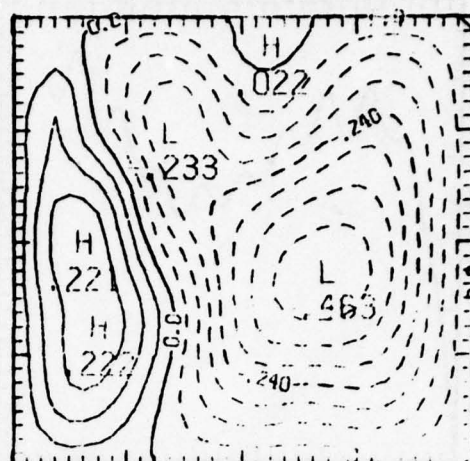


(f)

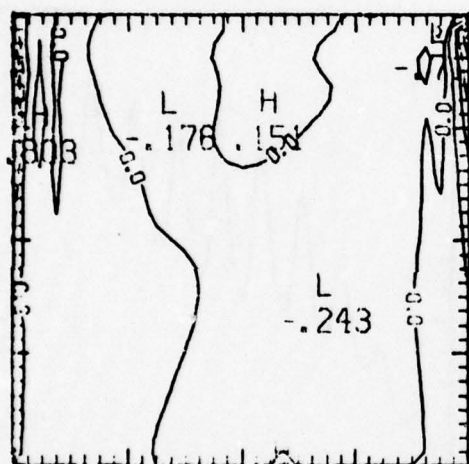
Figure 14



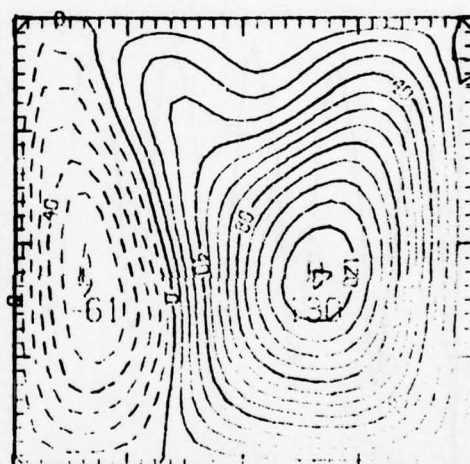
(a)



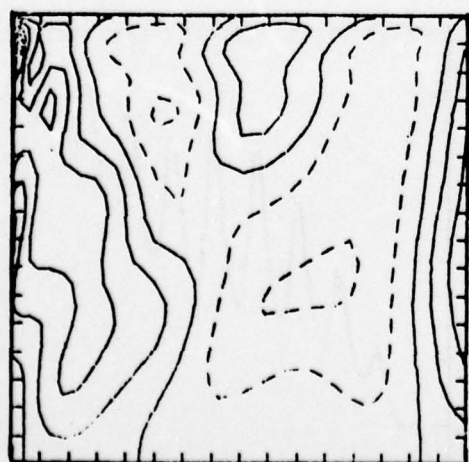
(b)



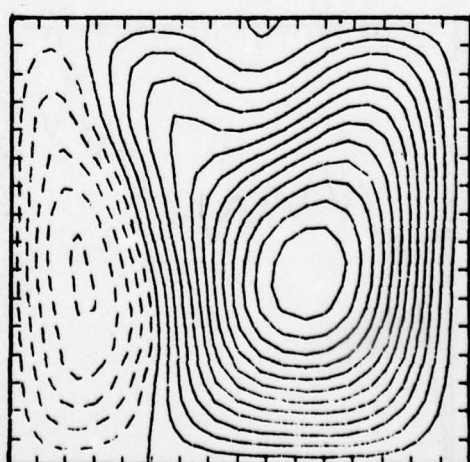
(c)



(d)

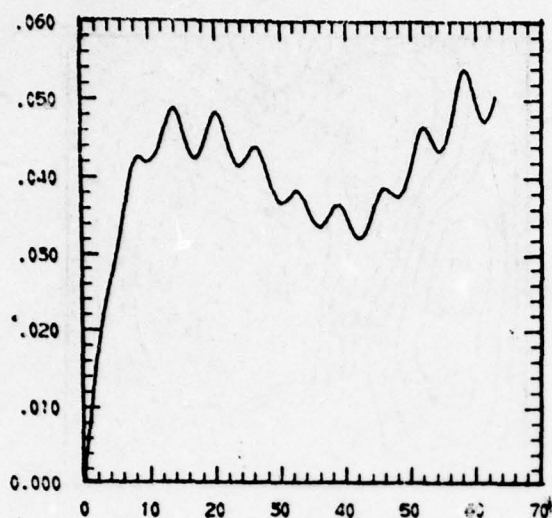


(e)

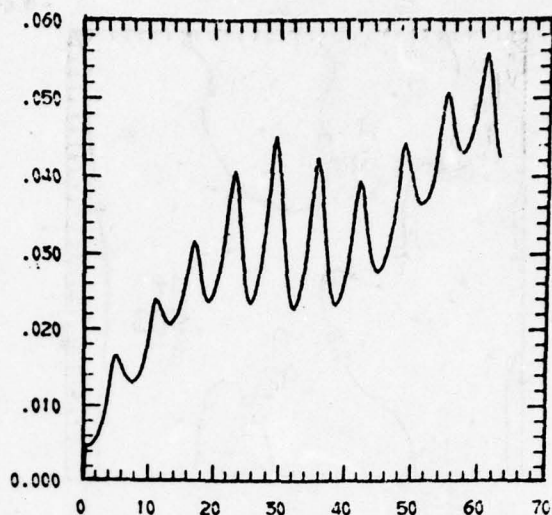


(f)

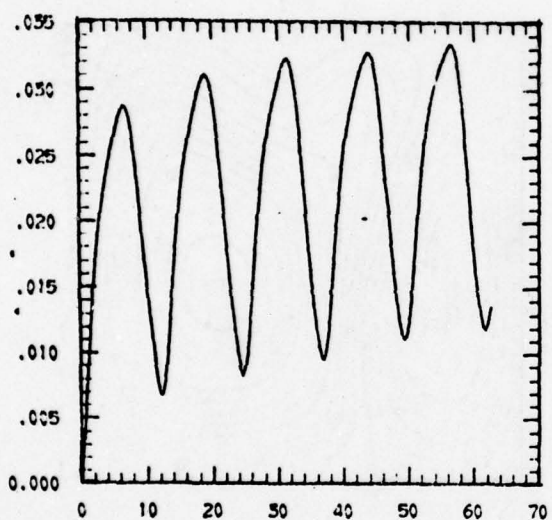
Figure 15



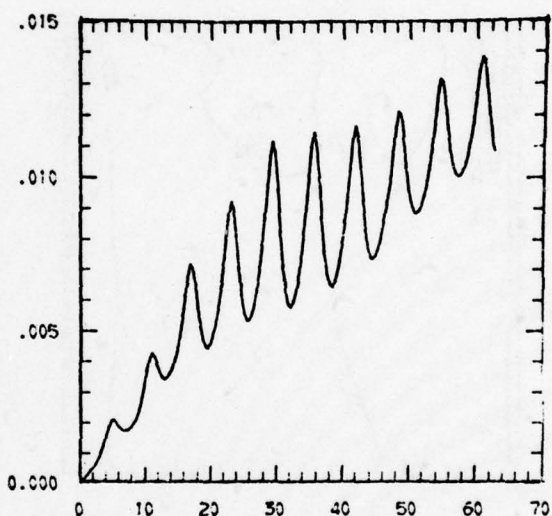
(a)



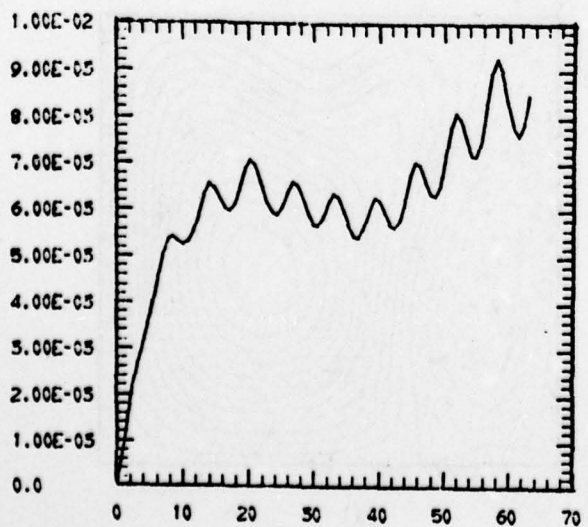
(b)



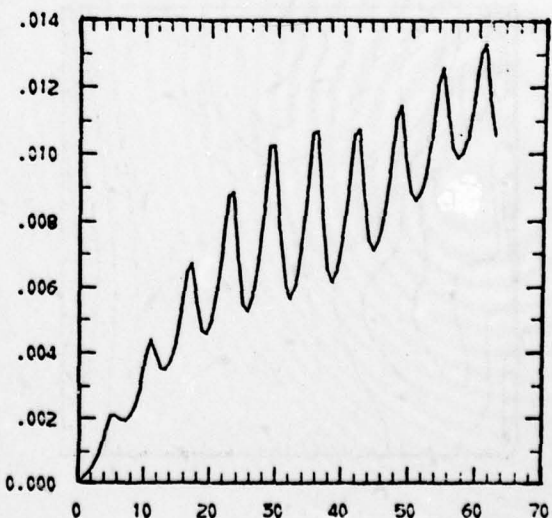
(c)



(d)

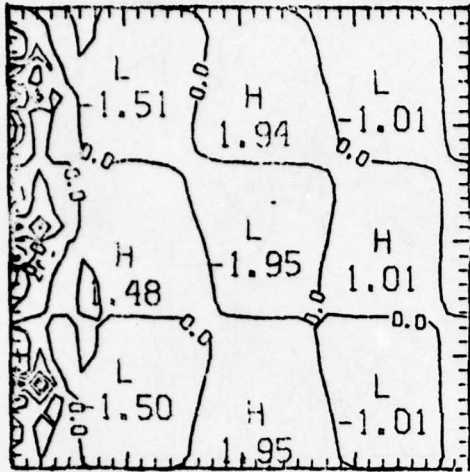


(e)

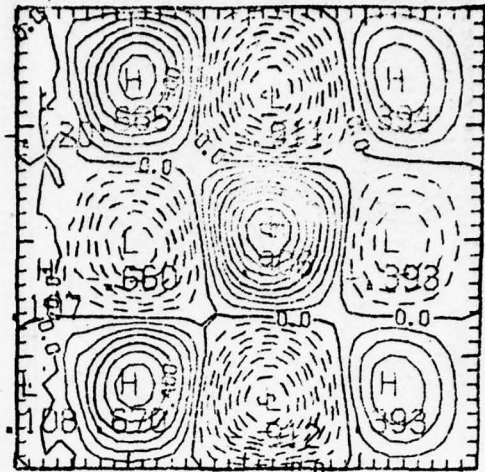


(f)

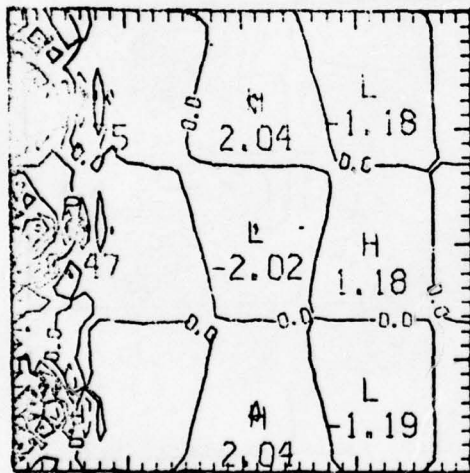
Figure 16



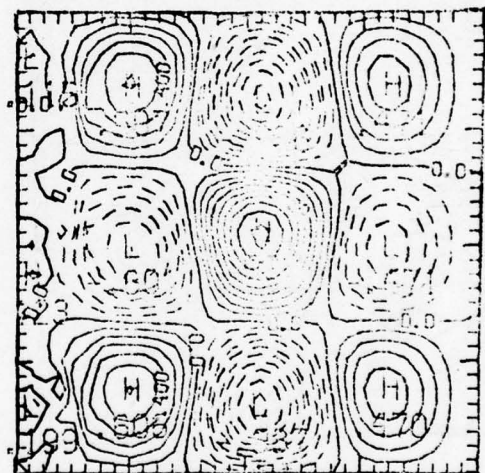
(a)



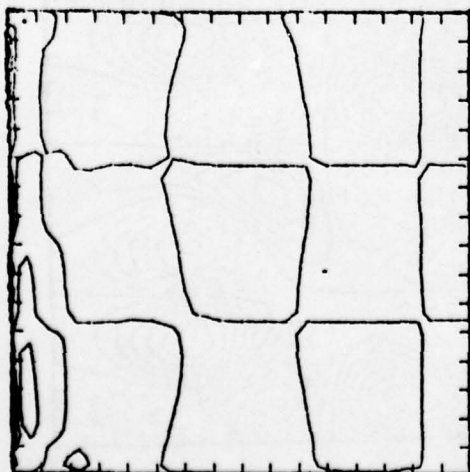
(b)



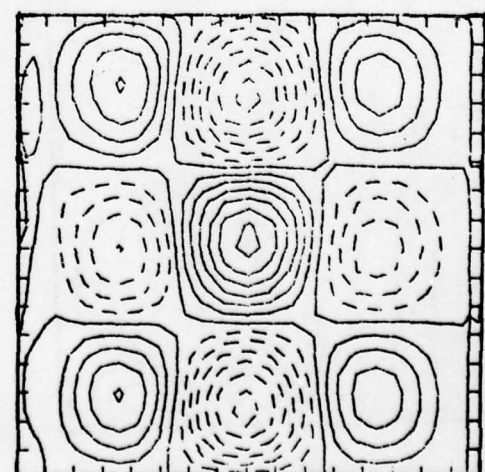
(c)



(d)

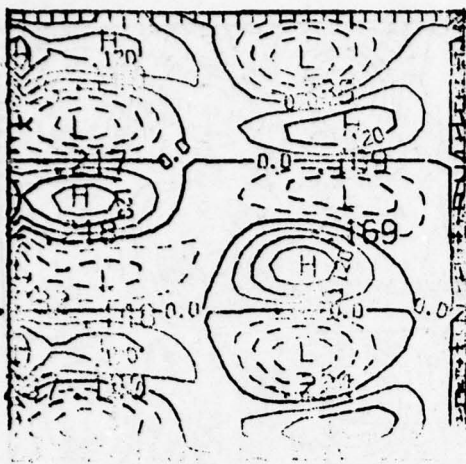


(e)

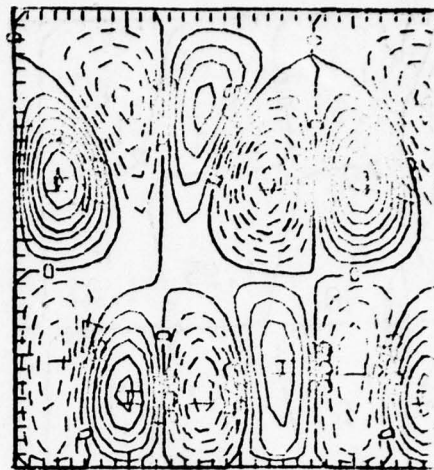


(f)

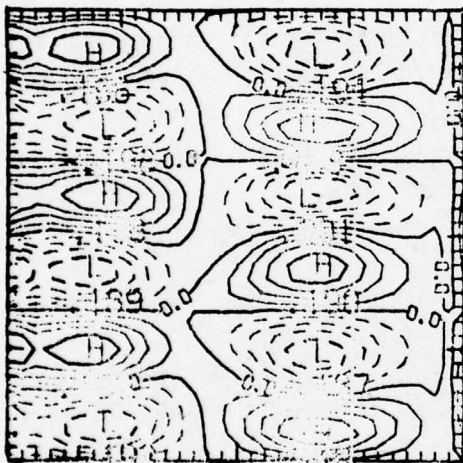
Figure 17



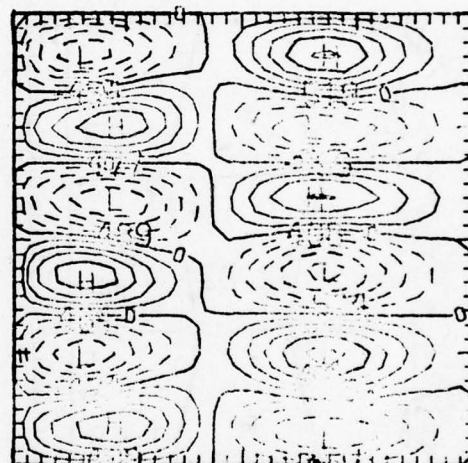
(a)



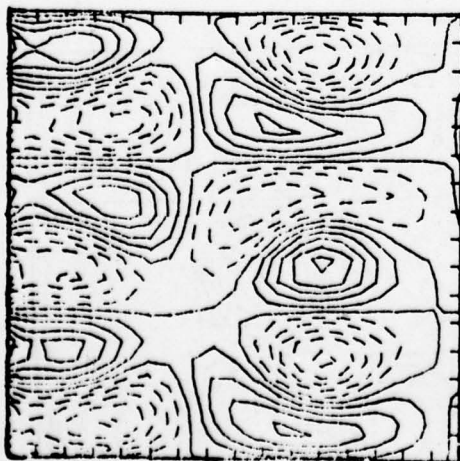
(b)



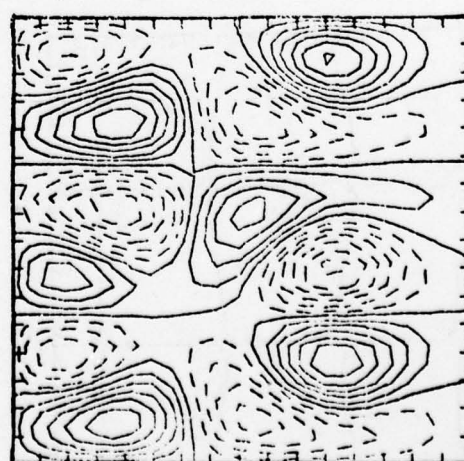
(c)



(d)

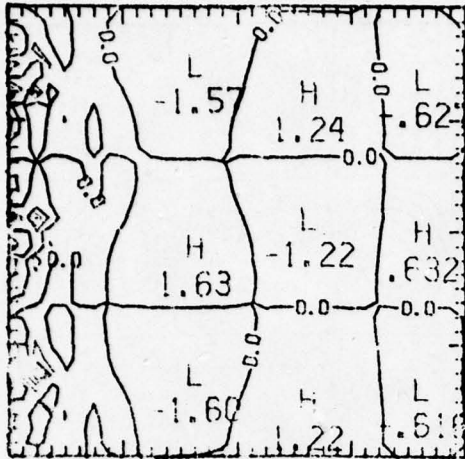


(e)

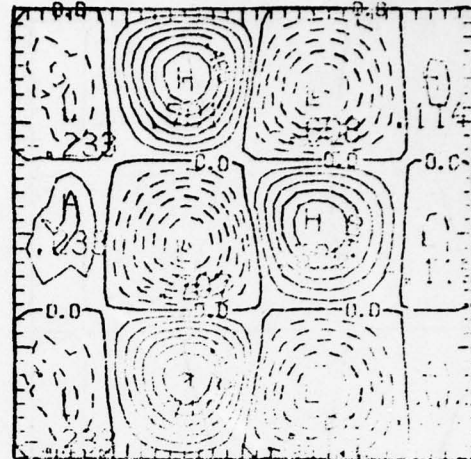


(f)

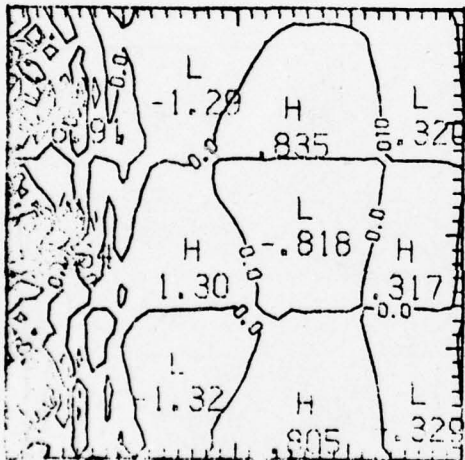
Figure 18



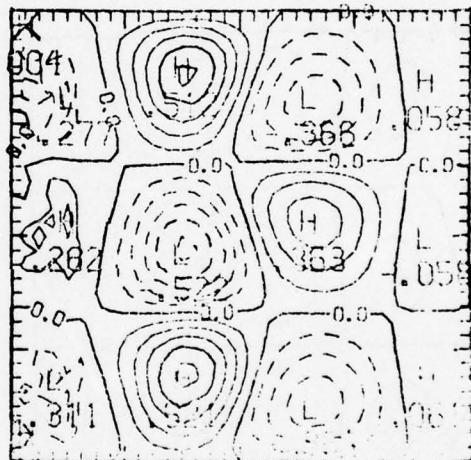
(a)



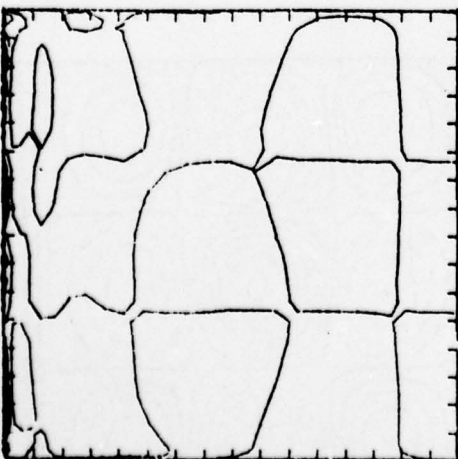
(b)



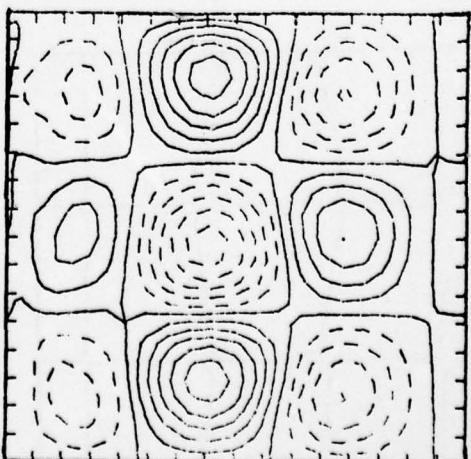
(c)



(d)



(e)



(f)

Figure 19

AD-A052 827

HARVARD UNIV CAMBRIDGE MA DIV OF APPLIED SCIENCES

F/G 8/3

THE ACCURACY, EFFICIENCY AND STABILITY OF THREE NUMERICAL MODEL--ETC(U)

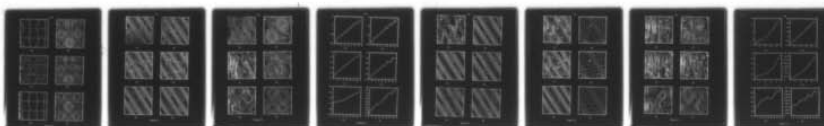
FEB 78 D B HAIDVOGEL, E E SCHULMAN

N00014-75-C-0225

UNCLASSIFIED

NL

2 OF 2
ADA
052827

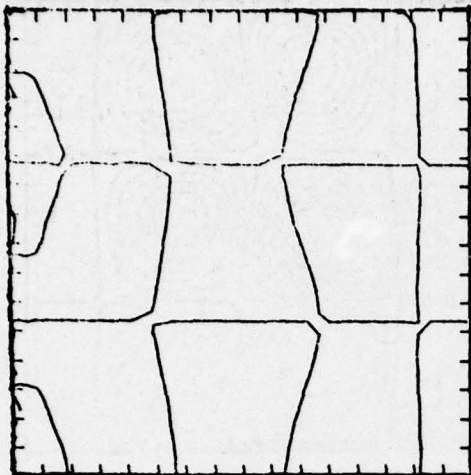


END

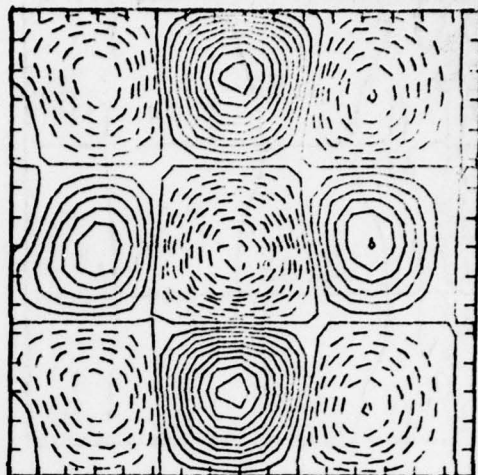
DATE
FILMED

5-78

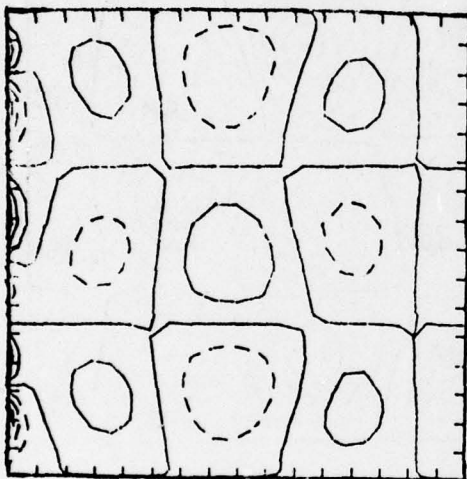
DDC



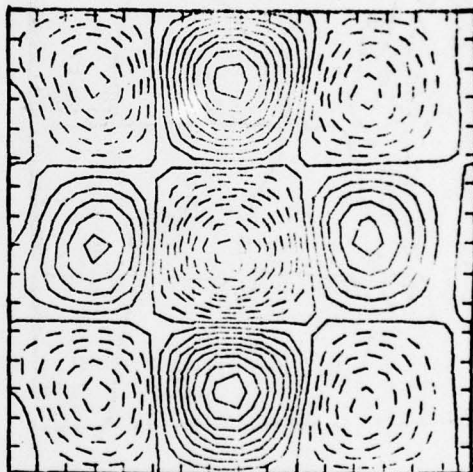
(a)



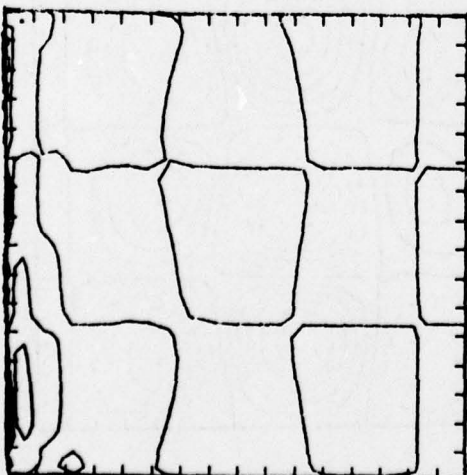
(b)



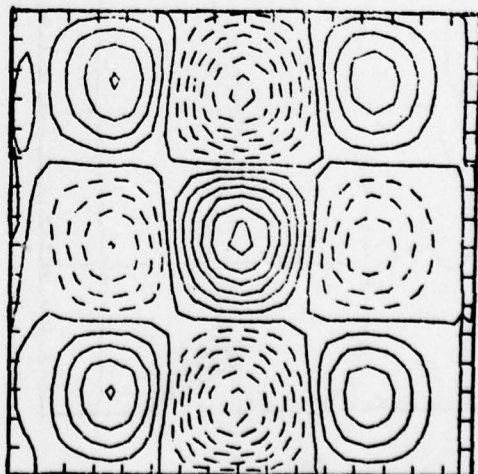
(c)



(d)

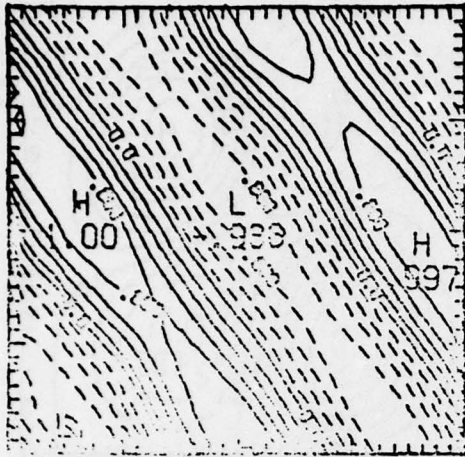


(e)

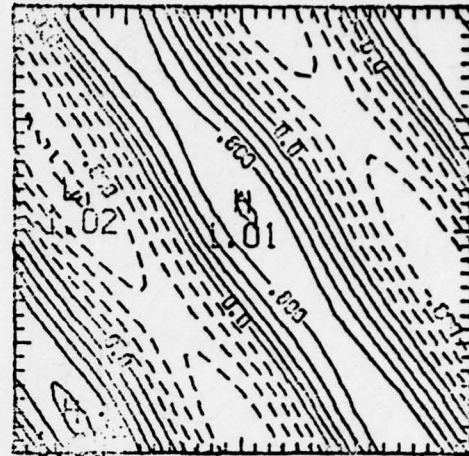


(f)

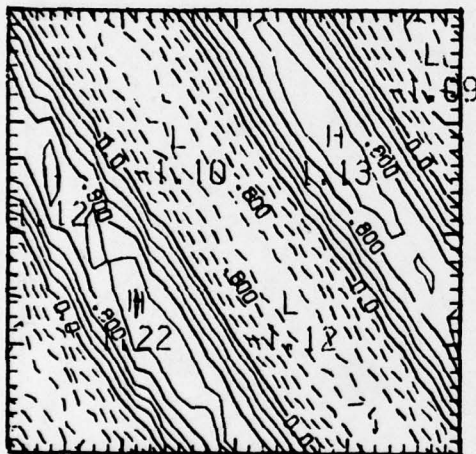
Figure 20



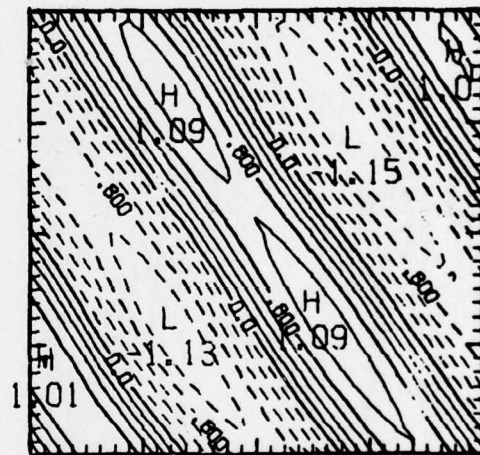
(a)



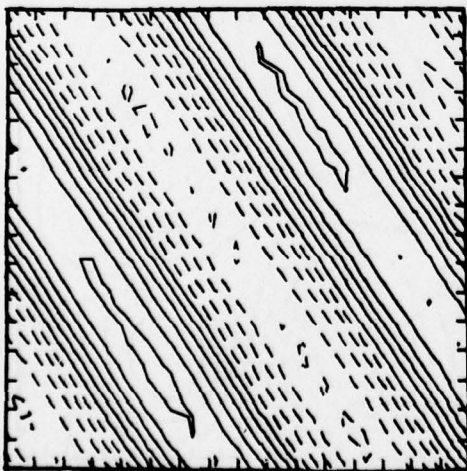
(b)



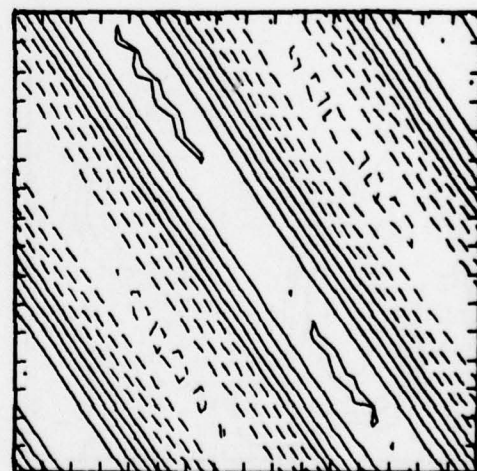
(c)



(d)

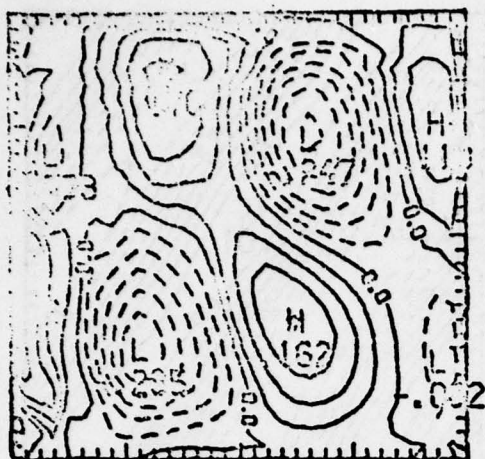


(e)

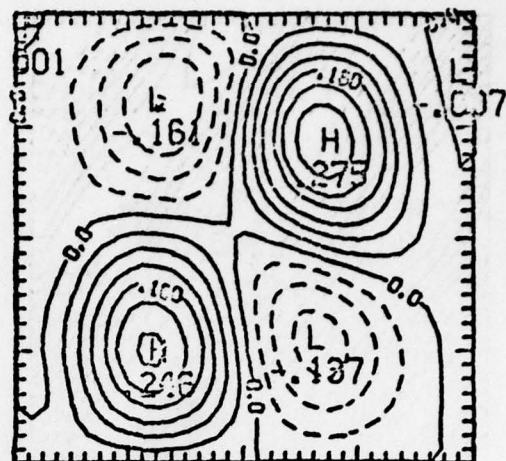


(f)

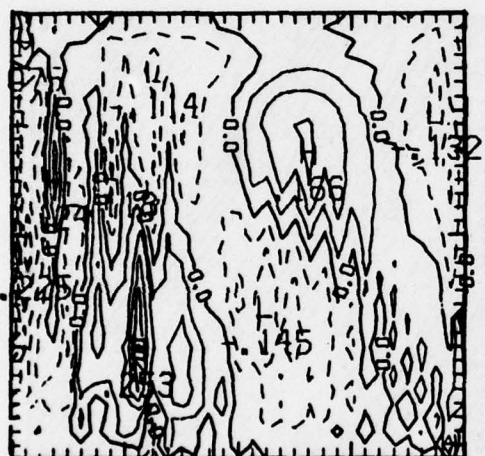
Figure 21



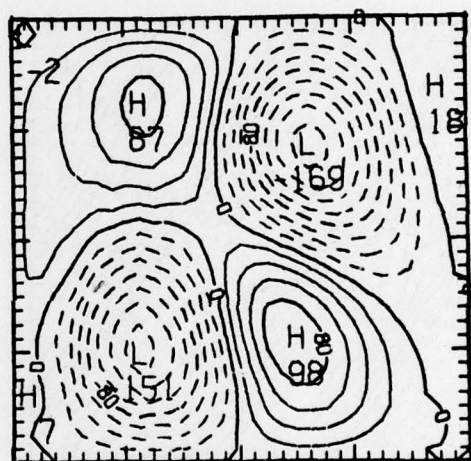
(a)



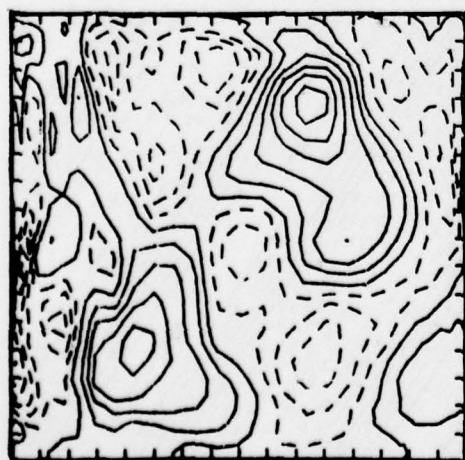
(b)



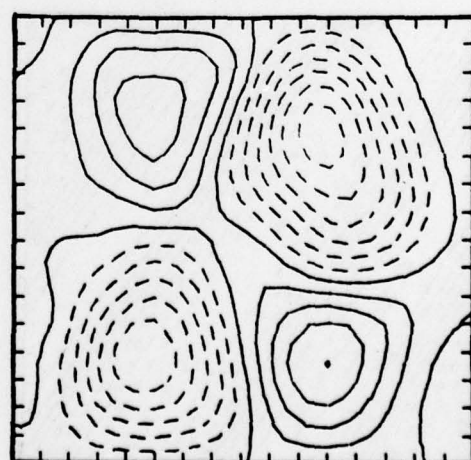
(c)



(d)

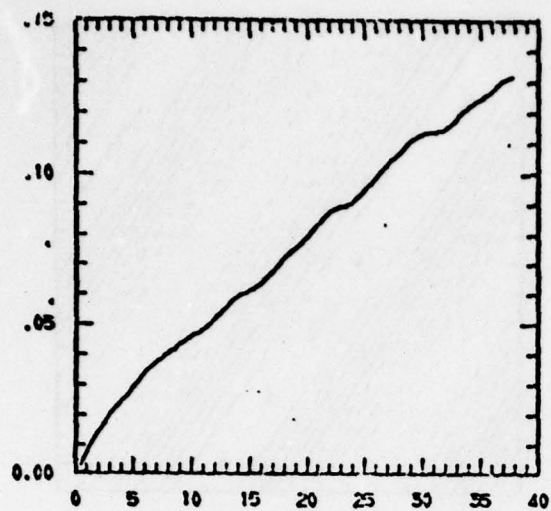


(e)

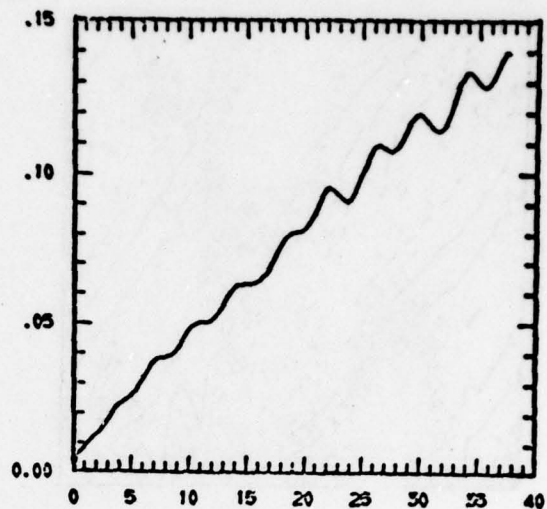


(f)

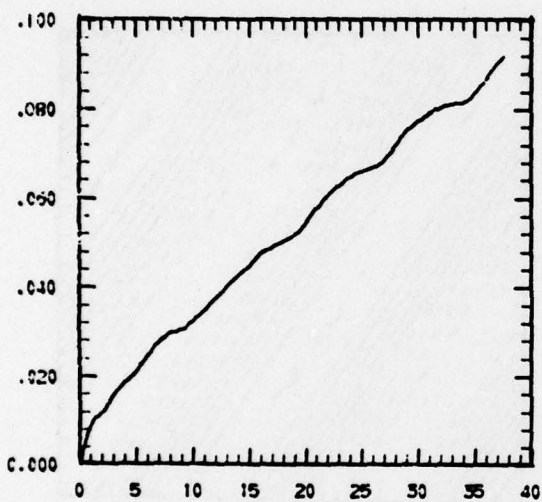
Figure 22



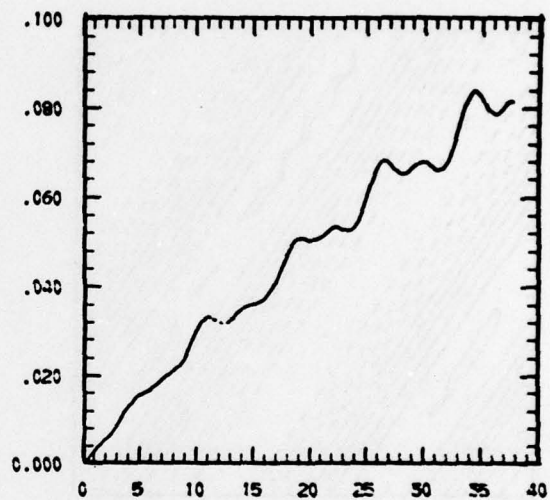
(a)



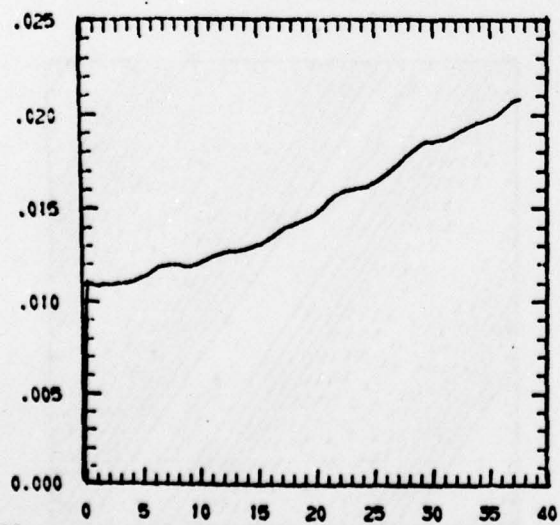
(b)



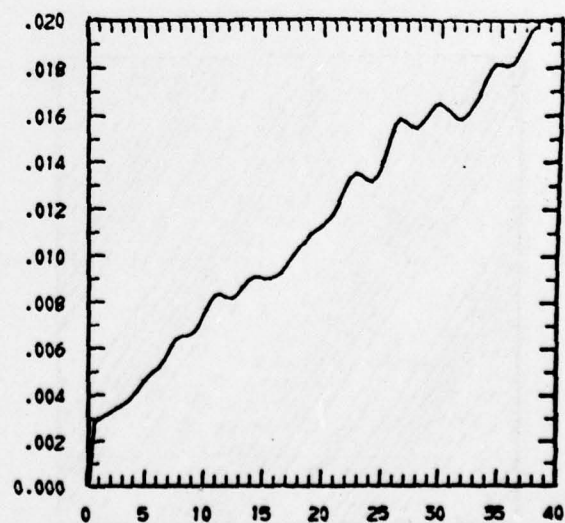
(c)



(d)

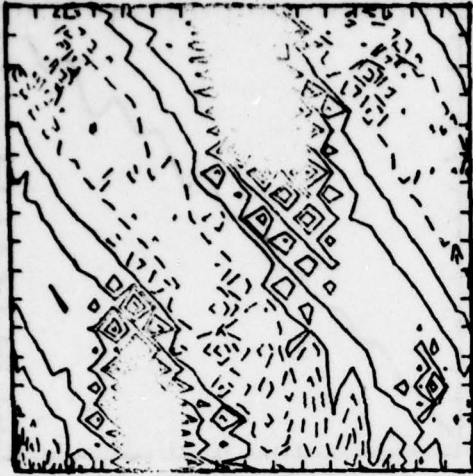


(e)

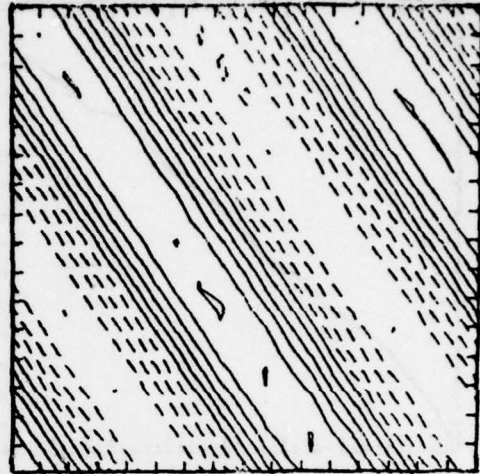


(f)

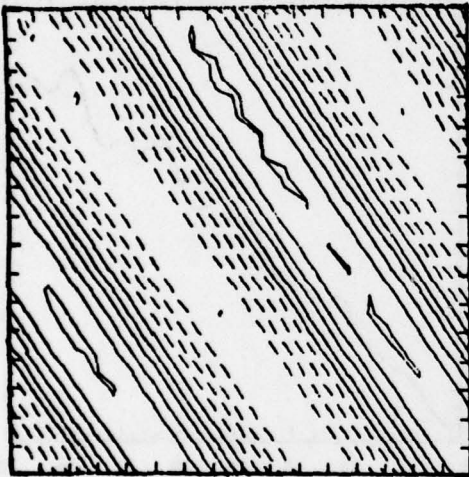
Figure 23



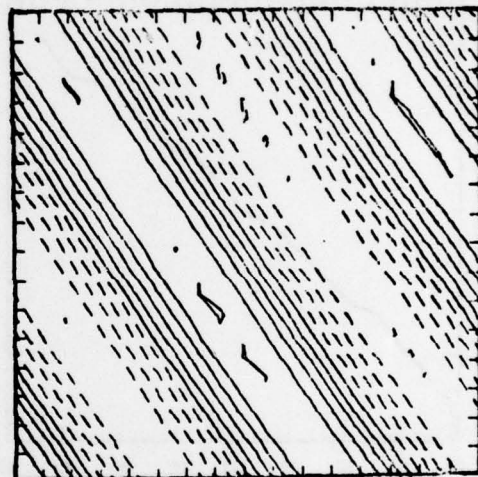
(a)



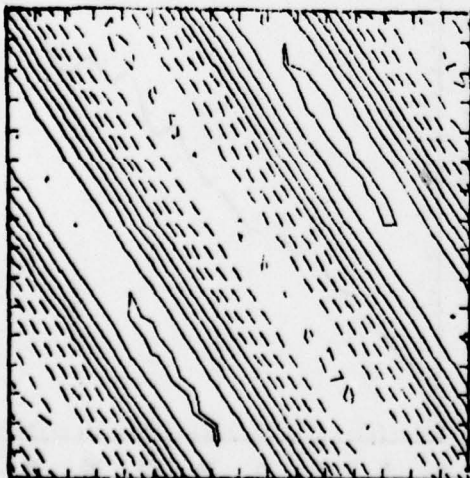
(b)



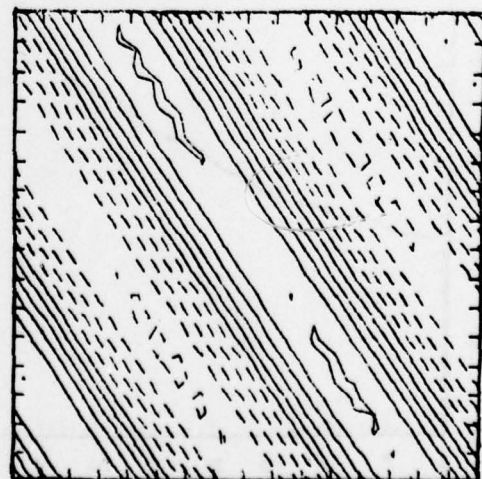
(c)



(d)

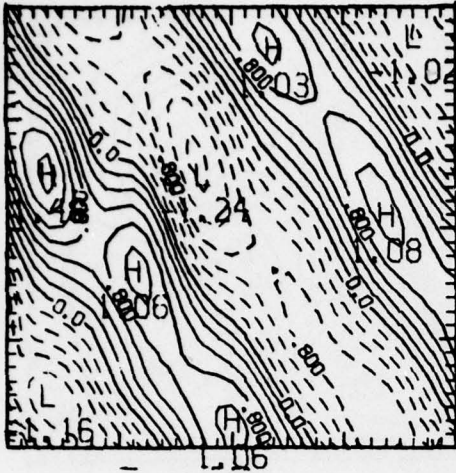


(e)

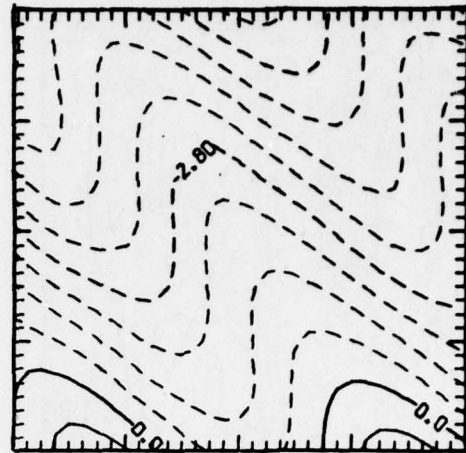


(f)

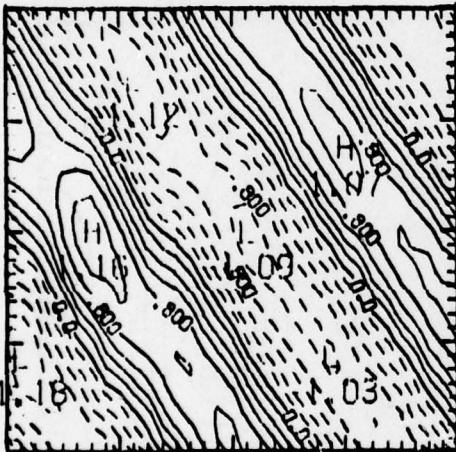
Figure 24



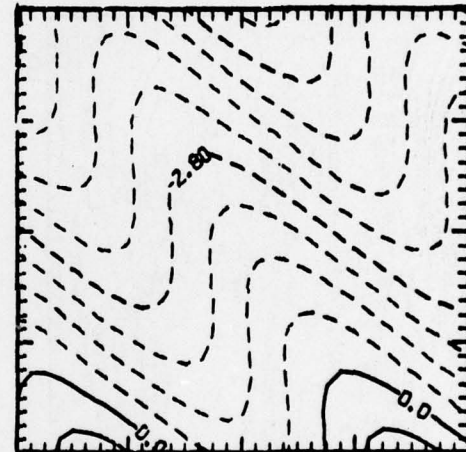
(a)



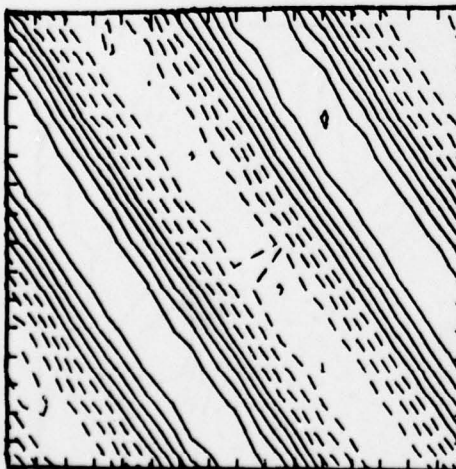
(b)



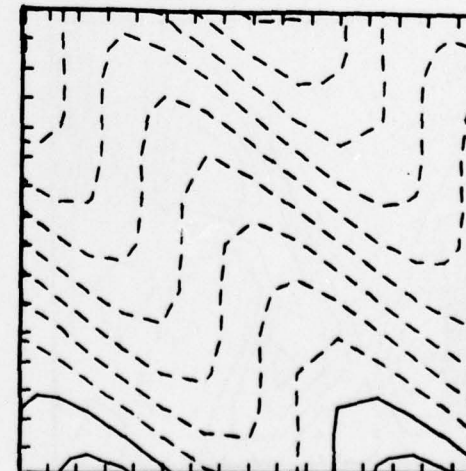
(c)



(d)

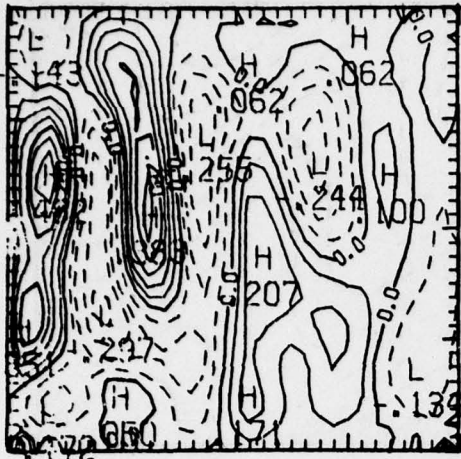


(e)

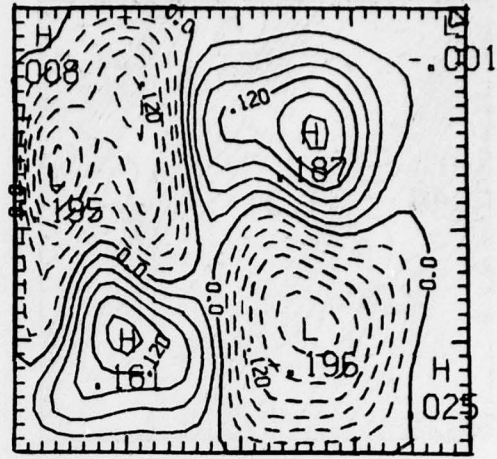


(f)

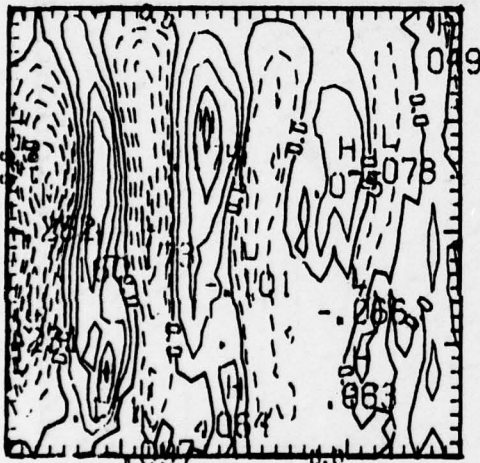
Figure 25



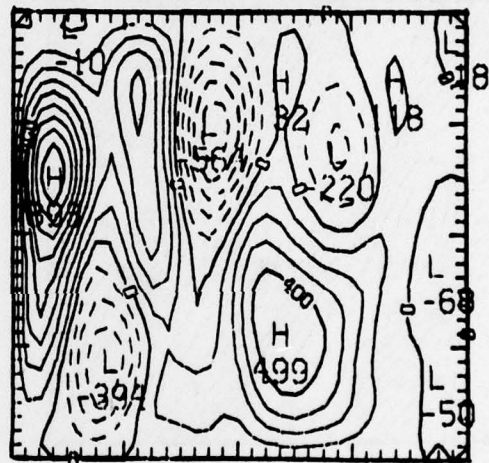
(a)



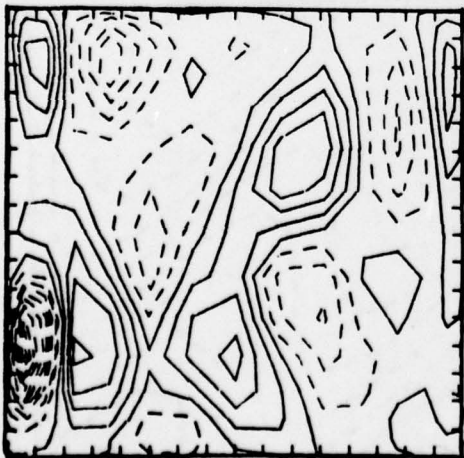
(b)



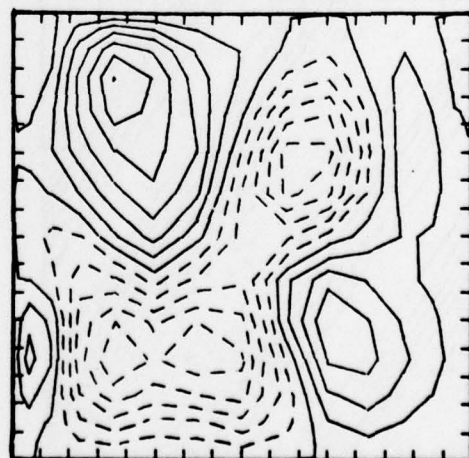
(c)



(d)

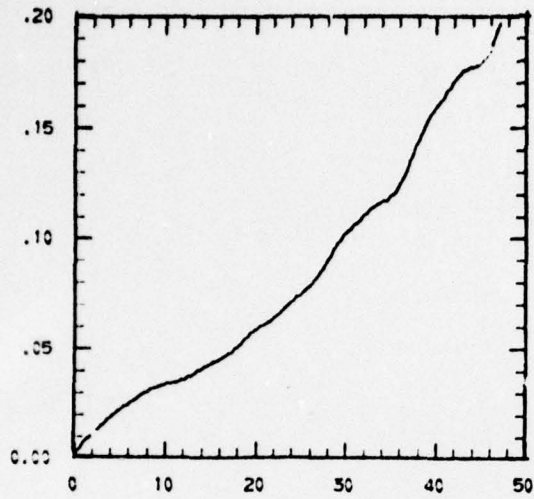


(e)

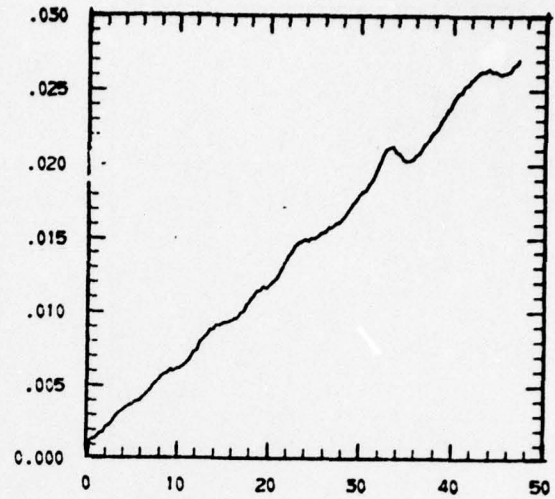


(f)

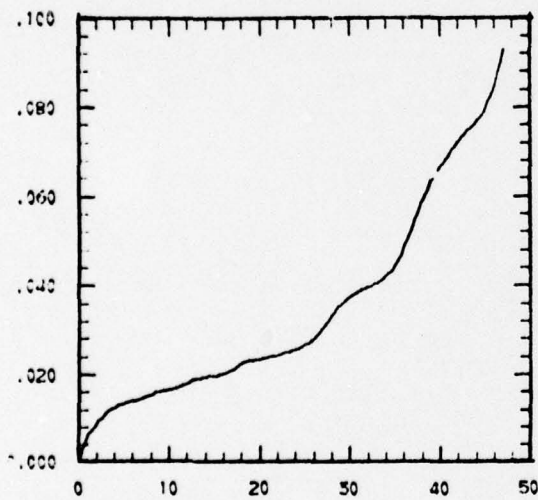
Figure 26



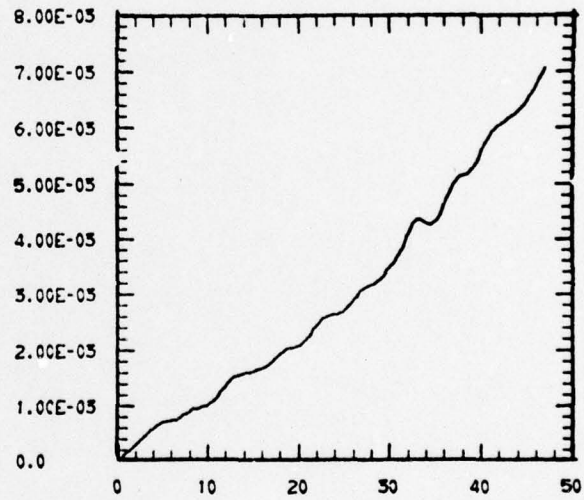
(a)



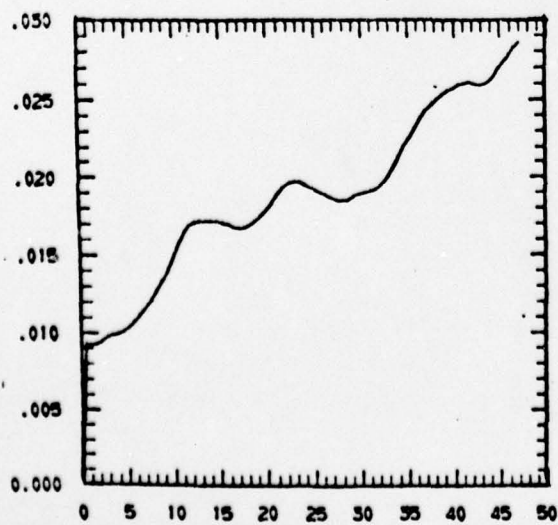
(b)



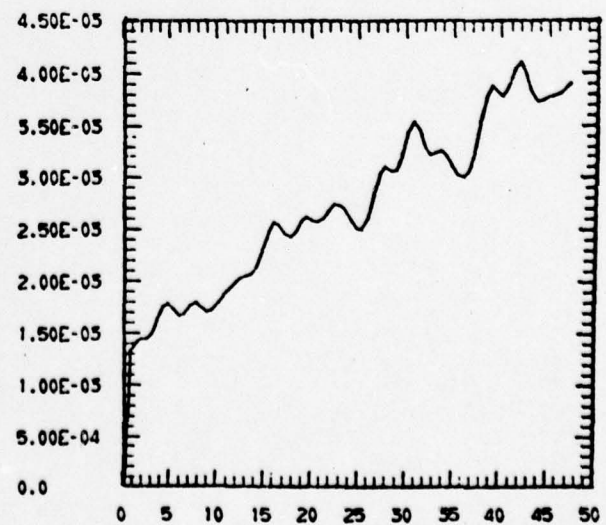
(c)



(d)



(e)



(f)

Figure 27